

The kaobook class

Use this document as a template

Millikelvin Confocal Microscopy of Semiconductor Membranes and Filter Functions for Unital Quantum Operations

Customise this page according to your needs

Tobias Hangleiter*

September 5, 2025

* A \LaTeX lover/hater

The harmony of the world is made manifest in Form and Number, and the heart and soul and all the poetry of Natural Philosophy are embodied in the concept of mathematical beauty.

– D'Arcy Wentworth Thompson

Contents

Contents	iii
I A FLEXIBLE PYTHON TOOL FOR FOURIER-TRANSFORM NOISE SPECTROSCOPY	1
1 Introduction	2
2 Theory of spectral noise estimation	4
2.1 Spectrum estimation from time series	5
2.2 Window functions	7
2.3 Welch's method	8
2.4 Parameters & Properties of the PSD	9
3 The python_spectrometer software package	11
3.1 Package design and implementation	11
3.1.1 Data acquisition	11
3.1.2 Data processing	13
3.2 Feature overview	14
3.2.1 Serial spectrum acquisition	15
3.2.2 Live spectrum acquisition	18
4 Conclusion and outlook	20
II CHARACTERIZATION AND IMPROVEMENTS OF A MILLIKELVIN CONFOCAL MICROSCOPE	23
5 Introduction	24
6 Cryostat performance	27
6.1 Cooling power	27
6.2 Electron temperature	29
7 Optical path	33
7.1 Light coupling	33
7.1.1 Choosing lenses	33
7.1.2 Collection efficiency	37
7.1.3 Imaging the laser spot	40
7.1.4 Cross-polarization extinction	41
7.2 Exemplary measurement of non-classical light	43
8 Vibration noise	45
8.1 Vibration isolation	46
8.1.1 Damping theory	46
8.1.2 Microscope isolation concept	47
8.2 Accelerometric vibration spectroscopy	48
8.3 Optical vibration spectroscopy	49
8.3.1 Noise floor	52
8.4 Routes for improvement	54
9 Conclusion and outlook	56

III OPTICAL MEASUREMENTS OF ELECTROSTATIC EXCITON TRAPS IN SEMICONDUCTOR MEMBRANES	59
10 Introduction	60
11 Photoluminescence and excitons in semiconductors	64
11.1 Photoluminescence in doped GaAs/Al _x Ga _{1-x} As heterostructures	64
11.2 The quantum-confined Stark effect	66
11.2.1 In-plane confinement	67
11.3 Excitonic complexes	70
12 The mjolnir measurement framework	72
12.1 Rationale	72
12.2 Instrument abstraction	72
12.2.1 Excitation path	74
12.2.2 Detection path	74
12.2.3 Sample	74
12.3 Calibrations	74
12.3.1 CCD calibration	75
12.3.2 Power calibration	75
12.3.3 Rejection feedback	76
12.4 Measurement routines	77
12.5 Plotting	78
13 Photoluminescence measurements of doped semiconductor membranes	80
13.1 Photoluminescence spectroscopy	81
13.1.1 Quantum-confined Stark shift	82
13.1.2 Power dependence	84
13.1.3 Spatial dependence	87
13.2 Photoluminescence excitation spectroscopy	89
13.3 Transfer-matrix method simulations of the heterostructure membrane	92
13.3.1 Electric fields in layered thin films	93
13.3.2 Quantum well absorptance	95
13.3.3 Field emission	96
14 Conclusion and outlook	98
 IV A FILTER-FUNCTION FORMALISM FOR UNITAL QUANTUM OPERATIONS	 102
15 Introduction	103
16 Filter-function formalism for unital quantum operations	107
16.1 Transfer matrix representation of quantum operations	107
16.1.1 Brief review of quantum operations and superoperators	107
16.1.2 Liouville representation of the error channel	108
16.2 Calculating the decay amplitudes	113
16.2.1 Control matrix of a gate sequence	114
16.2.2 Control matrix of a single gate	116
16.3 Calculating the frequency shifts	117
16.4 Computing derived quantities	119
16.4.1 Average gate and entanglement fidelity	119
16.4.2 State fidelity and measurements	120
16.4.3 Leakage	121
16.5 Performance analysis and efficiency improvements	121

16.6	Periodic Hamiltonians	121
16.7	Extending Hilbert spaces	122
16.8	Operator bases	123
16.9	Computational complexity	124
17	Filter functions from random sampling	128
17.1	Reconstruction by frequency-comb time-domain simulation	128
17.2	Case studies	130
18	The filter_functions software package	134
18.1	Package overview	134
18.2	Workflow	135
19	Example applications	138
19.1	Singlet-triplet two-qubit gates	138
19.2	Rabi driving	140
19.3	Randomized Benchmarking	143
19.4	Quantum Fourier transform	146
20	Conclusion and outlook	149
	APPENDIX	151
A	Optical coupling	152
A.1	Collection efficiency	152
A.2	Mode profile	153
A.3	Fraunhofer diffraction	154
B	Vibration spectroscopy	156
B.1	Knife-edge measurement	156
B.2	Additional vibration spectroscopy data	156
C	Dependence of TMM simulations on epoxy thickness	157
D	Additional measurements	158
D.1	Self-consistent Poisson-Schrödinger simulation of the membrane band structure	158
D.2	Additional data	158
D.2.1	Combined plot of PL and PLE data	158
D.2.2	2DEG PL as function of power	159
E	Filter Functions	160
E.1	Additional derivations	160
E.1.1	Derivation of the single-qubit cumulant function in the Liouville representation	160
E.1.2	Evaluation of the integrals in Equation 16.40	161
E.1.3	Simplifying the calculation of the entanglement infidelity	161
E.1.4	Sum rule	162
E.2	Singlet-Triplet Gate Fidelity	163
E.3	GRAPE-optimized gate set for QFT	164
E.4	Convergence Bounds	165
E.4.1	Magnus Expansion	166
E.4.2	Infidelity	167
F	Concatenation of second-order filter functions	168

G Monte Carlo and GKSL master equation simulations	173
G.1 Validation of QFT fidelities	173
Bibliography	176
List of Terms	189
Declaration of Authorship	191

List of Figures

2.1	Generated by <code>img/tikz/spectrometer/lockin_dut.tex</code> .	4
2.2	Generated by <code>img/py/spectrometer/lorentz.py</code> .	6
2.3	Generated by <code>img/py/spectrometer/pyspeck.py</code> .	8
2.4	Generated by <code>img/py/spectrometer/pyspeck.py</code> .	8
2.5	Generated by <code>img/py/spectrometer/pyspeck.py</code> .	9
2.6	Generated by <code>img/tikz/spectrometer/daq_settings.tex</code> .	10
3.1	Generated by <code>img/tikz/spectrometer/speck_tree.tex</code> .	11
3.2	Generated by <code>img/py/spectrometer/pyspeck_workflow.py</code> .	15
3.3	Generated by <code>img/py/spectrometer/pyspeck_workflow.py</code> .	16
3.4	Generated by <code>img/py/spectrometer/pyspeck_workflow.py</code> .	17
3.5	Generated by <code>img/py/spectrometer/pyspeck_workflow.py</code> .	17
3.6	Generated by <code>img/py/spectrometer/pyspeck_workflow.py</code> .	17
3.7	Generated by <code>img/py/spectrometer/pyspeck_workflow.py</code> .	18
3.8	Generated by <code>img/py/spectrometer/pyspeck_live_view.py</code> .	19
6.1	Generated by <code>img/py/setup/cooling_power.py</code> .	28
6.2	Generated by <code>img/py/setup/cooling_power.py</code> .	29
6.3	Generated by <code>img/py/setup/cooling_power.py</code> .	29
6.4	Generated by <code>img/py/setup/transport.py</code> .	30
6.5	Generated by <code>img/py/setup/transport.py</code> .	31
6.6	Generated by <code>img/py/setup/transport.py</code> .	32
7.1	Generated by <code>img/tikz/setup/optical_path.tex</code> .	33
7.2	Generated by <code>img/py/setup/single_mode_fiber_coupling.py</code> .	36
7.3	Generated by <code>img/tikz/setup/emission.tex</code> .	37
7.4	Generated by <code>img/py/setup/extraction.py</code> .	38
7.5	Generated by <code>img/py/setup/extraction.py</code> .	39
7.6	Generated by <code>img/py/setup/imaging.py</code> .	40
7.7	Generated by <code>img/py/setup/excitation_rejection.py</code> .	42
7.8	Generated by <code>img/py/setup/g2.py</code> .	43
7.9	Generated by <code>img/py/setup/g2.py</code> .	44
8.1	Generated by <code>img/pdf/setup/springs.py</code> .	46
8.2	Generated by <code>img/py/setup/vibration_spectroscopy.py</code> .	49
8.3	Generated by <code>img/tikz/setup/knife_edge.tex</code> .	49
8.4	Generated by <code>img/py/setup/vibration_spectroscopy.py</code> .	50
8.5	Generated by <code>img/py/setup/vibration_spectroscopy.py</code> .	51
8.6	Generated by <code>img/py/setup/vibration_spectroscopy.py</code> .	51
8.7	Generated by <code>img/py/setup/vibration_spectroscopy.py</code> .	52
8.8	Generated by <code>img/pdf/setup/vibration_spectroscopy.py</code> .	54
9.1	Generated by <code>img/tikz/setup/optical_path_reduced.tex</code> .	56
9.2	Generated by <code>img/py/setup/vibration_spectroscopy.py</code> .	58
11.1	Generated by <code>img/py/experiment/pl.py</code> .	65
11.2	Generated by <code>img/py/experiment/qcse.py</code> .	66
11.3	Generated by <code>img/py/experiment/qcse.py</code> .	67
11.4	Generated by <code>img/py/experiment/qcse.py</code> .	68
11.5	Generated by <code>img/py/experiment/qcse.py</code> .	70

12.1	Generated by img/tikz/experiment/mjolnir_instruments.tex.	73
12.2	Generated by img/tikz/experiment/mjolnir_tree.tex.	74
12.3	Generated by img/py/experiment/calibration.py.	76
12.4	Generated by img/py/experiment/pl.py.	79
13.1	Sample: DOPED M1_05_49-2. $\lambda_{\text{exc}} = 795 \text{ nm}$. $P = 0.92 \mu\text{W}$. Generated by img/py/experiment/pl.py.	81
13.2	Sample: HONEY H13. $\lambda_{\text{exc}} = 795 \text{ nm}$. $P = 1 \mu\text{W}$. Generated by img/py/experiment/pl.py.	82
13.3	Sample: DOPED M1_05_49-2. $V_{\text{CM}} = -1.3 \text{ V}$. $\lambda_{\text{exc}} = 795 \text{ nm}$. $P = 10 \mu\text{W}$. Generated by img/py/experiment/pl.py.	83
13.4	Sample: DOPED M1_05_49-2. $V_{\text{DM}} = -2.7 \text{ V}$. $V_{\text{CM}} = -1.3 \text{ V}$. $\lambda_{\text{exc}} = 795 \text{ nm}$. Generated by img/py/experiment/pl.py.	84
13.5	Sample: DOPED M1_05_49-2. $V_{\text{B}} = 0 \text{ V}$. Generated by img/py/experiment/pl.py.	86
13.6	Sample: FIG F10. $\lambda_{\text{exc}} = 795 \text{ nm}$. $V_{\text{y}} = 30 \text{ V}$ Generated by img/py/experiment/pl.py.	87
13.7	Sample: DOPED M1_05_49-2. $V_{\text{DM}} = -0.43 \text{ V}$. $V_{\text{CM}} = -3.75 \text{ V}$. $V_{\text{y}} = V_{\text{z}} = 30 \text{ V}$. $P = 1 \mu\text{W}$. $\lambda_{\text{exc}} = 795 \text{ nm}$. Generated by img/py/experiment/pl.py.	88
13.8	Sample: DOPED M1_05_49-2. $V_{\text{CM}} = -1.3 \text{ V}$. $P = 1 \mu\text{W}$. Generated by img/py/experiment/ple.py.	90
13.9	Generated by img/py/experiment/tmm.py.	96
13.10	Generated by img/py/experiment/tmm.py.	96
13.11	Generated by img/py/experiment/tmm.py.	97
16.1	Illustration of gate sequence	115
16.2	Generated by img/py/filter_functions/benchmark_monte_carlo.py.	126
17.1	Generated by img/py/filter_functions/monte_carlo_filter_functions.py.	130
17.2	Generated by img/py/filter_functions/monte_carlo_filter_functions.py.	131
17.3	Generated by img/py/filter_functions/monte_carlo_filter_functions.py.	132
19.1	Generated by img/py/filter_functions/cnot_FF.py.	139
19.2	Generated by img/py/filter_functions/periodic_driving.py.	142
19.3	Generated by img/py/filter_functions/randomized_benchmarking.py.	145
19.4	Generated by img/tikz/circuits/qft.tex. Generated by img/py/filter_functions/quantum_fourier_transform.py.	147
19.5	Generated by img/py/filter_functions/quantum_fourier_transform.py.	148
B.1	Generated by img/py/setup/vibration_spectroscopy.py.	156
C.1	Generated by img/py/experiment/tmm.py.	157
D.1	Sample: DOPED M1_05_49-2. $V_{\text{CM}} = -1.3 \text{ V}$. $P = 1 \mu\text{W}$. Generated by img/py/experiment/ple.py.	158
D.2	Sample: DOPED M1_05_49-2. $\lambda_{\text{exc}} = 795 \text{ nm}$. Generated by img/py/experiment/pl.py.	159
E.1	Generated by img/py/filter_functions/cnot_FF.py.	164
E.2	Generated by img/py/filter_functions/quantum_fourier_transform.py.	165
G.1	Generated by img/py/filter_functions/quantum_fourier_transform.py.	174

Publications

- [1] Yaiza Aragonés-Soria, René Otten, Tobias Hangleiter, Pascal Cerfontaine, and David Gross. “Minimising Statistical Errors in Calibration of Quantum-Gate Sets.” June 7, 2022. DOI: [10.48550/arXiv.2206.03417](https://doi.org/10.48550/arXiv.2206.03417). arXiv: [2206.03417](https://arxiv.org/abs/2206.03417) [quant-ph]. Pre-published.
- [2] Pascal Cerfontaine, Tobias Hangleiter, and Hendrik Bluhm. “Filter Functions for Quantum Processes under Correlated Noise.” In: *Physical Review Letters* 127.17 (Oct. 18, 2021), p. 170403. DOI: [10.1103/PhysRevLett.127.170403](https://doi.org/10.1103/PhysRevLett.127.170403).
- [3] Thomas Descamps, Feng Liu, Sebastian Kindel, René Otten, Tobias Hangleiter, Chao Zhao, Mihail Ion Lepsa, Julian Ritzmann, Arne Ludwig, Andreas D. Wieck, Beata E. Kardynał, and Hendrik Bluhm. “Semiconductor Membranes for Electrostatic Exciton Trapping in Optically Addressable Quantum Transport Devices.” In: *Physical Review Applied* 19.4 (Apr. 28, 2023), p. 044095. DOI: [10.1103/PhysRevApplied.19.044095](https://doi.org/10.1103/PhysRevApplied.19.044095).
- [4] Thomas Descamps, Feng Liu, Tobias Hangleiter, Sebastian Kindel, Beata E. Kardynał, and Hendrik Bluhm. “Millikelvin Confocal Microscope with Free-Space Access and High-Frequency Electrical Control.” In: *Review of Scientific Instruments* 95.8 (Aug. 9, 2024), p. 083706. DOI: [10.1063/5.0200889](https://doi.org/10.1063/5.0200889).
- [5] Denny Dütz, Sebastian Kock, Tobias Hangleiter, and Hendrik Bluhm. “Distributed Bragg Reflectors for Thermal Isolation of Semiconductor Spin Qubits.” In preparation.
- [6] Sarah Fleitmann, Fabian Hader, Jan Vogelbruch, Simon Humpohl, Tobias Hangleiter, Stefanie Meyer, and Stefan van Waasen. “Noise Reduction Methods for Charge Stability Diagrams of Double Quantum Dots.” In: *IEEE Transactions on Quantum Engineering* 3 (2022), pp. 1–19. DOI: [10.1109/TQE.2022.3165968](https://doi.org/10.1109/TQE.2022.3165968).
- [7] Fabian Hader, Jan Vogelbruch, Simon Humpohl, Tobias Hangleiter, Chimezie Eguzo, Stefan Heinen, Stefanie Meyer, and Stefan van Waasen. “On Noise-Sensitive Automatic Tuning of Gate-Defined Sensor Dots.” In: *IEEE Transactions on Quantum Engineering* 4 (2023), pp. 1–18. DOI: [10.1109/TQE.2023.3255743](https://doi.org/10.1109/TQE.2023.3255743).
- [8] Tobias Hangleiter, Pascal Cerfontaine, and Hendrik Bluhm. “Filter-Function Formalism and Software Package to Compute Quantum Processes of Gate Sequences for Classical Non-Markovian Noise.” In: *Physical Review Research* 3.4 (Oct. 18, 2021), p. 043047. DOI: [10.1103/PhysRevResearch.3.043047](https://doi.org/10.1103/PhysRevResearch.3.043047).
- [9] Tobias Hangleiter, Pascal Cerfontaine, and Hendrik Bluhm. “Erratum: Filter-function Formalism and Software Package to Compute Quantum Processes of Gate Sequences for Classical Non-Markovian Noise [Phys. Rev. Research 3, 043047 (2021)].” In: *Physical Review Research* 6.4 (Oct. 16, 2024), p. 049001. DOI: [10.1103/PhysRevResearch.6.049001](https://doi.org/10.1103/PhysRevResearch.6.049001).
- [10] Isabel Nha Minh Le, Julian D. Teske, Tobias Hangleiter, Pascal Cerfontaine, and Hendrik Bluhm. “Analytic Filter-Function Derivatives for Quantum Optimal Control.” In: *Physical Review Applied* 17.2 (Feb. 2, 2022), p. 024006. DOI: [10.1103/PhysRevApplied.17.024006](https://doi.org/10.1103/PhysRevApplied.17.024006).
- [11] Paul Surrey, Julian D. Teske, Tobias Hangleiter, Pascal Cerfontaine, and Hendrik Bluhm. “Data-Driven Qubit Characterization and Optimal Control Using Deep Learning.” In preparation.
- [12] Kui Wu, Sebastian Kindel, Thomas Descamps, Tobias Hangleiter, Jan Christoph Müller, Rebecca Rodrigo, Florian Merget, Beata E. Kardynał, Hendrik Bluhm, and Jeremy Witzens. “Modeling an Efficient Singlet-Triplet-Spin-Qubit-to-Photon Interface Assisted by a Photonic Crystal Cavity.” In: *Physical Review Applied* 21.5 (May 24, 2024), p. 054052. DOI: [10.1103/PhysRevApplied.21.054052](https://doi.org/10.1103/PhysRevApplied.21.054052).
- [13] Kui Wu, Sebastian Kindel, Thomas Descamps, Tobias Hangleiter, Jan Christoph Müller, Rebecca Rodrigo, Florian Merget, Hendrik Bluhm, and Jeremy Witzens. “An Efficient Singlet-Triplet Spin Qubit to Fiber Interface Assisted by a Photonic Crystal Cavity.” In: *The 25th European Conference on Integrated Optics*. Ed. by Jeremy Witzens, Joyce Poon, Lars Zimmermann, and Wolfgang Freude. Cham: Springer Nature Switzerland, 2024, pp. 365–372. DOI: [10.1007/978-3-031-63378-2_60](https://doi.org/10.1007/978-3-031-63378-2_60).

Software

The following open-source software packages were developed (at least partially) during the work on this thesis.

- [1] Tobias Hangleiter, Isabel Nha Minh Le, and Julian D. Teske, *Filter_functions* version v1.1.3, May 14, 2024. Zenodo. DOI: [10.5281/ZENODO.4575000](https://doi.org/10.5281/ZENODO.4575000),
- [2] Tobias Hangleiter, *Lindblad_mc_tools* Aug. 8, 2025. URL: https://git.rwth-aachen.de/tobias.hangleiter/lindblad_mc_tools.
- [3] Tobias Hangleiter, *Mjolnir* Aug. 8, 2025. URL: <https://git-ce.rwth-aachen.de/qutech/python-mjolnir>.
- [4] Tobias Hangleiter, Simon Humpohl, Max Beer, and René Otten, *Python-Spectrometer* version 2024.11.1, Nov. 21, 2024. Zenodo. DOI: [10.5281/ZENODO.13789861](https://doi.org/10.5281/ZENODO.13789861),
- [5] Tobias Hangleiter, Simon Humpohl, Paul Surrey, and Han Na We, *Qutil* version 2024.11.1, Nov. 21, 2024. Zenodo. DOI: [10.5281/ZENODO.14200303](https://doi.org/10.5281/ZENODO.14200303),

Part I

**A FLEXIBLE PYTHON TOOL FOR
FOURIER-TRANSFORM NOISE
SPECTROSCOPY**

NOISE is ubiquitous in condensed matter physics experiments, and in mesoscopic systems in particular it can easily drown out the sought-after signal. In solid-state quantum technology research, devices on the length scale of the Fermi wavelength – say tens of nanometers – are embedded in a crystalline matrix of 10^{23} atoms. These devices host single quantum objects such as electrons or quasiparticles—collective many-body excitations. They are controlled and measured by classical signals routed to the device through macroscopic connections like cables and fibers. The signals, in turn, are generated and analyzed by electronic (*e.g.*, transistors) or optical instruments (*e.g.*, lasers) that, in all likelihood, are again based on solid-state technology driven by the first quantum revolution [1, 2]. Ultimately, then, the experiments take place in an environment full of external influences from trams passing by, shaking the ground, to cosmic rays creating electron-hole or breaking up Cooper pairs.

All of these different layers to such experiments are inherently – and in fact often fundamentally¹ – *noisy*, and it is the physicist’s challenge to measure their desired effects in spite of this noise. A well-thought-out experimental setup is hence one that has been designed taking the various noise sources into consideration, and state-of-the-art experiments often need to push the frontier in order to be successful. From material choice in the sample to the signal path and the specs of the measurement equipment, many aspects need to be optimized and, in particular, characterized in order to assess the noise. Indeed, the assessment of noise might even be the entire *goal* of the experiment, for instance to evaluate material properties. In this case, the quantity being measured might not be the same quantity whose noise one is interested in but rather some function of it, and the resulting data still needs to be transformed before one is able to make any practical statements about those properties.

Noise, in the sense that we are concerned with in the present thesis,² is a stochastic process, meaning that we cannot predict with certainty a dynamical system’s time evolution; it *fluctuates* randomly around its noise-free value.³ Only by obtaining statistics, *i.e.*, repeated observations, either by preparing the system in the same initial state or measuring for a certain amount of time, can we make any statements about the underlying stochastic process. Two questions are key to assessing these statistics: first, what is the amplitude of the fluctuations? And second, at which frequency do the fluctuations occur? If the amplitude is small enough, we might not need to care, and if the frequency is large enough, we might be able to average out the fluctuations while if it is small enough, it might appear *quasistatic* and we might be able to subtract them. Although numerous other techniques for measuring and estimating a noise’s properties exist, analyzing noise in frequency space by means of the Fourier transform imposes itself when considering these two notions.

This approach is the central topic of this part of the present thesis. However, we will not be too much concerned with the theoretical side of the subject matter. Rather, I will focus on making these techniques readily and easily accessible to experimentalists in the lab. Given the arguments laid out above, noise spectroscopy should be an essential item in an experimentalists’ toolbelt. In practice, though, we are faced with several challenges. First, different experiments require different data acquisition

1: Consider Johnson-Nyquist noise in a resistor, for example.

2: Quantum noise does not fall under this scope as it may – disregarding vacuum fluctuations for the sake of argument – be considered *emergent*; it arises from a system entangled with a (not necessarily large) number of quantum degrees of freedom being observed, *i.e.*, tracing out the environment’s degrees of freedom. Our lack of knowledge about this environment then appears as noise in our observations. See Reference 3 for a comprehensive review of the quantum case.

3: Quantum measurements are also noisy in this sense as we cannot predict the outcome of a single-shot measurement, but here the stochasticity is in the outcomes of an ensemble rather than the sequence of values in time. The two are, however, closely related through ergodicity, which we will require in Section 2.1.

(DAQ) hardware, all of which have both varying capabilities and software interfaces. Hence, transferring a spectroscopy code from one device or setup to another is a non-trivial task and can inhibit adoption of the technique. Albeit some instruments come with built-in spectroscopy solutions, they vary in functionality and are not easily transferred to different systems. Second, while probably everyone finding themselves in the situation is capable of computing the noise spectrum when presented with a set of time series data, inferring the correct parameters for data acquisition given the desired parameters of the resulting spectrum can, while not difficult, be cumbersome to do.⁴ Lastly, noise spectroscopy is most effective when proper visualization tools are employed. Again, this is not a difficult task per se, but such things always incur overhead costs that can deter users from employing these essential techniques.

Here, I address these points by introducing a Python software package, `python_spectrometer` [4], that tackles the entire processing chain of practical noise spectroscopy in a physics laboratory. By abstracting DAQ hardware into a unified interface, it is portable between different setups. With the goal to make noise spectroscopy as accessible as possible and lower the entry barrier, it automatically handles parameter inference and hardware constraints. Finally, it provides a comprehensive plotting solution that allows for interactively analyzing the data using various different data visualization methods.

The rest of this part is structured as follows. In Chapter 2, I review the mathematical groundwork underpinning noise spectroscopy by means of Fourier transforms of time series and discuss parameters and properties of the central quantity of interest, the power spectral density (PSD). In Chapter 3, I then present the software package by going over its design choices and giving a walkthrough of its features using a typical workflow as an example. I conclude by giving an outlook on future directions in Chapter 4.

4: Although it is of course a good exercise, and, as a physicist, one should always strive to understand the tools one is using and the underlying principles at work. This part of the present thesis is intended to provide a starting point for that.

Conclusion and outlook

4

In this part of the present thesis, I introduced the `python_spectrometer` Python package for interactive, backend-agnostic noise spectroscopy. I first presented the theory behind spectral noise estimation based on time series analysis in Chapter 2. There, I showed how, by the Wiener-Khinchin theorem, the PSD $S(\omega)$ is related to a time-dependent signal by the Fourier transform of its autocorrelation function $C(\tau)$. After discretizing the problem, I discussed how the arising spectral windowing introduces distortions in the estimated PSD through effects such as spectral leakage and scalloping loss. The introduction of windowing naturally led to the need for a more efficient method of spectrum estimation to avoid data wastefulness. This is addressed by Welch's method, which trades spectral resolution for estimation accuracy for a given input size by dividing the input into segments and letting them overlap. Finally, I discussed the various parameters that influence the properties of the spectrum estimate produced by Welch's method.

In Chapter 3, I then introduced the `python_spectrometer` package that facilitates noise spectroscopy based on the theory developed in the previous chapter. While in principle agnostic to the specific technique (simple periodogram, Bartlett's method, *etc.*), it employs Welch's method by default to perform efficient estimation of noise power spectral densities. To make noise spectroscopy as approachable as possible, the package provides a unified interface to various hardware and software backends to manage data acquisition. Furthermore, it incorporates rich plotting features to ease data analysis and thereby expedite the feedback loop with the lab. I first outlined the design choices underlying the source code and explained the mechanism employed to infer DAQ settings from, for example, the physical parameters of the resulting spectrum estimate. I described the interface to drivers for different hardware instruments that makes it possible to use the same user code for spectrum acquisition independent of the specific instrument used for data acquisition while at the same time keeping the amount of required driver code at a minimum. Finally, I showcased the interactive features by means of a typical workflow. Here, the serial approach of recording single spectra that are saved to disk at a time stands in contrast to the non-persistent live mode, where data is continuously acquired and displayed in a separate thread or process.

There are several possible avenues for future development of the `python_spectrometer` package. An obvious case is adding support for more DAQ hardware instruments by implementing DAQ interfaces. Modular devices such as those offered by QBLOX¹ and Quantum Machines² are on track to become the new standard in quantum technology labs. Implementing drivers for these instruments would benefit the adoption of both the instruments and the `python_spectrometer` package. Another valuable addition would be supporting generic instruments abstracted by QuMADA [5]. QuMADA is a QCoDeS-based measurement framework that provides a unified interface to instruments in order to – in a similar spirit to `python_spectrometer`'s DAQ interface – abstract away internals of individual instruments and provide users with a standardized way to interact with them. This approach should naturally lend itself to a single implementation of the DAQ class supporting various instruments through the unified QuMADA interface.

1: <https://www.qblox.com/research>

2: <https://www.quantum-machines.co/>

Next, incorporating noise spectroscopy into the standard measurement workflow of quantum device experiments would allow experimentalists to quickly gauge noise levels as they are performing measurements. If for some reason the noise changed³ the experimentalist could quickly obtain insight into the noise by analyzing the spectrum. In a client-server architecture, which is inherently asynchronous, such as Zurich Instrument's LabOne⁴ software, this is already possible using the web interface. But of course the strength of the `python_spectrometer` package stems from its capacity to be utilized in conjunction with any hardware instrument.

One way to implement such functionality would be to introduce a proxy DAQ subclass to be used together with the live mode presented in Subsection 3.2.2. This proxy class would serve as an interface to external measurement software and expose two attributes; first, a data queue, into which the external code could place arbitrary time series data that was obtained during some measurement, and second, a shared dictionary to hold acquisition parameters as these might change between measurements. Because the live view mode runs in the background, the external measurement framework could push data to the queue whenever new data was taken without obstructing the measurement workflow.

Listing 4.1 shows a template design for such a TeeDAQ class.⁵ The `setup()` method ignores the input parameters and instead obtains the current settings from the shared settings proxy. Similarly, instead of fetching data from an instrument itself, the `acquire()` method attempts to fetch data from the shared queue and blocks the thread if no data is present, thereby efficiently idling and consuming no resources unless triggered by the external caller. A measurement framework would then interact with the TeeDAQ object as exemplarized by the following code:

```
daq = TeeDAQ(...)
spect = Spectrometer(daq)
view = spect.live_view()
...
data = measure(fs, n_pts)
daq.settings.update(fs=fs, n_pts=n_pts)
daq.queue.put(data)
```

Measurement frameworks integrating with this interface could thus provide experimentalists live feedback on current noise levels with negligible overhead and minimal code adaptation.

Finally, it might be useful to not only allow estimating PSDs but also cross power spectral densities (CSDs) or *cross-spectra*. The cross-spectrum⁶ is the Fourier transform of not the autocorrelation but the cross-correlation function $C(\tau)$ (Equation 2.4) between two random processes. Take a set of processes $\{x_1(t), x_2(t), \dots, x_n(t)\}$ that correspond to noise measured at different locations in a sample. The cross-correlation function between variables x_i and x_j is then given by⁷

$$C_{ij}(\tau) = \langle x_i(t)^* x_j(t + \tau) \rangle. \quad (4.1)$$

This function (and its Fourier pair the cross-spectrum $S_{ij}(\omega)$) quantifies the degree of correlation between noise at site i and noise at site j . Unlike the *auto*-spectrum (or self-spectrum), the cross-spectrum is always a complex quantity, even for real $x_i(t)$. It is not hard to see that for quantum processors, for example, these kinds of correlations could have significant impact on operation, and on error correction in particular [6–8]. To incorporate cross-spectra in the `python_spectrometer` package, only small changes should be necessary.

3: As it happens often, unfortunately.

4: <https://www.zhinst.com/ch/en/instruments/labone/labone-instrument-control-software>

```
# daq/tee.py
import dataclasses
import threading
import multiprocessing as mp

from .base import DAQ

@dataclasses.dataclass
class TeeDAQ(DAQ):
    settings:
        ↪ mp.managers.DictProxy
    queue: mp.JoinableQueue
    event: threading.Event

    def setup(self, **_):
        settings = self.
        ↪ DAQSettings(self.)
        ↪ settings
        return settings.
        ↪ to_consistent_dict()

    def acquire(self, **_):
        while not
        ↪ self.event.is_set():
            yield self.queue.
            ↪ get(block=True)
```

Listing 4.1: Template design for a proxy DAQ implementation to stream noise spectra from an external measurement framework. The `settings` attribute is a dictionary proxy shared between processes and used to pass acquisition parameters from the measurement framework to `python_spectrometer`.

5: The UNIX shell command `data = $(measure(**settings) | tee daq)` should give an indication as to the naming.

6: Again, we use the two terms interchangeably unless otherwise indicated, see Sidenote 11 in Chapter 2.

7: Again assuming wide-sense stationary processes.

First, the data acquisition logic would need to be adapted. Two possible routes suggest themselves here; first, specialized DAQ classes could be implemented that, in place of yielding one batch of time series data, yield two batches each time they are queried. This approach first of all requires instruments with multiple channels,⁸ which is not necessarily given. Furthermore, it would incur additional coding efforts by having to re-implement each DAQ class for cross-spectra. On the other hand, it would arguably make synchronization between channels easier to achieve.

A less involved path would adapt the Spectrometer class to work with multiple DAQs. This would not involve additional driver work⁹ and allow the Spectrometer object to ensure synchronization between the different DAQs. The internal workflow shown in Listing 3.3 would then need to be slightly adapted to the code shown in Listing 4.2. The downside of this approach is that synchronization of different instruments or channels would need to be taken care of externally.

```
daq_1 = MyDAQ(driver_handle, channel=1)
# Or MyOtherDAQ(driver_handle_2) if another instrument
daq_2 = MyDAQ(driver_handle, channel=2)
daqs = (daq_1, daq_2)

parsed_settings = [daq.setup(**user_settings) for daq in daqs]
assert all_equal(parsed_settings), "DAQ settings do not match"

acquisition_generators = [daq.acquire(**parsed_settings[0])
                           for daq in daqs]
for data_buffers in zip(*acquisition_generators):
    estimate_csd(*data_buffers)
```

Further code adaptations would involve minor changes such as replacing the spectrum estimator with `scipy.signal.csd()` [9] for CSD estimation¹⁰ and make the plotting conform to complex data.¹¹

8: If one sticks to single DAQ instances managing single instruments.

9: Except possibly ensuring thread safety and timing synchronization if multiple DAQ objects communicate with the same physical instrument.

Listing 4.2: Proposed DAQ workflow for estimating cross-spectra. Each hardware channel (same or different instruments) is assigned to a DAQ object. After instrument configuration, it is asserted that the parameters match. Finally, data is fetched from both channels and fed into a CSD estimator. Note that triggering would need to be implemented externally.

[9]: (n.d.), *csd* — SciPy v1.15.2 Manual

10: In practice, working with the normalized CSD, or correlation coefficient [10, 11]

$$r_{ij}(\omega) = \frac{S_{ij}(\omega)}{\sqrt{S_{ii}(\omega)S_{jj}(\omega)}} \quad (4.2)$$

with $S_{ii}(\omega)$ the PSD of process x_i would likely be more favorable.

11: It could be worthwhile to add a subplot to display both the magnitude and phase of the complex quantity $S_{ij}(\omega)$.

Part II

CHARACTERIZATION AND IMPROVEMENTS OF A MILLIKELVIN CONFOCAL MICROSCOPE

Author contributions — *Parts of the results presented in this part of the present thesis have been published in Reference [12]. Thomas Descamps and Feng Liu originally designed the setup together with Hendrik Bluhm and constructed it. Julian Ritzmann^a and Arne Ludwig^a grew the wafer on which Matthias Künne fabricated the sample used to measure the electron temperature in Section 6.2. The chip used to measure photon antibunching in Section 7.2 was grown by Xuelin Jin. Marcus Eßer kindly lent the accelerometer used in Section 8.2.*

[12]: Descamps, Liu, Hangleiter, Kindel, Kardynał, and Bluhm (2024), *Millikelvin Confocal Microscope with Free-Space Access and High-Frequency Electrical Control*

a: Ruhr-Universität Bochum.

QUANTUM technology is maturing and entering the realm of commercial application [13–17]. Despite this progress, its potential is arguably far from fully tapped. From the perspective of the physicist, quantum technology can not only serve the industrial sector, though, but also become a new tool in the researcher’s belt to explore new physics on the nanoscale, where quantum mechanics governs the behavior of individual particles as well as many-body interactions and collective effects. Given the multidisciplinary nature of the field, this presents a unique opportunity to explore in particular the intersection of different areas of physics such as optomechanics [18, 19], quantum thermodynamics [20–22] and batteries [23], quantum gravity [24, 25], and more. In the solid state, electrical and optical properties dominate. Here, their intersection brings together two of the perhaps technologically most advanced and permeating branches of physics.

The small energy scales involved in electronic *intra*-band effects or many-body correlations often necessitate extremely low temperatures in the Millikelvin range for observation. While optical effects on the other hand are typically robust due to their large energy scales in the visible range,¹ semiconductors or semimetals such as graphene allow optical *inter*-band transitions and as such coupling between the – in themselves low-energy physics of the – valence and conduction band. Thus, observing many-body effects of quasiparticle excitations such as a Bose-Einstein condensate (BEC) of excitons [26–30], for example, places high demands on the experimental setup, requiring not only very low temperatures but also some form of optical access. For quantum technologies, the development of a quantum network based on optically interfaced solid-state spins is among the foremost goals [31–34]. There, single optical photons are generally used to transmit quantum information across long distances and qubits encoded in single spins – electronic or nuclear – are used to store and process information locally. Owing to their small magnetic moment and strong Coulomb interaction, electron spin qubits usually require temperatures well below 1 K for high-fidelity operation, and a coherent interface between these and a “flying qubit” – a photon encoding information, for example, in its helicity or time-of-arrival degree of freedom – would thus also need to be placed in an optically accessible cryostat capable of reaching such low temperatures.

Descamps et al. [12, 35] presented a free-space confocal microscope integrated into a fully wired cryogen-free dilution refrigerator (DR) (Oxford Instruments Triton 450) that facilitates such experiments. In the following, I give a brief outline of the setup described in more detail in Reference 35. The microscope is constructed with the optics fixed

1: Typically quoted as 380 nm to 750 nm corresponding to 1.65 eV to 3.26 eV.

in place on top of the cryostat, alleviating the need to remove and re-align them when opening and closing the cryostat. Optical fibers deliver light to the cryostat from the optical table and back, simplifying the connection between the two components. On the optical table, a tunable continuous-wave (cw) Ti:sapphire laser² (M Squared Solstis) generates coherent radiation that is attenuated by a variable neutral-density (ND) filter mounted on an electrically controlled rotation stage (Thorlabs K10CR1/M) and can be blocked by an electrically controlled filter flipper (Thorlabs MFF101/M). The attenuated light is coupled into a single-mode fiber (SMF) patch cable (Thorlabs 780HP) and delivered to the optical head on top of the cryostat, which I describe and analyze in more detail in Chapter 7. Waveplates mounted on piezoelectric rotation stages (Attocube ECR4040) with controller Attocube AMC100 allow electromechanical control of the polarization state while an Attocube ANC350 controller connected to three piezoelectric linear steppers (Attocube ANPx311) on which the sample is mounted allow precise control of the sample position. Light collected from the sample is coupled into another SMF patch cable on the optical head and, on the optical table, launched into a diffraction grating spectrometer (Horiba FHR1000) with a focal length of 1 m NA-matched to the fiber by a pair of singlet lenses. The spectrometer houses two gratings (600 gr/mm and 1800 gr/mm) mounted on a rotating turret. Two exit ports selectable by an electrically controlled mirror let the dispersed light exit the spectrometer onto either a thermoelectrically cooled charge-coupled device (CCD) (Andor iDus 416) or, through an adjustable slit allowing spectral filtering, into a Hanbury Brown-Twiss (HBT) interferometer. The interferometer consists of a 50:50 beam splitter (BS) on whose exit ports the light is focused into two multi-mode fibers (MMFs) connected to an avalanche photodiode (APD)-based single-photon counting module (SPCM) (Excelitas SPCM-850-14-FC) each. A streaming time-to-digital converter (Swabian Instruments Time Tagger 20) then assigns time tags to the output pulses of the SPCMs heralding the arrival of a single photon.

The entire setup thus consists of various different components of different nature – mechanical, optical, electrical, or a combination thereof – made by various different manufacturers, making the unified control of all instruments challenging. During the work on the present thesis, I extended the Python driver coverage within the QCoDeS framework to include all components that provide an Application Programming Interface (API) for external control. This enables fully remote operation and allows for complete automation of the setup.³ I furthermore implemented the bottom-loading technique for fast sample exchange, whereby the mixing chamber (MXC) is held at 10 K while the sample puck is removed or replaced using a special adapter from below. Turnaround cycles of approximately one day from base temperature to base temperature can be achieved in this way, in contrast to a full warm-up and cooldown cycle time including removal and replacement of all cryostat shields of one week. The optical alignment turns out to be remarkably stable during this procedure and it is usually not required to manually adjust it after a bottom loading cycle.

In this part of the present thesis, I analyze, characterize, and improve upon three different parts of this measurement setup. First, I investigate the refrigeration capabilities of the DR to address the question of how the modifications for optical access impact the cooling performance (Chapter 6). There, I present measurements of various sources of heating and compare them to the available cooling power before turning attention to the achievable electron temperature in a GaAs/Al_xGa_{1-x}As quantum

2: A spectrally filtered, pulsed fs-laser (Coherent Mira 900-F) is also available but unused in the present thesis.

3: Remote turn-on of the laser still requires explicit user input for safety reasons.

dot. In Chapter 7, I then discuss the confocal microscope itself, that is, the optics mounted to the cryostat, including the objective and ocular lenses as well as the coupling to the SMFs. I review the fundamentals of the relevant physics in order to guide the reader through the lens selection process and subsequently compare the estimated setup efficiency to measurements, focusing on the mode profile of dipole radiation emitted from a point source inside a dielectric slab. Moreover, I characterize the laser spot on the sample using the imaging capabilities of the optical head as well as the cross-polarization extinction performance. To validate the optical performance of the microscope, I demonstrate that signatures of non-classical light, specifically photon anti-bunching from a self-assembled quantum dot (SAQD) single-photon source, can be readily observed. Lastly, in Chapter 8, I address the impact of vibrations introduced by the cryostat's operation on the microscope performance. Given that we would like to resolve features on the micrometer scale, and need to couple light emitted from the sample into a SMF with mode field diameter (MFD) of $5\text{ }\mu\text{m}$, random displacements induced by the acoustic waves generated by the cryostat's pulse tube refrigerator (PTR) during operation can potentially limit the microscope's capabilities severely. I take a passive air spring suspension approach to decouple the cryostat from a static rigid reference frame and allow it to be displaced freely and in-phase with the external perturbation. Employing two different techniques, I characterize the vibration noise using the tools developed in Part I and show that the vibrations can indeed be attenuated to a degree sufficient for operation of the microscope.

In this part of the present thesis I analyzed various aspects of the Millikelvin confocal microscope introduced in References 35 and 12. The setup offers the ability to conduct optical measurements of samples at Millikelvin temperatures while at the same time having access to state-of-the-art electrical wiring for sensitive quantum transport measurements such as those performed for semiconductor spin qubit experiments. I first covered the refrigeration aspect of the setup in Chapter 6. Housed in a commercial dry DR, the modifications made for free-space optical access introduce additional heat loads and thus impact the available cooling power budget. Specifically, I quantified the heat loads introduced by the motion stages' resistive position readout and irradiation of the sample with the laser, as well as the base temperature reached for different configurations of anti-reflection (AR)-coated windows installed inside the cryostat. With the optimal configuration of windows, I found the system to reach a base temperature below 10 mK for readout voltages below 100 mV and laser powers below 10 μ W. To assess the impact on electrical performance, I measured the electron temperature in a GaAs/Al_xGa_{1-x}As quantum dot in transport using Coulomb blockade thermometry. I tuned a device designed for spin-qubit operation into a single quantum dot in the few-electron regime and measured the width of a conductance resonance in the sequential tunneling regime in direct transport, obtaining $T = 75$ mK comparable with state-of-the-art systems.

During these experiments, the objective was not focused onto the sample while the entrance window on top of the cryostat was not covered, allowing ambient light to enter. As several studies have found, the electrical characteristics of two-dimensional electron gases (2DEGs) in GaAs/Al_xGa_{1-x}As heterostructures, in particular Si-doped ones, are highly sensitive to illumination, resulting in long-time transient effects and instabilities [36–39]. It would hence be interesting to study the behavior of electron temperature in relation to (wavelength-dependent) illumination, an experiment the setup described in this part of the present thesis is uniquely suited for.

In Chapter 7, I then discussed the optical characteristics of the setup, in particular the microscope and its components. I laid out the rationale behind choosing the lenses for collimating the Gaussian beam launched from the SMF, focusing it onto the sample, collecting the emitted radiation, and focusing that into another SMF. Having chosen the lenses, I analyzed the efficiency of light emitted from a point dipole located inside a dielectric slab being coupled into the SMF. From the analysis, it became clear that the precise spatial distribution of the electric field is non-trivial and warrants further attention. A more detailed numerical simulation could serve to pinpoint areas of improvement besides fairly obvious solutions such as mirrors below the sample or mode-engineering like the approach pursued in Reference 40. On the other hand, measuring the field profile experimentally using a CCD inserted into the optical path right before the detection fiber would allow better matching between theoretically expected and experimentally observed efficiencies.

A crucial point might turn out to be the mirror in front of the objective lens. As shown by Benelajla et al. [41], reflections of polarized non-plane-wave beams induce a modal transform into modes with nodes at the cen-

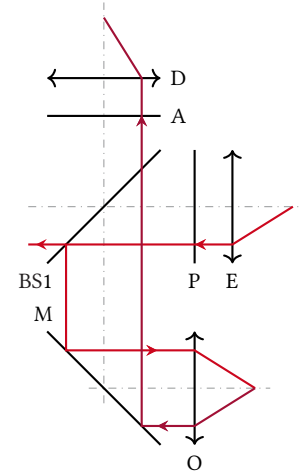


Figure 9.1: Reduced sketch of the optical path (cf. Figure 7.1) including the cold mirror (M). The excitation laser experiences three reflections, twice at M and once at BS1. The light emitted from the sample experiences a single reflection at M.

ter that are spatially filtered by the SMF in a confocal geometry. While beneficial for cross-polarization extinction (*cf.* Subsection 7.1.4), the same effect could lead to radiation emitted from the sample not coupling into the detection fiber if it is co-polarized with the excitation beam.¹ Figure 9.1 shows a reduced sketch of the optical path. Light emitted from the sample is reflected off the mirror (M) and passes through the beam splitter BS1 and the analyzer (A) before being focused into the detection fiber by the ocular lens (D). This situation is equivalent to that described by Benelajla et al. [41] if the emitted light is cross-polarized with respect to A and has a Gaussian mode profile. As I showed in Subsection 7.1.2, the mode overlap between the dipole radiation after collimation and a Gaussian TEM₀₀ mode is quite large at 83 %, implying that the effects investigated in Reference 41 for Gaussian beams will also apply to some extent to the dipole radiation considered here.

For the excitation rejection, the cold mirror potentially adds another issue. As shown by Steindl et al. [43], the giant cross-polarization extinction mechanism in a confocal geometry discovered by Benelajla et al. [41] is reduced in efficacy when additional reflections are introduced into the optical path.² Our situation is again slightly different to the one studied there, however, as the cold mirror is mounted perpendicular to the BS³ and hence the effects on *s*- and *p*-polarizations upon reflection mix. A detailed analysis of the spatial mode profile would thus help elucidate the extent to which these effects matter in our experiments.

Lastly, in Chapter 8, I addressed the impact of vibrations, induced chiefly by the PTR, on the microscope performance. After outlining the basic principles of vibration isolation, I described the suspension scheme based on passive air springs which I installed in the setup to mitigate the vibration noise coupled into system by the PTR. I then performed measurements of the displacement noise power spectral density (PSD) using two different methods. First, using a piezoelectric accelerometer that is directly sensitive to absolute displacements through the local acceleration experienced by the sensor, I found that during operation of the cryostat the vibrations should be considered too large for operation of the microscope, obtaining 1/3 octave band root mean square (RMS) velocities well into the tenths of mm/s range. However, I argued that the absolute value of displacement noise at the sample position is less indicative of the microscope performance than the relative displacement noise between sample and detection fiber, *i.e.*, the vibrations along the optical path. To quantify these, I introduced an optical *in-situ* method of measuring lateral displacement using a knife-edge measurement on a reflectance step on a sample. This technique can be employed without additional modifications or instruments besides those already present in the optical setup. It is based on the fact that the finite spot size of the Gaussian laser beam incident on a step-like reflectance profile such as that produced by a lithographic Au gate on a crystalline surface results in a linear slope in reflected intensity over the width of the laser spot. This allows measuring the reflected intensity as function of time and subsequently converting the intensity to a displacement along the gradient using a previous calibration akin to the charge sensing technique in gate-defined quantum dots (GDQDs), following which the tools laid out in Part I can be used to obtain the noise PSD. Using this technique, I showed that the relative displacement noise is orders of magnitude smaller than the absolute, placing the octave band RMS velocities well below the targeted levels categorized by the vibration criteria. I furthermore analyzed the sensitivity of the technique, showing that the noise floor is dominated by photon shot noise, and laid out routes for enhancing the signal-to-noise

1: Of course, the cross-polarization of analyzer and polarizer will suppress emitted radiation co-polarized with the excitation in any case. The excitation with linear polarization was chosen to coherently address exciton states in a Voigt configuration. If excitation with circularly polarized light is desired, the $\lambda/4$ plate can be moved from the excitation arm to below BS1 similar to Reference 42. I tested this configuration but found the excitation rejection to be poor and reverted to the original configuration.

2: A halfwave plate inserted into the path was also found to reduce the rejection ratio, suggesting that the $\lambda/2$ and $\lambda/4$ plates might also impact performance. On the other hand, Kuhlmann et al. [42] found the $\lambda/4$ plate to be crucial for compensating ellipticities introduced by the setup.

3: That is, while *x* lies in the plane of the BS, *y* lies in the plane of the cold mirror if we use the coordinate system of Figure 8.3 where *x* is the out-of-plane sample coordinate and *z* is along gravity.

ratio (SNR).

Figure 9.2 summarizes the performance of the vibration damping for enabled PTR and the two different vibration spectroscopy techniques. The upper panel shows the relative (instantaneous) displacement noise power for activated suspension referenced to that for deactivated suspension (*cf.* Subsection 3.2.1) on a logarithmic scale. The suspension appears to have a greater effect overall for the absolute level measured with the accelerometer. However, looks can be deceiving as evidenced by the lower panel, which shows the integrated data,

$$\text{Integrated} \equiv 10 \log_{10} \left(\frac{\text{RMS}_S^2(f)}{\text{RMS}_{\text{ref}}^2(f)} \right), \quad (9.1)$$

also on a logarithmic scale (*cf.* Equation 8.4). Clearly, above 10 Hz the suspension improves the overall noise power as measured by the optical method, whereas the absolute level measured with the accelerometer does not recover from the penalty taken between 1 Hz and 10 Hz where oscillations are amplified by the air springs.

The microscope characterized in this part of the present thesis has potential applications beyond the field of quantum technology. Low-temperature effects such as superconductivity and other correlated electronic phases could be studied optically [44–46]. Van der Waals heterostructures appear particularly promising as they allow to combine optically responsive direct-gap semiconductors with metallic materials whose electronic properties can be studied in transport, leading to hybridization and proximity effects due to the atomically close contact [47]. Examples of this include stacks of graphene or bilayer graphene (BLG) with transition-metal dichalcogenides (TMDs) such as MoS₂ or WSe₂ [48–51]. The latter display giant exciton binding energies that are sensitive to the dielectric screening by their close environment, thus allowing to serve as optical sensors of electronic properties [48, 52]. Recent experiments in this direction undertaken in the setup by Tebbe et al. [53] on BLG/WSe₂ show promising first results on spin-orbit interaction (SOI) proximity effects and magnetic phases in BLG [54].

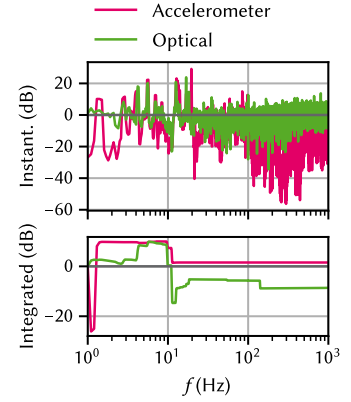


Figure 9.2: Relative displacement noise power of the setup with air spring suspension activated referenced to suspension deactivated. Lower panel shows the fractional integrated data.

Part III

**OPTICAL MEASUREMENTS OF
ELECTROSTATIC EXCITON TRAPS IN
SEMICONDUCTOR MEMBRANES**

Author contributions — *An overview of wafers measured in this part of the present thesis is given in Table D.1. Nikolai Spitzer^a grew wafer #15460 (“HONEY”). Julian Ritzmann^a grew wafer #15271 (“FIG”). Chao Zhao^b grew wafer #M1_05_49. Thomas Descamps fabricated the sample DOPED M1_05_49-2. Sebastian Kindel fabricated the samples HONEY H13 and FIG F10.*

a: Ruhr-Universität Bochum.

b: Then at Forschungszentrum Jülich.

JUST as quantum computers are conceived as the quantum analogon of classical computers with bits and logic operations switched out by quantum counterparts, so can one devise *networks* of such objects, where quantum information generated or processed at a quantum *node* is distributed across long distances through the quantum counterparts of classical information channels [55, 56]. Famously envisioned by Kimble [57], the concept can be extended to the idea of a *quantum internet*. A wide array of ideas has been put forth that make use of the theoretical capabilities of such quantum networks.

Initially, quantum networks were studied in the context of quantum cryptography [58–61]. There, the no-cloning theorem and clever use of entanglement ensure quantum-secured communication between distant parties that cannot be eavesdropped upon or tampered with by adversarial parties without detection.¹ Considerable attention has also been paid to the notion of distributed quantum computation [64]. As quantum computers do not appear to be on the same course of miniaturization as classical computers have been, there might turn out to be a limit to the physical size of quantum computers and, hence, a limit to the processing power of a monolithic node. Distributed quantum computation resolves this bottleneck by allowing computations to be executed across separate nodes much like classical supercomputer clusters. Although a comprehensive resource assessment of the feasibility of such approaches is still outstanding, initial results are promising [65], and experimental demonstrations of small computations have recently been shown [66]. A concept combining distributed quantum computation with quantum cryptography is blind quantum computation [67, 68], which promises a form of cloud-based quantum computation. Also here first experimental demonstrations have been achieved [69].

1: As ever in cryptography, new protocols keep getting hacked and loop-holes are discovered [62, 63]. It will be interesting to see, therefore, if the security will faithfully transfer from theory to experiment.

Next, quantum networks have garnered interest in the field of quantum sensing [70]. This term refers to the branch of quantum technology in which individual quantum systems are employed as highly sensitive sensors, for example of magnetic fields, or, more generally, to perform measurements of physical quantities [24, 71]. For example, there exist proposals to employ quantum networks for long-baseline telescopes that use optical interferometry to enhance the resolution of astronomical imaging [72, 73], akin to the techniques used to produce the first image of a supermassive black hole [74], or global networks of quantum clocks [75]. Going beyond technological applications, the capability to coherently transmit quantum states across large distances opens the pathway to tests of quantum theory itself, and where it might fail [76].² At least since the publication of the Einstein-Podolsky-Rosen (EPR)–paradox [77], tests of the non-locality of quantum mechanics have been proposed [78, 79] and performed [80, 81]. More recently, for example, a small quantum

2: This area of physics is termed *foundations of physics*.

network was used to rule out a description of quantum theory by real numbers [82] and we may expect more such experiments to come [83]. Indeed, as the first small-scale experimental demonstrators arrive [84–87], research into complex quantum networks and their properties and possible applications is still in its beginnings [88].³

So how does such a quantum network work? In the “canonical quantization” picture we already adopted previously, we might simply replace classical, optical links by quantum versions thereof and similarly transmit *flying* qubits instead of bits through those channels. However, even optical fibers, the backbone of the modern internet, are lossy, and since the photon loss scales exponentially with distance, there would be little hope to build networks larger than a few to a few tens of kilometers.⁴ In classical networks, this problem is remedied by repeater stations that simply produce copies of incoming photons and thus amplify the signal. In quantum mechanics, however, this is forbidden by the no-cloning theorem, which states that one cannot achieve a perfect copy of a qubit prepared in an arbitrary and unknown quantum state [92, 93]. To the rescue comes, then, entanglement. By letting two adjacent repeater stations share a bipartite maximally entangled state (often referred to as a EPR or Bell pair), a station, Charlie, positioned between two others, Alice and Bob, each of whom Charlie shares Bell pairs with can perform a Bell measurement on the two halves of the pairs in his possession and thereby project Alice and Bob’s halves into a state that is maximally entangled between the two of them. This technique of entangling two states that have never interacted with each other is known as entanglement swapping [94, 95]. Briegel et al. [96] and Dür et al. [97] then proposed a quantum repeater protocol that uses entanglement swapping, enhanced by entanglement distillation,⁵ to successively entangle neighboring pairs of entangled states whose resource requirements scale logarithmically with the length of the quantum channel between the ends of which entanglement needs to be established. What is more, the protocol tolerates error and loss rates on the percent level and is thus much more benign than quantum error correction (QEC). Following the initial proposal, more improved schemes were developed that tolerate higher errors [98] or employ entirely different techniques [99], see Reference 32 for a review, and recently also experimental realizations have been shown [100].

A crucial detail of the protocol is that it requires storing Bell states until the heralding of successful entanglement in a quantum memory.⁶ In practice, this means that quantum repeaters require a coherent light-matter interface between photonic flying qubits and stationary quantum memory since storing photons is not feasible. Such an interface has been the subject of intense research and there exist a large number of competing approaches that differ in choice of material platform for the memory and choice of encoding for the photon [31, 102]. Among the most advanced are atomic and defect-based systems. Atomic (and ionic) systems are a natural choice as the energy scales of atomic transitions are compatible with photons in the telecom range (~ 1550 nm) [85, 86, 100, 103, 104]. Nuclear spins coupled to defects in crystal lattices have long spin lifetimes at the same time as optical transitions [84, 87, 105–107]. Optically interfacing semiconductor spin qubits⁷ or superconducting qubits, on the other hand, is arguably more challenging because of a separation of energy scales. While qubits in these systems have energy splittings in the GHz regime, telecom photons have energies of hundreds of THz, and so bridging this gap requires some sort of intermediary or *transducer*. For superconducting qubits, approaches based on mechanical resonators [108] and electro-optic nonlinear materials [109] have been pur-

3: Take for example the recent interest in quantum causal order [89–91], originally envisioned to study gravitational effects on quantum coherence.

4: We can expect a survival probability of 1 % over a distance of 100 km [32]. There is therefore arguably no feasible alternative to optical transmission over long distances.

5: Also known as entanglement purification.

6: I note that there exist also protocols for memoryless, all-optical quantum repeaters [32, 101].

7: By semiconductor spin qubits, I refer to qubits encoded in the spin of one or more electrons or holes confined in quantum dots (QDs), in contrast to spins attached to charged defect centers or nuclear spins.

sued among others. For spin qubits, excitons (or complexes thereof) confined in optically active quantum dots (OAQDs) such as self-assembled QDs [110–113] appear to be most promising owing to their excellent optical properties. Due to the fast recombination speeds of excitons, their suitability as a qubit is limited. Single charge carriers confined to self-assembled quantum dots (SAQDs) have been explored instead [114], but still face the problem that the growth of SAQDs is random and as such coupling two or more qubits is extremely challenging. By contrast, spin qubits confined in gate-defined quantum dots (GDQDs) have reached a high level of maturity [115, 116], and the promise of scalability by leveraging the highly advanced industrial semiconductor fabrication technology still holds true.

Jöcker et al. [117] thus proposed a protocol for transferring the quantum state of a photonic, polarization-encoded qubit to that of a spin qubit confined in a GDQD by means of a OAQD serving as intermediary in order to benefit from the benign optical properties of the latter and the long coherence times and processing capabilities of the former. In the protocol, an incident photon generates an exciton in the OAQD, transferring the quantum state to the exciton. By application of a strong in-plane magnetic field, bright and dark states of the exciton are mixed and electron and hole remain in a product state with all information encoded in the electron spin. This allows discarding the hole and subsequently transferring the electron state to the GDQD, the details of which depend on the encoding chosen, either single-spin (Loss-DiVincenzo (LD)) or two-spin (singlet-triplet (ST)) qubit. The protocol is agnostic to the precise realization of the OAQD, although it adopts parameters from SAQDs. A crucial ingredient of the protocol is that the OAQD be in tunnel-coupling distance to the GDQD in order to enable exchange coupling or the adiabatic transfer of the photo-electron. For SAQDs this is a challenging endeavor since, as mentioned above, their growth is random and therefore requires one to first locate the dots and then align the gates during fabrication of the GDQD. Because of the exponential dependence of tunnel coupling on the distance, this alignment needs to be very precise indeed.

An alternative to an SAQD was proposed by Descamps [35] in form of an electrostatic exciton trap. Here, excitons are designed to be confined not by local modifications of the band structure during growth but by application of out-of-plane electric fields through gate electrodes. This tilts the band structure and lowers the exciton energy by the quantum-confined Stark effect (QCSE), where exciton dissociation is prevented by charge carrier confinement in a quantum well (QW). To avoid dissociation by lateral electric fields, Descamps [35] developed a fabrication process to thin down the semiconductor heterostructure to a thin membrane symmetric about the QW, allowing lithographic patterning of laterally aligned, nanometer-scale gate electrodes on both sides of the membrane [118]. Application of voltages of the same magnitude but opposite polarity to gates on the top and bottom side of the membrane then produces – to leading order – a local electric field without changing the chemical potential in the QW itself, while voltages of the same polarity have just the opposite effect. Together with the out-of-plane confinement by the QW, this should in theory provide 0D-confinement of exciton purely by electrostatic means and allow for the top-down, scalable fabrication of OAQDs in close proximity to other, conventional GDQDs. What is more, the confinement strength and potential relative to the neighboring GDQD can be finely tuned by well-established techniques.

In Reference 118, Descamps et al. demonstrated the implementation of the membrane fabrication process as well as initial progress towards

forming a GDQD in transport and optical measurement of the lowering of the local exciton potential by the QCSE. Yet unobserved was the signature of QD-behavior in an exciton trap as manifested by, for example, the resolution of orbital splittings or single-photon emission. In this part of the present thesis, I present optical measurements of exciton traps towards this goal. It is outlined as follows. In Chapter 11, I give an introduction to the physics of photoluminescence (PL) in semiconductors as well as the influence of electric fields. Following that, I introduce the Python measurement framework I wrote to control the experiment in Chapter 12. Then, in Chapter 13, I present measurements of doped membranes. I show data of an exciton trap and discuss the voltage, power, and position dependence of the PL emission as well as photoluminescence excitation (PLE) measurements. Finally, I perform simulations of the membrane structure to explain the quenching of PL intensity observed when focusing a gate and propose slight modifications to the heterostructure design to mitigate this effect. I conclude with an outlook in Chapter 14.

In this part of the present thesis, I presented and discussed optical measurements of doped semiconductor membranes under perpendicular electric fields. I first gave an introduction to the physics of photoluminescence (PL) in semiconductor QWs in Chapter 11. Starting with the PL of an unbiased two-dimensional electron gas (2DEG) in a QW, which is defined by the band gap and the Fermi edge at low and high energies, respectively, I then performed calculations of the electron and hole energies in an undoped QW under the influence of an external electric field. This gives rise to the QCSE and quadratically lowers the energy difference between electron and hole ground states. The QW confinement prevents the field ionization of excitons and instead leads to a continuously decreased wave function overlap resulting in enhanced lifetime and reduced oscillator strength. I showed that, when taking into account lateral confinement by application of a local electric field as envisaged by Descamps [35], the oscillator strength vanishes for finite orbital angular momentum quantum numbers under the assumption of rotational symmetry, resulting in an optically resolvable level splitting of $2\hbar\omega$. Furthermore, the model predicts that the oscillator strength of excited states vanishes at certain electric fields because their wave functions have nodes in the QW. Using simple approximations, I finally estimated the Fowler-Nordheim tunneling rate of charge carriers escaping the QW confinement as function of the electric field, finding that below 5 V/nm rates are below 1 MHz. In the analytical calculations, I neglected excitonic effects, which for quantitative results need to be considered. Furthermore, the samples investigated later on in this part of the present thesis all contained a doped QW hosting a 2DEG whose presence certainly alters the picture. Many-body theory is required to fully capture the arising effects such as the Fermi-edge singularity (FES) and Mahan excitons [119].

In Chapter 12, I introduced the `mjolnir` measurement framework that facilitates optical experiments in the Millikelvin confocal microscope presented in Part II. I made the case for its existence and outlined the design goals before sketching the package's implementation and features. Central to these is the abstraction of physical instruments into logical ones, combining the parameters of different devices into logical functionality. Because of the relatively large range of different devices used to control the optical setup, this significantly reduces the level of complexity exposed to the user during the measurement workflow and enables the concise definition of measurements without large amounts of repetitive setup and teardown code. A very simple example is the `Excitation_Path` instrument's `wavelength` parameter, which not only sets the wavelength of the continuous-wave (cw) laser but also adjusts the wavelength parameter of the power meter, thus ensuring the sensor reading is correctly converted. Furthermore, the package implements multiple calibration routines, for instance to automatically update the energy axis of the charge-coupled device (CCD) mounted after the spectrometer. Measurements are implemented as multi-dimensional loops defined by composable `Sweep` objects and run through a central `MeasurementHandler` object that can be customized to execute default setup and teardown tasks as well as perform standard modifications of measurement definitions. Finally, `mjolnir` provides live plotting of power meter readings, CCD data, or avalanche photodiode (APD) count rate, as well as an interactive data

plotter based on 2D-slices through multidimensional data. Since the rest of the package is independent of the measurement functionality, other QCoDeS-based measurement frameworks such as quantify can readily replace or augment the latter, for instance to benefit from more sophisticated measurement control workflows that include timing control flows and broader support for buffered sweeps, or leverage the data analysis capabilities.

Employing the mjoInir software framework, I conducted optical measurements of doped QW membranes that I presented in Chapter 13. With the aim of demonstrating the spatial 0D-confinement of excitons by electrostatic means, I characterized the PL as function of position and electric field applied by means of local gate electrodes on the top and bottom sides of the membrane. The 2DEG PL of the unbiased QW was found to be in good agreement with the intuition obtained in Chapter 11, although it also revealed a significant mismatch between nominal and actual charge carrier densities for multiple samples. Defining the difference-mode (V_{DM}) and common-mode (V_{CM}) voltages as the difference and sum of top and bottom gate voltages, respectively, the electric field across the membrane is expected to be proportional to V_{DM} . In most samples investigated, the QCSE was not symmetric in V_{DM} , however, but showed an offset of around 700 mV, corresponding to an admixture of V_{CM} , that can be explained by built-in screening on one side of the membrane, the origin of which is unknown. Updating the virtual gate matrix to compensate for this effect (Equation 13.4) in future measurements would simplify their interpretation.

For small V_{DM} , the field inside the QW is entirely screened by the 2DEG. Surprisingly, though, at about ± 1 V from the symmetry point, the charge carrier density starts to reduce until the 2DEG is fully depleted at about the same amount higher voltages again. I proposed that this is due to carrier sweep-out by Fowler-Nordheim tunneling that establishes an equilibrium between ionized dopants in the AlGaAs barrier and the charge carriers in the well. As the electric field is increased, the tunnel coupling increases and more ionized donors neutralize with electrons from the QW. This reduces the band bending, in turn broadens the tunnel barrier, and hence counteracts the increased transparency due to the tilting of the bands by the electric field. Overall, the emission energy could be tuned by 20 meV in the fully depleted regime.

Measuring the power dependence of the Stark-shifted emission line revealed no biexciton peaks. Instead, a substructure of a considerable number of individual lines appeared. At very small excitation powers, the main emission line displayed a logarithmic blue shift whose strength drastically changes above 10 nW. Several exciton traps showed an intricate substructure of the main emission line, whose constituents coupled differently to the electric field. As one-dimensional position sweeps across a trap also showed, the most likely explanation are a number of different emitters at different spatial locations within the area covered by the microscope focus. Possible candidates are impurities, defects, or interface steps or islands. While the literature has shown these to also be capable of binding excitons, no signatures of confinement were observed in $g^{(2)}$ measurements.

Such could also be revealed by photoluminescence excitation (PLE), a measurement of which I presented in Section 13.2. While the trap diameter was large and the expected orbital splitting of an excitonic quantum dot quite small and not observed, several interesting features appeared

nonetheless. I put forth several hypotheses for the origin of the duplicated absorption edge as well as a second duplicated feature with positive Stark shift. Among them were light-hole excitons, excited QW states, and optical phonons, although none yield a quantitative agreement with the literature. For the largest electric field, where the 2DEG is fully depleted, both the PL and PLE displayed a peak splitting of the same magnitude, ~ 3 meV but 40 meV apart. The PL line was well fitted by a trion and exciton line shape. In the regime of finite electron densities it might be interesting to investigate if trion-polaritons occur in this system [120–122].

Finally, I addressed the observed quenching of PL intensity when the microscope focus is moved on top of gates on the backside of the membrane. I appealed to multilayer interference effects that lead to a reduction in both absorption of irradiant photons in the QW as well as in outcoupling efficiency. Using the transfer-matrix method (TMM), I simulated the membrane heterostructure for different configurations of gates on either sides and found good qualitative agreement with the behavior observed in experiments. I then optimized the AlGaAs barrier thickness for higher absorptance and, based on this, proposed increasing the current thickness of 90 nm by a modest 30 nm to achieve a 16-fold improved absorptance and better outcoupling efficiency.

Ultimately, though, I did not observe signatures of exciton confinement by local electrostatic potentials, which would be a significant step towards the realization of a spin-photon interface to semiconductor spin qubits by top-down fabrication. Where does this leave the concept introduced by Descamps [35]? Firstly, none of the samples that I investigated were fully functional, and as such we cannot make any definitive statements about the feasibility of the concept. Indeed, we can take the opposite point of view: none of the measurements presented in the present thesis provide any negative evidence that would *prohibit* electrostatic exciton trapping as envisioned in Reference 35. All observed deviations from the expected behavior should be possible to resolve by improved sample growth in close feedback with experimental characterization. Access to the full parameter space of virtual difference-mode and common-mode voltages of a sufficiently small central gate pair surrounded by a larger guard gate can reasonably be expected to provide enough tunability to confine single excitons. Given the above, the guard common mode should be used to overcome the screening and deplete the 2DEG. Then, the central difference mode should have a large enough window of operation before the Schottky barrier breaks down ($V_{DM} \approx \pm 1.4$ V) to provide a localized electric field that, going by the calculations in Chapter 11, lowers the exciton energy by up to 25 meV, and results in a quantum dot orbital level splitting on the order of 0.5 meV, large enough to be resolved by PLE. The optimization of the heterostructure design I proposed should furthermore provide higher radiative efficiency and thus allow measurements over a wider range of excitation powers while only modestly lowering the achievable electric field for a given voltage. To enable resonance-fluorescence (RF) measurements, the coherence of excitation and subsequent emission under the current polarization configuration of the confocal microscope should be investigated (see Chapter 9).

Moving beyond GaAs, Reznikov [39] proposed an implementation of the device concept in another material system, $\text{Ge/Si}_{1-x}\text{Ge}_x$. Hole spin qubits in this system have quickly matured in recent years. What is more, by carefully engineering the alloy composition and strain of the QW, a semi-direct¹ bandgap as well as type-I confinement² is projected to be achievable. Favorably, the optical gap can be tuned to the telecom O-band and

1: *I.e.*, the band structure has conduction and valence band minima and maxima at the Γ -point, but the Γ -valley is not the lowest conduction band valley.

2: *I.e.*, the band alignment of the valence band is inverted compared to the conduction band and both electrons and holes are confined in the QW.

thus alleviate the need for quantum frequency conversion to match quantum network operation wavelengths. However, the optical characterization of this system will be challenging as the quasi-direct band gap leads to reduced PL efficiency due to valley coupling.

Part IV

A FILTER-FUNCTION FORMALISM FOR UNITAL QUANTUM OPERATIONS

Author contributions — *This part of the present thesis is based to large extent on Reference [123], an early draft of which in turn was my Master’s thesis [Hangleiter2019a], and as such contains text written by all three authors. Chapter 19 and Appendix G additionally contains results published in Reference [124]. Parts of this work have also been included in Reference [125]. Refer to References [Hangleiter2019a] and [125, Section 3.7] for detailed author contributions up to that point. Chapter 17 and Appendix F contain new results.*

Note — *In Reference [123], extensive use was made of Kubo’s cumulant expansion [126]. Due to an error in Kubo’s paper which was only pointed out several years later [127] and we were not aware of, those results turned out to be not exact as claimed but approximate [128].¹ We address this discrepancy in Chapter 17.*

IN the circuit model of quantum computing, computations are driven by applying time-local quantum gates. Any algorithm can be compiled using sequences of one- and two-qubit gates [130]. Ideal, error-free gates are represented by unitary transformations, so that simulating the action of an algorithm on an initial state of a quantum computer amounts to simple matrix multiplication. Real implementations are subject to noise that causes decoherence resulting in gate errors. If the noise is uncorrelated between gates, its effect can be described by quantum operations acting as linear maps on density matrices, even when several gates are concatenated. A closely related approach is the use of a master equation in Gorini-Kossakowski-Sudarshan-Lindblad (GKSL) form [131, 132], which governs the dynamics of density matrices under the influence of Markovian noise with a flat power spectral density.

Yet many physical systems used as hosts for qubits do not satisfy the condition of uncorrelated noise. One example frequently encountered in solid-state systems is that of $1/f$ noise, which in principle contains arbitrarily long correlation times. It emerges for instance as flux noise in superconducting qubits and electrical noise in quantum dot qubits [133–136]. Whereas simple approaches exist to treat for example quasistatic noise, which corresponds to perfectly correlated noise (*i.e.*, a spectrum with weight only at zero frequency), they cannot be applied to $1/f$ noise because of the wide distribution of correlation times it contains [137]. Thus, there is a gap in the mathematical descriptions of gate operations for noises with arbitrary power spectra that exist between the extremal cases of perfectly flat (white) and sharply peaked (quasistatic) spectra. To capture experimentally relevant effects important to understand the capabilities of quantum computing systems, a universally applicable formalism is hence desirable. For example, one may expect the fidelity requirements for quantum error correction to be more stringent for correlated noise as errors of different gates can interfere constructively [138]. On the other hand, it might also be possible to use correlation effects to one’s benefit, attenuating decoherence by cleverly constructing the gate sequences in algorithms.

[123]: Hangleiter, Cerfontaine, and Bluhm (2021), *Filter-Function Formalism and Software Package to Compute Quantum Processes of Gate Sequences for Classical Non-Markovian Noise*

Hangleiter2019a

[124]: Cerfontaine, Hangleiter, and Bluhm (2021), *Filter Functions for Quantum Processes under Correlated Noise*

[125]: Cerfontaine (2019), *High-Fidelity Single- and Two-Qubit Gates for Two-Electron Spin Qubits*

[128]: Hangleiter, Cerfontaine, and Bluhm (2024), *Erratum: Filter-function Formalism and Software Package to Compute Quantum Processes of Gate Sequences for Classical Non-Markovian Noise [Phys. Rev. Research 3, 043047 (2021)]*

1: Unfortunately, the error has proliferated through the literature and proves quite pervasive despite the significant amount of time that has passed since it was first discovered. Recent examples include Reference 129. One may only speculate if this is because of the 14 years that passed between the original publication and the correction, the lack of an erratum once the mistake had been discovered, or simply because of Kubo’s fame. In any case, it might serve as a cautionary tale and possibly an impetus to a less static publication system that allows, for example, cross-linking commentaries and critiques.

As experimental platforms begin to approach fidelity limits set by employing primitive pulse schemes [135, 139, 140] and detailed knowledge about noise sources and spectra in solid-state systems becomes available [141–143], control pulse optimizations tailored towards specific systems will be required to further push fidelities beyond the error correction threshold [144, 145]. This calls for flexible and generically applicable tools as a basis for the numerical optimization of pulses as well as the detailed analysis of the quantum processes they effect. In order to obtain a useful description also for gate operations that decouple from leading orders of noise, such as dynamically corrected gates (DCGs) [146], beyond leading order results are required.

In Reference 124 we presented a formalism based on filter functions and the Magnus expansion (ME) that addresses these needs and limitations of the canonical master equation approach for correlated noise. Specifically, we showed how process descriptions can be obtained perturbatively for arbitrary classical noise spectra and derived a concatenation rule to obtain the filter function of a sequence of gates from those of the individual gates. This work generalizes and extends these results.

Filter functions (FFs) were originally introduced to describe the decay of phase coherence under dynamical decoupling (DD) sequences [147–150] consisting of wait times and perfect π -pulses. The formalism facilitated recognizing these sequences as band-pass filters that allow for probing the environmental noise characteristics of a quantum system through noise spectroscopy [143, 151–153] or optimizing sequences to suppress specific noise bands [143, 154–156]. It can also be extended to fidelities of gate operations for single [157, 158] or multiple [159, 160] qubits using the ME [161, 162] as well as more general DD protocols [163]. The works by Green et al. [158] and Clausen, Bensky, and Kurizki [164] also introduced the notion of the control matrix as a quantity closely related to the canonical filter function that is convenient for calculations. In this context, the formalism’s capability to predict fidelities of gate implementations has been identified and experimentally tested [156, 158, 165, 166]. More recently, it has also proved useful in assessing the performance requirements for classical control electronics [167].

While analytical approaches allow for the calculation of filter functions of arbitrary quantum control protocols in principle, it is in practice often a tedious task to determine analytical solutions to the integrals involved if the complexity of the applied wave forms goes beyond simple square pulses or extends to multiple qubits. Moreover, one does not always have a closed-form expression of the control at hand, such as is the case for numerically optimized control pulses. This calls for a numerical approach which, while giving up some of the insights an analytical form offers, is universally applicable and eliminates the need for laborious analytical calculations.

Here, we build and extend upon our work of Reference 124 and that of Reference 158 to show that the formalism can be recast within the framework of stochastic Liouville equations by means of the cumulant expansion [126, 127, 168, 169].

We investigate the accuracy of the expansion in Chapter 17. For Gaussian noise commuting with the control, this entails exact results for the quantum process of an arbitrary control operation using only first and second order terms of the ME [161]. Moreover, due to the fact that the ME retains the algebraic structure of the expanded quantity [162] we are able to separate incoherent and coherent contributions to the quantum

process. We give explicit methods to evaluate these terms for piecewise-constant control pulses. Moreover, we show that the formalism naturally lends itself as a tool for numerical calculations and present the `filter_1` functions Python software package that enables calculating the filter function of arbitrary, piecewise constant defined pulses [170]. On top of providing methods to handle individual quantum gates, the package also implements the concatenation operation as well as parallelized execution of pulses on different groups of qubits, allowing for a highly modular and hence computationally powerful treatment of quantum algorithms in the presence of correlated noise. Given an arbitrary, classical noise spectral density, it can be used to calculate a matrix representation of the error process. From this matrix one can extract average gate fidelities, transition probabilities, and leakage rates as we derive below. To simplify adaptation the software's Application Programming Interface (API) is strongly inspired by and compatible with `QuTiP` [171] as well as `qopt` [172]. This allows users to use these packages in conjunction. Assessing the computational performance, we show that our method outperforms Monte Carlo (MC) simulations for single gates. New analytical results applicable to periodic Hamiltonians and employing the concatenation property make this advantage even more pronounced for sequences of gates. To highlight the main software features, we show example applications below.

We provide this package in the expectation that it will be a useful tool for the community. Besides recasting and expanding on our earlier introduction of the formalism in Reference 124, the present work is intended to provide an overview of the software and its capabilities. It is structured as follows: In Chapter 16 we derive a closed-form expression for unital quantum operations in the presence of non-Markovian Gaussian noise and lay out how it may be evaluated using the filter-function formalism. We review the concatenation of quantum operations shown in Reference 124 and furthermore adapt the method by Green et al. [158] to calculate the filter function of an arbitrary control sequence numerically. We will specifically focus on computational aspects of the formalism and lay out how to compute various quantities of interest. Moreover, we classify its computational complexity for calculating average gate fidelities and remark on simplifications that allow for drastic improvements in performance in certain applications. In Chapter 18, we introduce the software package by outlining the programmatic structure and giving a brief overview over the API. Lastly, in Chapter 19, we show the application of the software by means of four examples that highlight various features of the formalism and its implementation. Therein, we first demonstrate that the formalism can predict average gate fidelities for complex two-qubit quantum gates in agreement with computationally much more costly MC calculations. Next, we show how it can be applied to periodically driven systems to efficiently analyze Rabi oscillations. We finally establish the formalism's ability to predict deviations from the simple concatenation of unitary gates for sequences and algorithms in the presence of correlated noise by simulating a randomized benchmarking (RB) experiment as well as assembling a quantum Fourier transform (QFT) circuit from numerically optimized gates. We conclude by briefly remarking on possible future application and extension of our method in Chapter 20.

Throughout this part we will denote Hilbert-space operators by Roman font, *e.g.* U , and quantum operations and their representations as transfer matrices in Liouville space by calligraphic font, *e.g.* \mathcal{U} , which we also use for the control matrix $\tilde{\mathcal{B}}$ to emphasize its innate connection to a transfer matrix. For consistency, a unitary quantum operation will share the same

character as the corresponding unitary operator. An operator in the interaction picture will furthermore be designated by an overset tilde, *e.g.* $\tilde{H} = U^\dagger H U$ with U the unitary operator defining the co-moving frame. Definitions of new quantities on the left and right side of an equality are denoted by $:=$ and $=$, respectively. We use a central dot (\cdot) as a placeholder in some definitions of abstract operators such as the Liouvillian, denoted by $\mathcal{L} := [H, \cdot]$, which is to be understood as the commutator of the corresponding Hamiltonian H and the operator that \mathcal{L} acts on. The identity matrix is denoted by $\mathbb{1}$ and its dimension always inferred from context. Furthermore, we will use Greek letters for indices that correspond to noise operators in order to distinguish them clearly from those that correspond to basis or matrix elements. Lastly, we work in units where $\hbar = 1$.

Filter-function formalism for unital quantum operations

16

WE begin the mathematical part by showing how a superoperator matrix representation of the error process, the *error transfer matrix*, of a unital quantum operation can be computed from the control matrix of the pulse implementing the operation. The control matrix relates the operators through which noise couples into the system to a set of basis operators in the interaction picture and we detail how it can be calculated in a relatively efficient manner for two different situations. First, we consider a sequence of gates whose control matrices have been precomputed. Second, we lay out how the control matrix can be obtained from scratch under the assumption of piecewise-constant control, which is often convenient for approximating continuous pulse shapes. Other wave forms can be dealt with analogously by solving the corresponding integrals. We then move on to show how several quantities of interest can be extracted and present optimized strategies for computing the central objects of the formalism.

16.1 Transfer matrix representation of quantum operations

16.1.1 Brief review of quantum operations and superoperators

The quantum operations formalism provides a general framework for the description of open quantum systems [55, 173]. It forms the mathematical basis for quantum process tomography (QPT) [174, 175] as well as gate set tomography (GST) [176, 177] and has also been extensively employed in the context of RB [178, 179]. Several different representations of quantum operations exist. While all of them are equivalent one typically chooses the most convenient for the problem at hand. For an overview of the most commonly used representations see Reference 177 and for matrix representations in particular Reference 180 and the references therein. In this work we employ the Liouville representation, to the best of our knowledge first formalized by Fano [181], to profit from its simple properties under composition. It is also known as the transfer matrix representation and we will use the terms interchangeably below. We now briefly review the concept and refer the reader to the literature for further details. Concretely, the Liouville representation of an operation $\mathcal{E} : \rho \rightarrow \mathcal{E}(\rho)$ acting on density operators in a Hilbert space \mathcal{H} of dimension d is given by

$$\mathcal{E}_{ij} \doteq \text{tr}(C_i^\dagger \mathcal{E}(C_j)) \quad (16.1)$$

with an operator basis $C = \{C_0, C_1, \dots, C_{d^2-1}\}$ for the space of linear operators over \mathcal{H} , $L(\mathcal{H})$, orthonormal with respect to the Hilbert-Schmidt product $\langle A, B \rangle := \text{tr}(A^\dagger B)$. In the case that the operator basis corresponds to the Pauli matrices Equation 16.1 is known as the Pauli transfer matrix (PTM). The operation \mathcal{E} is thus associated with a $d^2 \times d^2$ matrix in *Liouville space* \mathcal{L} that describes its action as the degree to which the j th basis element is mapped onto the i th. On \mathcal{L} one can identify a set of basis kets $\{|C_i\rangle\rangle_{i=0}^{d^2-1} = \{|i\rangle\rangle_{i=0}^{d^2-1}$ isomorphic to the operators C_i (and correspondingly

bras $\langle\langle i|$ to the adjoint C_i^\dagger) as well as the inner product $\langle\langle i|j\rangle\rangle = \langle C_i, C_j \rangle$. As the vectors $|i\rangle\rangle$ form an orthonormal basis, any operator on \mathcal{H} can be written as a vector on \mathcal{L} , $|A\rangle\rangle = \sum_i |i\rangle\rangle \langle\langle i|A\rangle\rangle$, whereas a superoperator on \mathcal{H} becomes a matrix on \mathcal{L} , see Equation 16.1. It can then be shown that density operators represented by vectors are propagated by transfer matrices so that the action of a quantum operation \mathcal{E} on a density operator ρ is given by $|\mathcal{E}(\rho)\rangle\rangle = \mathcal{E}|\rho\rangle\rangle = \sum_{ij} |\mathcal{E}|_{ij} |i\rangle\rangle \langle\langle j|\rho\rangle\rangle$. Thus, the composition of two operations \mathcal{E}_1 and \mathcal{E}_2 corresponds to matrix multiplication in Liouville space, $[\mathcal{E}_2 \circ \mathcal{E}_1]_{ik} = \sum_j [\mathcal{E}_2]_{ij} [\mathcal{E}_1]_{jk}$, a property which makes the representation particularly attractive for sequences of operations. Although from a numerical perspective the computational complexity scales unfavorably with the system dimension d (cf. Section 16.9), we will employ the Liouville representation for its transparent interpretation and concise behavior under composition in the following analytical considerations. Lastly, we note that for $C_0 \propto \mathbb{1}$, trace-preservation and unitality are encoded in the relations $\mathcal{E}_{0j} = \delta_{0j}$ and $\mathcal{E}_{j0} = \delta_{j0}$, respectively.

16.1.2 Liouville representation of the error channel

We will now derive an expression for the quantum process of a quantum gate in the presence of arbitrary classical noise. As a single realization of a classical noise generates strictly unitary dynamics, we will be interested in the expectation value of the dynamics over many such realizations, which will lead to a quantum process including decoherence. If the noise is additionally Gaussian, these results are exact and therefore apply without restrictions to arbitrarily large noise strength as well as to gates that partially decouple from noise. For such DCGs or DD sequences [146, 150] higher order terms can become dominant. In the case that the environment is not strictly Gaussian, our approach becomes perturbative and we recover the results presented in Reference 124. As most of our discussion later on in this part will focus on the approximation neglecting coherent errors, readers not interested in the full generality may refer to that publication for a less general but perhaps more accessible derivation and skip ahead to Section 16.2.

The difference is that in Reference 124, the Magnus expansion is applied to the solution of the Schrödinger equation, whereas the approach presented here is based on the theory of stochastic Liouville equations and the cumulant expansion [126, 168]. In the filter function context, the cumulant expansion has been used to express the decay of the off-diagonal terms of a single-qubit density matrix in Reference 150. More recently, Paz-Silva and Viola [163] employed it in conjunction with the ME to obtain the matrix elements of the perturbed density operator after a time T of noisy evolution. In Reference 182, the authors made use of the cumulant expansion and stochastic Liouville equations for the purpose of gate optimization. Here, we combine different aspects of these works and make the connection to the quantum operations formalism by determining the noise-averaged error propagator in the Liouville representation. This form completely characterizes the error process and hence allows for detailed insight into the decoherence mechanisms of the operation.

Concretely, we consider a system described by the stochastic Hamilto-

nian

$$H(t) = H_c(t) + H_n(t), \quad (16.2)$$

$$H_n(t) = \sum_{\alpha} b_{\alpha}(t) B_{\alpha}(t). \quad (16.3)$$

$H_c(t)$ is implemented by the experimentalist to generate the desired control operation during the time $t \in [0, \tau]$ and $H_n(t)$ describes classical fluctuating noise environments $b_{\alpha}(t) \in \mathbb{R}$ that couple to the quantum system via the Hermitian noise operators $B_{\alpha}(t) \in \mathcal{L}(\mathcal{H})$. These may carry a general, deterministic time dependence and without loss of generality, we can require them to be traceless since any contributions proportional to the identity do not contribute to noisy evolution in any case.¹ The $b_{\alpha}(t)$ are random variables drawn from (not necessarily Gaussian) distributions with zero mean that are assumed to be independent and identically distributed (i.i.d.) both with respect to repetitions of the experiment. Note that this concept of independence does not preclude correlations between different noise sources $\alpha \neq \beta$ nor between one noise source at different times $t \neq t'$, but only serves to obtain a well-defined ensemble average. Lastly, to be able to later on relate the correlation functions of the $b_{\alpha}(t)$ to their spectral density, we require the noise fields to be wide-sense stationary, meaning that their correlation function depends only on the time difference.²

1: The identity commutes with the control Hamiltonian at all times and hence does not generate any evolution in the interaction picture in which we work later on (cf. Equation 16.13).

2: See also Sidenote 7.

For noise operators without explicit time dependence, Equation 16.3 constitutes a universal decomposition as can be seen by choosing the B_{α} from an orthonormal basis for $\mathcal{L}(\mathcal{H})$. To motivate the time-dependent form of Equation 16.3, assume the true Hamiltonian is a function of a set of noisy parameters $\tilde{\lambda}(t) = \lambda(t) + \delta\lambda(t)$ where $\delta\lambda(t) = \text{vec}(\{b_{\alpha}(t)\}_{\alpha})$ are the stochastic variables. Expanding the Hamiltonian in an orthonormal operator basis yields $H(\tilde{\lambda}(t)) = \sum_{\alpha} f_{\alpha}(\lambda(t), \delta\lambda(t)) B_{\alpha}$. In general, however, the expansion coefficients f_{α} will be arbitrary functions of both the deterministic parameters $\lambda(t)$ and the stochastic noises $\delta\lambda(t)$, which prohibits a factorized form like Equation 16.3. We can address this problem by first expanding H around $\lambda(t)$ for small fluctuations $\delta\lambda(t)$. Then, the Hamiltonian approximately becomes $H(\tilde{\lambda}(t)) \approx H(\lambda(t)) + \delta\lambda(t) \cdot \nabla_{\lambda} H(\lambda(t))$, where we can define the control Hamiltonian as $H_c(t) := H(\lambda(t))$. Expanding the second term in the operator basis now results in the form (16.3) for the noise Hamiltonian as it is linear in $\delta\lambda(t)$ and the deterministic time dependence is contained in $\nabla_{\lambda} H(\lambda(t))$ alone.

This permits us to model complex relations between physical noise sources and the noise operators that capture the coupling to the quantum system, arising for example through control hardware or effective Hamiltonians obtained from *e.g.* Schrieffer-Wolff transformations. While the linearization is in most cases an approximation, it does not impose significant constraints since the noise is typically weak compared to the control.³ As an example, we could capture a dependence of the device sensitivity on external controls (see also Reference 159). In a widely used setting electrons confined in solid-state quantum dots are manipulated using the exchange interaction J that depends non-linearly on the potential difference ϵ between two dots. Since the dominant physical noise source affecting this control is charge noise, one could include the effect on $J(\epsilon)$ to first order with $s_{\epsilon}(t) = \partial J(\epsilon(t))/\partial \epsilon(t)$ so that $H_n(t) = b_{\epsilon}(t) B_{\epsilon}(t) = b_{\epsilon}(t) s_{\epsilon}(t) B_{\epsilon}$ for some operator B_{ϵ} which represents the exchange coupling.

3: The same argument forms the basis for the perturbative approach for non-Gaussian noise.

We proceed in our derivation by noting that the control Hamiltonian H_c

gives rise to the noise-free Liouville–von Neumann equation

$$\frac{d\rho(t)}{dt} = -i[H_c(t), \rho(t)] = -i\mathcal{L}_c(t)\rho(t) \quad (16.4)$$

on the Hilbert space \mathcal{H} with the Liouvillian superoperator $\mathcal{L}_c(t)$ representing the control. Analogous to the Schrödinger equation we may also write this differential equation in terms of time evolution superoperators (superpropagators), $d\mathcal{U}_c(t)/dt = -i\mathcal{L}_c(t)\mathcal{U}_c(t)$ where the action of \mathcal{U}_c on a state ρ is to be understood as $\mathcal{U}_c : \rho \rightarrow U_c \rho U_c^\dagger$ with U_c the usual time evolution operator satisfying the corresponding Schrödinger equation. This allows us to write the superpropagator for the total Liouvillian $\mathcal{L} = \mathcal{L}_c + \mathcal{L}_n$ as $\mathcal{U}(t) = \mathcal{U}_c(t)\tilde{\mathcal{U}}(t)$ where the unitary error superpropagator $\tilde{\mathcal{U}}(t)$ contains the effect of a specific noise realization in Equation 16.3. Next, we transform the noise Liouvillian \mathcal{L}_n to the interaction picture with respect to the control Liouvillian \mathcal{L}_c so that $\tilde{\mathcal{U}}(t)$ satisfies the modified Liouville–von Neumann equation

$$\frac{d\tilde{\mathcal{U}}(t)}{dt} = -i\tilde{\mathcal{L}}_n(t)\tilde{\mathcal{U}}(t), \quad (16.5)$$

$$\tilde{\mathcal{L}}_n(t) = \mathcal{U}_c^\dagger(t)\mathcal{L}_n(t)\mathcal{U}_c(t). \quad (16.6)$$

Equation 16.5 may be formally solved using the Magnus expansion [161] so that at time $t = \tau$

$$\tilde{\mathcal{U}}(\tau) = \exp\{-i\tau\mathcal{L}_{\text{eff}}(\tau)\} \quad (16.7)$$

with $\mathcal{L}_{\text{eff}}(\tau) = \sum_{n=1}^{\infty} \mathcal{L}_{\text{eff},n}(\tau)$. A sufficient criterion for the convergence of the expansion is given by Moan, Oteo, and Ros [183] as $\int_0^\tau dt \|\tilde{\mathcal{L}}_n(t)\| < \pi$ where $\|\cdot\| = \sqrt{\langle \cdot, \cdot \rangle}$ is the Frobenius (Hilbert-Schmidt) norm. The first and second terms of the ME are given by [161, 162]

$$\mathcal{L}_{\text{eff},1}(\tau) = \frac{1}{\tau} \int_0^\tau dt \tilde{\mathcal{L}}_n(t), \quad (16.8a)$$

$$\mathcal{L}_{\text{eff},2}(\tau) = -\frac{i}{2\tau} \int_0^\tau dt_1 \int_0^{t_1} dt_2 [\tilde{\mathcal{L}}_n(t_1), \tilde{\mathcal{L}}_n(t_2)]. \quad (16.8b)$$

The n th term of the expansion contains n factors of the noise variables $b_\alpha(t)$ and scales with n factors of the control duration τ , suggesting that higher-order terms can be neglected if their product is small. In the Bloch sphere picture this corresponds to requiring that the angle by which the Bloch vector is rotated away from its intended trajectory due to the noise be small. Below, we will use the parameter ξ to denote the magnitude of this deviation. It is properly defined in Subsection E.4.1 where also bounds for the convergence of the ME are discussed. Here, we only state that $\mathcal{L}_{\text{eff},n} \sim \xi^n$ (see also Reference 158).

We have suggestively written the ME in terms of an effective Liouvillian $\mathcal{L}_{\text{eff}} = [H_{\text{eff}}, \cdot]$ to interpret it as the generator of a *time*-averaged evolution of a single noise realization up to time τ . In order to obtain the *ensemble*-averaged evolution of many realizations of the stochastic Hamiltonian in Equation 16.3, we apply the cumulant expansion to $\tilde{\mathcal{U}}$ (see also References 184 and 185),

$$\langle \tilde{\mathcal{U}}(\tau) \rangle = \langle \exp\{-i\tau\mathcal{L}_{\text{eff}}(\tau)\} \rangle =: \exp \mathcal{K}(\tau) \quad (16.9)$$

with $\langle \cdot \rangle$ denoting the ensemble average⁴ and the cumulant function [126]

4: The ensemble average represents the expectation value over identical repetitions of an operation in an experiment. It can be taken to be a spatial ensemble of many identical systems, *e.g.* an NMR system, or, for ergodic systems, a time ensemble of a single system under stationary noise as would be the case for a single spin measured repeatedly, for instance.

$$\mathcal{K}(\tau) = \sum_{k=1}^{\infty} \frac{(-i\tau)^k}{k!} \langle \mathcal{L}_{\text{eff}}(\tau)^k \rangle_c \quad (16.10)$$

$$= \sum_{k=1}^{\infty} \frac{(-i\tau)^k}{k!} \left\langle \left[\sum_{n=1}^{\infty} \mathcal{L}_{\text{eff},n}(\tau) \right]^k \right\rangle_c. \quad (16.11)$$

The notation $\langle \cdot \rangle_c$ denotes the cumulant average which prescribes a certain averaging operation. The first cumulant of a set of random variables $\{X_i(t)\}_i$ is simply the expectation value, $\langle X_i(t) \rangle_c = \langle X_i(t) \rangle$, whereas the second cumulant corresponds to the covariance, $\langle X_i(t)X_j(t) \rangle_c = \langle X_i(t)X_j(t) \rangle - \langle X_i(t) \rangle \langle X_j(t) \rangle$. Remarkably, third and higher-order cumulants vanish for Gaussian processes [168, 186], making Equation 16.11 exact by truncating the sums already at $k = 2$ and $n = 2$. In this case, the convergence radius of the ME becomes infinite. The terms with $k = n = 2$ do not contribute as they involve fourth-order cumulants. Since furthermore we assume that the noise fields $b_\alpha(t)$ have zero mean, also the terms with $k = n = 1$ vanish and $\langle X_i(t)X_j(t) \rangle_c = \langle X_i(t)X_j(t) \rangle$. We can hence write the cumulant function succinctly as

$$\mathcal{K}(\tau) = -i\tau \langle \mathcal{L}_{\text{eff},2}(\tau) \rangle - \frac{\tau^2}{2} \langle \mathcal{L}_{\text{eff},1}(\tau)^2 \rangle. \quad (16.12)$$

Equations 16.9 and 16.12 allow us to exactly compute the full quantum process $\langle \tilde{\mathcal{U}} \rangle : \rho \rightarrow \langle \tilde{\mathcal{U}}(\rho) \rangle$ for Gaussian noise with arbitrary spectral density and power. For non-Gaussian noise these expressions are approximate up to $\mathcal{O}(\xi^2)$ and higher order terms include both higher orders of the ME and the cumulant expansion. Inspecting Equation 16.12, we observe that the first term is anti-Hermitian as it is a pure Magnus term⁵ and thus generates unitary, coherent time evolution. Conversely, the second term is Hermitian and thus generates decoherence.⁶ The former is more difficult to compute than the latter because the second order of the ME, Equation 16.8b, contains nested time integrals. Arguments can be made [124], however, that for single gates in an experimental context the coherent errors captured by this term can be calibrated out to a large degree [187, 188]. Moreover, many of the central quantities of interest that can be extracted from the quantum process, among which are gate fidelities and certain measurement probabilities, are functions of only the diagonal elements of \mathcal{K} . By virtue of the antisymmetry of the second order terms, they do not contribute to these quantities to leading order as we show in Section 16.4.

While we will also lay out how to compute the second order, our discussion will therefore focus on contributions from the incoherent term below. As it turns out, this term can be computed using a filter-function formalism based on that by Green et al. [158]. To see this, we insert the explicit forms of the ME given in Equation 16.8 and the noise Hamiltonian given in Equation 16.3 into Equation 16.12. Together with $[\mathcal{L}, \mathcal{L}'] = [[H, H'], \cdot]$ and $\mathcal{L}\mathcal{L}' = [H, [H', \cdot]]$, we find that

$$\begin{aligned} \mathcal{K}(\tau) = & -\frac{1}{2} \sum_{\alpha\beta} \left(\int_0^\tau dt_1 \int_0^{t_1} dt_2 \langle b_\alpha(t_1)b_\beta(t_2) \rangle [[\tilde{B}_\alpha(t_1), \tilde{B}_\beta(t_2)], \cdot] \right. \\ & \left. + \int_0^\tau dt_1 \int_0^\tau dt_2 \langle b_\alpha(t_1)b_\beta(t_2) \rangle [\tilde{B}_\alpha(t_1), [\tilde{B}_\beta(t_2), \cdot]] \right), \end{aligned} \quad (16.13)$$

where $\tilde{B}_\alpha(t) = U_c^\dagger(t)B_\alpha(t)U_c(t)$ are the noise operators of Equation 16.3 in the interaction picture. $\langle b_\alpha(t_1)b_\beta(t_2) \rangle$ is the cross-correlation function of noise sources α and β which we will later relate to the spectral density.

5: Remember that the ME preserves algebraic structure to every order.

6: In the Liouville representation, the first term is an antisymmetric matrix that generates a rotation and the second a symmetric matrix that generates a deformation of the generalized, $d^2 - 1$ -dimensional Bloch sphere.

For now, we stay in the time domain and introduce an orthonormal and Hermitian operator basis for the Hilbert space \mathcal{H} to define the Liouville representation,

$$\mathbf{C} = \{C_k \in \mathbf{L}(\mathcal{H}) : C_k^\dagger = C_k \text{ and } \text{tr}(C_k C_l) = \delta_{kl}\}_{k=0}^{d^2-1}, \quad (16.14)$$

where we choose $C_0 = d^{-1/2} \mathbb{1}$ for convenience so that the remaining elements are traceless. In order to separate the commutators from the time-dependence and hence the integral in Equation 16.13, we expand the noise operators in this basis so that

$$\tilde{B}_\alpha(t) =: \sum_k \tilde{B}_{\alpha k}(t) C_k. \quad (16.15)$$

The expansion coefficients $\tilde{B}_{\alpha k}(t) \in \mathbb{R}$ are given by the inner product of a noise operator in the interaction picture on the one hand and a basis element on the other:

$$\tilde{B}_{\alpha k}(t) = \langle \tilde{B}_\alpha(t), C_k \rangle = \text{tr}(U_c^\dagger(t) B_\alpha(t) U_c(t) C_k). \quad (16.16)$$

In line with Green et al. [158], we call these coefficients the control matrix (see also References 189 and 164). In the transfer matrix (superoperator) picture we can take up the following interpretation for the control matrix by virtue of the cyclicity of the trace: it describes a mapping of a state, represented by the basis element C_k and subject to the control operation $\mathcal{U}_c(t) : C_k \rightarrow U_c(t) C_k U_c^\dagger(t)$, onto the noise operator $B_\alpha(t)$. That is, we can write the α th row of the control matrix as $\langle \tilde{B}_\alpha(t) | = \langle B_\alpha(t) | \mathcal{U}_c(t)$. In this connection lies the power of the FF formalism as will become clear shortly; we can first determine the ideal evolution without noise and subsequently evaluate the error process by linking the unitary control operation to the noise operators.

Having expanded the noise operators in the basis \mathbf{C} , we can already anticipate that upon substituting them, Equation 16.13 will separate into a time-dependent part involving on one hand the control matrix and cross-correlation functions and on the other a time-independent part involving commutators of basis elements. This will simplify our calculations in the following. To see this, we recall the definition of the Liouville representation in Equation 16.1 and apply it to the cumulant function so that $\mathcal{K}_{ij} = \text{tr}(C_i \mathcal{K}[C_j]) \in \mathcal{L}$, where the notation $\mathcal{K}[C_j]$ means substituting C_j for the placeholder \bullet in the commutators in Equation 16.13 and we suppressed the time argument for legibility. Finally, we insert the expanded noise operators given by Equation 16.15 and obtain the Liouville representation of the cumulant function,

$$\mathcal{K}_{ij}(\tau) =: -\frac{1}{2} \sum_{\alpha\beta} \sum_{kl} (f_{ijkl} \Delta_{\alpha\beta,kl} + g_{ijkl} \Gamma_{\alpha\beta,kl}). \quad (16.17)$$

Here, we captured the ordering of the noise operators due to the commutators in Equation 16.13 in the coefficients f_{ijkl} and g_{ijkl} . These are trivial functions of the fourth order trace tensor⁷

$$T_{ijkl} = \text{tr}(C_i C_j C_k C_l) \quad (16.18)$$

given by

$$f_{ijkl} = T_{klji} - T_{lkji} - T_{klij} + T_{lkij} \quad \text{and} \quad (16.19a)$$

$$g_{ijkl} = T_{klji} - T_{kjli} - T_{kilj} + T_{kijl}. \quad (16.19b)$$

7: Note the similarity to the relationship of a transfer matrix with the χ -matrix, $\mathcal{E}_{ij} = \sum_{kl} \chi_{kl} T_{ikjl}$, with χ_{kl} defined by $\mathcal{E}(\rho) = \sum_{kl} \chi_{kl} C_k \rho C_l$ or, in terms of the Kraus operators K_i of the quantum operation, $\chi_{kl} = \sum_i \text{tr}(K_i C_k) \text{tr}(K_i^\dagger C_l) = [\sum_i |K_i\rangle\langle K_i|]_{kl}$ [177].

Furthermore, we introduced the frequency (Lamb) shifts Δ and decay amplitudes Γ which contain all information on the noise and qubit dynamics as captured by the control matrix $\tilde{\mathcal{B}}(t)$:

$$\Delta_{\alpha\beta,kl} = \int_0^\tau dt_1 \int_0^{t_1} dt_2 \langle b_\alpha(t_1)b_\beta(t_2) \rangle \tilde{\mathcal{B}}_{\alpha k}(t_1)\tilde{\mathcal{B}}_{\beta l}(t_2), \quad (16.20)$$

$$\Gamma_{\alpha\beta,kl} = \int_0^\tau dt_1 \int_0^\tau dt_2 \langle b_\alpha(t_1)b_\beta(t_2) \rangle \tilde{\mathcal{B}}_{\alpha k}(t_1)\tilde{\mathcal{B}}_{\beta l}(t_2). \quad (16.21)$$

The frequency shifts Δ correspond to the first term in Equation 16.12, hence incurring coherent errors, *i.e.* generalized axis and overrotation errors. They reflect a perturbative correction to the quantum evolution due to a change of the Hamiltonian at two points in time, and thus time ordering matters. Conversely, the decay amplitudes Γ correspond to the second term and capture the decoherence. These terms are due to an incoherent average that only takes classical correlations into account, so that time ordering does not play a role. Note that Equation 16.17 together with Equation 16.9 constitutes an exact version (in the Liouville representation) of Eq. (4) from Reference 124 for Gaussian noise. The approximation of Reference 124 is obtained by expanding the exponential to linear order and neglecting the second order terms Δ .

For a single qubit and \mathcal{C} the Pauli basis one can make use of the simple commutation relations so that the cumulant function takes the form (see Section E.1)

$$\mathcal{K}_{ij}(\tau) = \begin{cases} -\sum_{k \neq i} \Gamma_{kk} & \text{if } i = j, \\ -\Delta_{ij} + \Delta_{ji} + \Gamma_{ij} & \text{if } i \neq j, \end{cases} \quad (16.22)$$

for $i, j > 0$ and any α, β . As mentioned in Section 16.1 the cases $j = 0$ and $i = 0$ encode trace-preservation and unitality, respectively, and as such $\mathcal{K}_{0j} = \mathcal{K}_{i0} = 0$ since our model is both trace-preserving and unital.⁸

16.2 Calculating the decay amplitudes

In order to evaluate the cumulant function $\mathcal{K}(\tau)$ given by Equation 16.17 and thus the transfer matrix $\langle \tilde{\mathcal{U}}(\tau) \rangle$ from Equation 16.9 for a given control operation, we solely require the decay amplitudes Γ_{kl} and frequency shifts Δ_{kl} since the trace tensor T_{ijkl} depends only on the choice of basis and is therefore trivial (although quite costly for large dimensions, *cf.* Section 16.8) to calculate. In this section, we describe simple methods for calculating Γ_{kl} using an extension of the filter-function formalism developed by Green et al. [158] that we introduced in Reference 124. The central quantity of interest will be the control matrix that we already introduced above. It relates the interaction picture noise operators to the operator basis and we will compute it in Fourier space in order to identify the cross-correlation functions with the noise spectral density in Equation 16.21. We distinguish between a sequence of quantum gates, as already presented in Reference 124, and a single gate. In the first case the control matrix of the entire sequence can be calculated from those of the individual gates, greatly simplifying the calculation if the latter have been precomputed. This approach gives rise to correlation terms in the expression for Γ_{kl} that capture the effects of sequencing gates. In the second case, as was shown by Green et al. [158], one can calculate the control matrix for arbitrary single pulses under the assumption of

8: Unital quantum operations map the identity to the identity (*i.e.*, the identity is a fixed point of \mathcal{E}). To violate unitality, the quantum system on \mathcal{H} needs to exchange energy with another system \mathcal{H}' , *e.g.* T_1 -relaxation, a process which cannot be described by unitary dynamics on \mathcal{H} alone. Because we average over strictly unitary operations on \mathcal{H} to obtain $\langle \tilde{\mathcal{U}} \rangle$, our model cannot capture such processes. The same line of reasoning holds for trace preservation.

piecewise-constant control and we lay out how to adapt the approach for numerical applications.

We start by noting that, because we assumed the noise fields $b_\alpha(t)$ to be wide-sense stationary, that is to say the cross-correlation functions evaluated at two different points in time t_1 and t_2 depend only on their difference $t_1 - t_2$, we can define the two-sided noise power spectral density (PSD) $S_{\alpha\beta}(\omega)$ as the Fourier transform of the cross-correlation functions $\langle b_\alpha(t_1)b_\beta(t_2) \rangle$ (see also Equation 2.11),

$$\langle b_\alpha(t_1)b_\beta(t_2) \rangle = \int_{-\infty}^{\infty} \frac{d\omega}{2\pi} S_{\alpha\beta}(\omega) e^{-i\omega(t_1-t_2)}. \quad (16.23)$$

Note that the spectrum only characterizes the noise fully in the case of Gaussian noise. For non-Gaussian components in the noise, additional polyspectra have in principle to be considered for higher-order correlation functions [129]. However, since we only discuss second-order contributions which involve two-point correlation functions here, we only need to take $S_{\alpha\beta}(\omega)$ into account. Inserting the definition of the spectral density into Equation 16.21, one finds

$$\Gamma_{\alpha\beta,kl} = \int_{-\infty}^{\infty} \frac{d\omega}{2\pi} \tilde{\mathcal{B}}_{\alpha k}^*(\omega) S_{\alpha\beta}(\omega) \tilde{\mathcal{B}}_{\beta l}(\omega) \quad (16.24)$$

with $\tilde{\mathcal{B}}(\omega) = \int_0^\tau dt \tilde{\mathcal{B}}(t) e^{i\omega t}$ the frequency-domain control matrix. Note that $\tilde{\mathcal{B}}^*(\omega) = \tilde{\mathcal{B}}(-\omega)$ because $\tilde{\mathcal{B}}(t)$ is real due to our choice of a Hermitian basis \mathcal{C} . In the above equation, the fourth-order tensor⁹

$$\mathcal{F}_{\alpha\beta,kl}(\omega) := \tilde{\mathcal{B}}_{\alpha k}^*(\omega) \tilde{\mathcal{B}}_{\beta l}(\omega) \quad (16.25)$$

is the generalized filter function that captures the susceptibility of the decay amplitudes to noise at frequency ω . For $\alpha = \beta, k = l$, and by summing over the basis elements,

$$\mathcal{F}_\alpha(\omega) = \sum_k |\tilde{\mathcal{B}}_{\alpha k}(\omega)|^2 = \text{tr}(\tilde{\mathcal{B}}_\alpha^\dagger(\omega) \tilde{\mathcal{B}}_\alpha(\omega)), \quad (16.26)$$

and this tensor reduces to the canonical *fidelity* filter function [157] from which the entanglement fidelity can be obtained, see Subsection 16.4.1. Thus, if the frequency-domain control matrix $\tilde{\mathcal{B}}_{\alpha k}(\omega)$ for noise source α and basis element k is known, the transfer matrix can be evaluated by integrating Equation 16.24. Moreover, one can study the contributions of each pair of noise sources (α, β) both separately or, at virtually no additional cost and to leading order, collectively by summing over them, $\Gamma_{kl} = \sum_{\alpha\beta} \Gamma_{\alpha\beta,kl}$.

We now discuss how to calculate the control matrix $\tilde{\mathcal{B}}(\omega)$ in frequency space for a given control operation. We focus first on sequences of quantum gates, assuming that the control matrices $\tilde{\mathcal{B}}^{(g)}(\omega)$ for each gate g have been calculated before.

16.2.1 Control matrix of a gate sequence

For a sequence of gates with precomputed interaction picture noise operators the approach developed by Green et al. [158] based on piecewise-constant control can be adapted to yield an analytical expression for those of the composite gate sequence that is computationally efficient to evaluate [124]. Here we review these results to give a complete picture of

9: Of course, we can also interpret $\mathcal{F}_{\alpha\beta}(\omega) \in \mathcal{L}$ as a linear operator (matrix) in Liouville space, and similarly $\Gamma_{\alpha\beta} \in \mathcal{L}$.

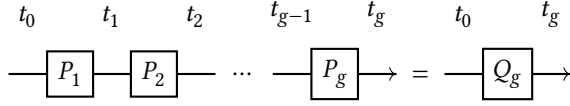


Figure 16.1: Illustration of a sequence of G gates. Individual gates with propagators P_g start at time t_{g-1} and complete at time t_g . The total action from t_0 to t_g is given by Q_g .

the formalism. While our results are general and apply to any superoperator representation, we employ the Liouville representation here for its simple composition operation: matrix multiplication. Computationally, this is not the most efficient choice since transfer matrices have dimension $d^2 \times d^2$ and thus their matrix multiplication scales unfavorably compared to, for example, left-right conjugation by unitaries (*cf.* Section 16.9). However, because the structure of the control matrix $\tilde{\mathcal{B}}$ is similar to that of a transfer matrix,¹⁰ we will obtain a particularly concise expression for the sequence in the following. For a perhaps more intuitive description employing exclusively conjugation by unitaries, we refer the reader to Reference 124.

We consider a sequence of G gates with propagators $P_g = U_c(t_g, t_{g-1})$, $g \in \{1, \dots, G\}$ that act during the g th time interval $(t_{g-1}, t_g]$ with $t_0 = 0, t_G = \tau$ as illustrated in Figure 16.1. The cumulative propagator of the sequence up to time t_g is then given by $Q_g = \prod_{g'=g}^0 P_{g'}$ with $P_0 = \mathbb{1}$ and its Liouville representation denoted by $Q^{(g)}$. Furthermore, the control matrix of the g th pulse at the time $t - t_{g-1}$ relative to the start of segment g is

$$\tilde{\mathcal{B}}_{\alpha k}^{(g)}(t - t_{g-1}) = \text{tr}(U_c^\dagger(t, t_{g-1}) B_\alpha(t - t_{g-1}) U_c(t, t_{g-1}) C_k). \quad (16.27)$$

We can now exploit the fact that in the transfer matrix picture quantum operations compose by matrix multiplication to write the total control matrix at time $t \in (t_{g-1}, t_g]$ as

$$\tilde{\mathcal{B}}(t) = \tilde{\mathcal{B}}^{(g)}(t - t_{g-1}) Q^{(g-1)} \quad (16.28)$$

since $\mathcal{U}_c(t, t_0) = \mathcal{U}_c(t, t_{g-1}) Q^{(g-1)}$ and we have that $\langle\langle \tilde{\mathcal{B}}(t) | = \langle\langle \mathcal{B}(t) | \mathcal{U}_c(t, t_0) = \langle\langle \mathcal{B}(t - t_{g-1}) | Q^{(g-1)}$. The Fourier transform of Equation 16.28 can then be obtained by evaluating the transform of each gate separately,

$$\tilde{\mathcal{B}}(\omega) = \sum_{g=1}^G e^{i\omega t_{g-1}} \tilde{\mathcal{B}}^{(g)}(\omega) Q^{(g-1)}, \quad (16.29)$$

$$\tilde{\mathcal{B}}^{(g)}(\omega) = \int_0^{\Delta t_g} dt e^{i\omega t} \tilde{\mathcal{B}}^{(g)}(t), \quad (16.30)$$

with $\Delta t_g = t_g - t_{g-1}$ the duration of gate g . Hence, calculating the control matrix of the full sequence requires only the knowledge of the temporal positions, encoded in the phase factors $e^{i\omega t_{g-1}}$, and the total intended action $Q^{(g-1)}$ of the individual pulses if their control matrices have been precomputed or obtained otherwise.¹¹ The sequence structure can thus be exploited to one's benefit. If the same gates appear multiple times during the sequence one can reuse control matrices for equal pulses to facilitate calculating filter functions for complex sequences with modest computational effort. Most importantly, Equation 16.29 is independent of the inner structure of the individual pulses and therefore takes the same time to evaluate whether they are highly complex or very simple. In Section 16.9, we will analyze the computational efficiency of capitalizing on this feature in more detail.

As we have seen, the total control matrix of a composite pulse sequence

10: Remember that it corresponds to a basis expansion of the interaction picture noise operators

11: Such as analytically.

is given by a weighted sum over the individual control matrices. Since $\tilde{\mathcal{B}}(\omega)$ enters Equation 16.24 twice, this leads to correlation terms between two gates at different positions in the sequence when computing the total decay amplitudes Γ . Inserting Equation 16.29 into Equation 16.24 gives

$$\begin{aligned} \Gamma_{\alpha\beta,kl} &= \sum_{g,g'=1}^G \int_{-\infty}^{\infty} \frac{d\omega}{2\pi} [\mathcal{Q}^{(g'-1)\dagger} \tilde{\mathcal{B}}^{(g')\dagger}(\omega)]_{k\alpha} S_{\alpha\beta}(\omega) [\tilde{\mathcal{B}}^{(g)}(\omega) \mathcal{Q}^{(g-1)}]_{\beta l} \\ &\quad \times e^{i\omega(t_{g-1} - t_{g'-1})} \\ &=: \sum_{g,g'=1}^G \int_{-\infty}^{\infty} \frac{d\omega}{2\pi} S_{\alpha\beta}(\omega) \mathcal{F}_{\alpha\beta,kl}^{(gg')}(\omega) \end{aligned} \quad (16.31)$$

$$=: \sum_{g,g'=1}^G \Gamma_{\alpha\beta,kl}^{(gg')} \quad (16.32)$$

where we defined the pulse correlation filter function $\mathcal{F}^{(gg')}(\omega)$ that captures the temporal correlations between pulses at different positions g and g' in the sequence as well as the corresponding decay amplitudes $\Gamma^{(gg')}$. Unlike regular filter functions, these can be negative for $k = l$, $g \neq g'$ and therefore reduce the overall noise susceptibility of a sequence given by $\mathcal{F}(\omega) = \sum_{gg'} \mathcal{F}^{(gg')}(\omega)$. By expanding the exponential in Equation 16.9 to linear order, the individual contributions of the pulse correlation FFs can also be traced through to derived quantities such as the infidelity [124, Equation 11]. We have thus gained a concise description of the noise-cancelling properties of gate sequences: in this picture, they arise purely from the concatenation of different pulses, quantifying, for instance, the effectiveness of DD sequences [124].

16.2.2 Control matrix of a single gate

Previous efforts have derived the control matrix analytically for selected pulses such as DD sequences [150], special dynamically corrected gates (DCGs) [159], as well as developed a general analytical framework [157, 158]. However, analytical solutions might not always be accessible, *e.g.* for numerically optimized pulses, and are generally laborious to obtain. Therefore, we now detail a method to obtain the control matrix numerically under the assumption of piecewise-constant control. Our method is similar in spirit to that of Green, Uys, and Biercuk [157] for single qubits with $d = 2$, but whereas those authors computed analytical solutions to the relevant integrals during each time step, here we use matrix diagonalization to obtain the propagator of a control operation to make the approach amenable to numerical implementation. This allows carrying out the Fourier transform of the control matrix Equation 16.16 analytically by writing the control propagators in terms of their eigenvalues in diagonal form.

We divide the total duration of the control operation, τ , into G intervals $(t_{g-1}, t_g]$ of duration Δt_g with $g \in \{0, \dots, G\}$ and $t_0 = 0, t_G = \tau$. We then approximate the control Hamiltonian as constant within each interval so that within the g

$$H_c(t) = H_c^{(g)} = \text{const.} \quad (16.33)$$

and similarly the deterministic time dependence of the noise operators as $B_\alpha(t) = s_\alpha(t) B_\alpha = s_\alpha^{(g)} B_\alpha$. Under this approximation we can diagonalize

the time-independent Hamiltonians $H_c^{(g)}$ with eigenvalues $\omega_i^{(g)}$ numerically and write the time evolution operator that solves the noise-free Schrödinger equation as $U_c(t, t_{g-1}) = V^{(g)} D^{(g)}(t, t_{g-1}) V^{(g)\dagger}$. Here, $V^{(g)}$ is the unitary matrix of eigenvectors of $H_c^{(g)}$ and the diagonal matrix $D_{ij}^{(g)}(t, t_{g-1}) = \delta_{ij} \exp\{-i\omega_i^{(g)}(t - t_{g-1})\}$ contains the time evolution of the eigenvalues. Using this result together with Q_{g-1} , the cumulative propagator up to time t_{g-1} , we can acquire the total time evolution operator at time t from $U_c(t) = U_c(t, 0) = U_c(t, t_{g-1}) Q_{g-1}$. We then substitute this relation into the definition of the control matrix, Equation 16.16, and obtain

$$\tilde{\mathcal{B}}_{\alpha k}(t) = s_{\alpha}^{(g)} \text{tr} \left(Q_{g-1}^{\dagger} V^{(g)} D^{(g)\dagger}(t, t_{g-1}) V^{(g)} B_{\alpha} \right. \\ \left. \times V^{(g)} D^{(g)}(t, t_{g-1}) V^{(g)\dagger} Q_{g-1} C_k \right) \quad (16.34)$$

$$= s_{\alpha}^{(g)} \sum_{ij} \bar{B}_{\alpha, ij}^{(g)} \bar{C}_{k, ji}^{(g)} e^{i\Omega_{ij}^{(g)}(t - t_{g-1})}, \quad (16.35)$$

where we defined $\Omega_{ij}^{(g)} = \omega_i^{(g)} - \omega_j^{(g)}$, $\bar{C}_k^{(g)} = V^{(g)\dagger} Q_{g-1} C_k Q_{g-1}^{\dagger} V^{(g)}$, and $\bar{B}_{\alpha}^{(g)} = V^{(g)\dagger} B_{\alpha} V^{(g)}$. Carrying out the Fourier transform of Equation 16.35 to get the frequency-domain control matrix of the pulse generated by the Hamiltonian from Equation 16.33 is now straightforward since the integrals involved are over simple exponential functions. We obtain

$$\tilde{\mathcal{B}}_{\alpha k}(\omega) = \sum_{g=1}^G s_{\alpha}^{(g)} e^{i\omega t_{g-1}} \text{tr} \left([\bar{B}_{\alpha}^{(g)} \circ I^{(g)}(\omega)] \bar{C}_k^{(g)} \right) \quad (16.36)$$

with $I_{ij}^{(g)}(\omega) = -i(e^{i(\omega + \Omega_{ij}^{(g)})\Delta t_g} - 1)/(\omega + \Omega_{ij}^{(g)})$ and the Hadamard product $(A \circ B)_{ij} := A_{ij} \times B_{ij}$. Equation 16.36 is readily evaluated on a computer and thus enables the calculation of filter functions of arbitrary control sequences, either on its own or in conjunction with Equation 16.29. A similar expression is obtained for representations other than the Liouville representation.

16.3 Calculating the frequency shifts

The frequency shifts $\Delta_{\alpha\beta,kl}$ in Equation 16.17 correspond to the second order of the ME and thus involve a double integral with a nested time dependence. This makes their evaluation more involved than that of the decay amplitudes $\Gamma_{\alpha\beta,kl}$ and, in contrast to the previous section, we cannot identify a concatenation rule or single out correlation terms as in Equation 16.31. However, we can still apply the approximation of piecewise-constant control and follow a similar approach as in Subsection 16.2.2 to compute Δ in Fourier space. Since these terms correspond to a coherent gate error that can in principle be calibrated out to leading order in experiments we will not go into much detail here.

We follow the arguments made above for the decay amplitudes and express the cross-correlation functions $\langle b_{\alpha}(t) b_{\beta}(t') \rangle$ by their Fourier transform, the spectral density $S_{\alpha\beta}(\omega)$, using Equation 16.23. Inserting this equation into the definition of the frequency shifts in the time domain, Equation 16.20, yields

$$\Delta_{\alpha\beta,kl} = \int_{-\infty}^{\infty} \frac{d\omega}{2\pi} S_{\alpha\beta}(\omega) \int_0^{\tau} dt \tilde{\mathcal{B}}_{\alpha k}(t) e^{-i\omega t} \int_0^t dt' \tilde{\mathcal{B}}_{\beta l}(t') e^{i\omega t'}. \quad (16.37)$$

We again assume piecewise-constant time segments so that the inner time integral can be split up into a sum of integrals over complete constant segments $(t_{g'-1}, t_{g'}]$ as well as a single integral that contains the last, incomplete segment up to time t . That is, taking the time t of the outer integral to be within the interval $(t_{g-1}, t_g]$ we perform the replacement

$$\int_0^t dt' \rightarrow \sum_{g'=1}^{g-1} \int_{t_{g'-1}}^{t_{g'}} dt' + \int_{t_{g-1}}^t dt'. \quad (16.38)$$

We have thus divided our task into two: The first term allows, as before in Subsections 16.2.1 and 16.2.2, to identify the Fourier transform of the control matrix during time steps g' and g for both the inner and the outer integral according to Equation 16.36. The second term remains a nested double integral, but now the integrand contains only products of complex exponentials because we assume the control to be constant within the limits of integration. As a next step, we also replace the outer time integral by a sum of integrals over single segments, $\int_0^t dt \rightarrow \sum_{g=1}^G \int_{t_{g-1}}^{t_g} dt$, to obtain

$$\Delta_{\alpha\beta,kl} = \int_{-\infty}^{\infty} \frac{d\omega}{2\pi} S_{\alpha\beta}(\omega) \sum_{g=1}^G \int_{t_{g-1}}^{t_g} dt \times e^{-i\omega t} \tilde{\mathcal{B}}_{\alpha k}(t) \left\{ \sum_{g'=1}^{g-1} \int_{t_{g'-1}}^{t_{g'}} dt' + \int_{t_{g-1}}^t dt' \right\} e^{i\omega t'} \tilde{\mathcal{B}}_{\beta l}(t'). \quad (16.39)$$

Before continuing, we ease notation and define $\tilde{\mathcal{B}}(\omega) =: \sum_g \mathcal{G}^{(g)}(\omega)$ with $\mathcal{G}^{(g)}(\omega)$ obtained from Equation 16.36 and furthermore adopt the Einstein summation convention for the remainder of this section, meaning multiple subscript indices that appear on only one side of an equality are summed over implicitly. We now proceed like in Subsection 16.2.2 and make use of the piecewise-constant approximation to diagonalize the control Hamiltonian during each segment. For the nested integrals, we obtain $\tilde{\mathcal{B}}_{\alpha k}(t)$ from Equation 16.35, whereas the remaining integrals factorize and we can identify the Fourier-transformed quantity $\mathcal{G}^{(g)}(\omega)$. Equation 16.39 then becomes

$$\Delta_{\alpha\beta,kl} = \int_{-\infty}^{\infty} \frac{d\omega}{2\pi} S_{\alpha\beta}(\omega) \sum_{g=1}^G \left[\mathcal{G}_{\alpha k}^{(g)*}(\omega) \sum_{g'=1}^{g-1} \mathcal{G}_{\beta l}^{(g')}(\omega) + s_{\alpha}^{(g)} \tilde{B}_{\alpha,ij}^{(g)} \tilde{C}_{k,ji}^{(g)} I_{ijmn}^{(g)}(\omega) \tilde{C}_{l,nm}^{(g)} \tilde{B}_{\beta,mn}^{(g)} s_{\beta}^{(g)} \right] \quad (16.40)$$

with $\tilde{B}_{\alpha,ij}^{(g)}, \tilde{C}_{k,ji}^{(g)}, \Omega_{ij}^{(g)}$ as defined above in Subsection 16.2.2 and

$$I_{ijmn}^{(g)}(\omega) = \int_{t_{g-1}}^{t_g} dt e^{i\Omega_{ij}^{(g)}(t-t_{g-1})-i\omega t} \int_{t_{g-1}}^t dt' e^{i\Omega_{mn}^{(g)}(t'-t_{g-1})+i\omega t'}. \quad (16.41)$$

Explicit results for the integration in Equation 16.41 are given in Subsection E.1.2. To calculate the frequency shifts Δ , we can thus reuse the quantity $\mathcal{G}^{(g)}(\omega)$ also required for the decay amplitudes Γ . The only additional computation, apart from contraction, involves the G integrations $I_{ijmn}^{(g)}(\omega)$. Importantly, Equation 16.40 has the same structure as the corresponding Equation 16.24 for Γ in that the individual entries of Δ are given by an integral over the spectral density of the noise multiplied with a – in

this case second-order – filter function that describes the susceptibility to noise at frequency ω :

$$\Delta_{\alpha\beta,kl} = \int_{-\infty}^{\infty} \frac{d\omega}{2\pi} S_{\alpha\beta}(\omega) \mathcal{F}_{\alpha\beta,kl}^{(2)}(\omega). \quad (16.42)$$

16.4 Computing derived quantities

By means of Equations 16.29, 16.36 and 16.40, one can obtain the cumulant function $\mathcal{K}(\tau)$ from Equation 16.17 and hence the error process $\langle \tilde{\mathcal{U}}(\tau) \rangle$ from Equation 16.9 for an arbitrary sequence of gates. From this, several quantities of interest for the characterization of a given control operation can be extracted. We explicitly review the average gate and state fidelities as well as expressions to quantify leakage here, but emphasize that this is not exhaustive. Because for many applications the noise is weak and hence the parameter $\xi \ll 1$, we will in the following expand the exponential in Equation 16.7 to leading order in ξ in the following. That is, we approximate¹²

$$\langle \tilde{\mathcal{U}}(\tau) \rangle \approx \mathbb{1} + \mathcal{K}(\tau). \quad (16.43)$$

12: Remember that $\mathcal{K}(\tau) \in \mathcal{O}(\xi^2)$.

For Gaussian noise, higher order corrections can be obtained either by explicitly calculating higher powers of \mathcal{K} or by numerically evaluating the exponential of the cumulant function. The former method often leads to simpler expressions than Equation 16.17 for which the trace tensor T_{ijkl} need not be computed directly. In the weak-noise regime, one can also define specific filter functions for each derived quantity that are given in terms of linear combinations of the generalized filter functions $\mathcal{F}_{\alpha\beta,kl}(\omega)$. The ensemble expectation value of the quantity can then be obtained directly from the overlap with the spectral density, $\int d\omega / 2\pi \mathcal{F}(\omega) S(\omega)$. Finally, we will drop the averaging brackets and the argument of the error transfer matrix $\langle \tilde{\mathcal{U}}(\tau) \rangle$ for brevity in the following.

16.4.1 Average gate and entanglement fidelity

The average gate fidelity is a commonly-quoted figure of merit used to characterize physical gate implementations [135, 139, 190–192]. It represents the fidelity between an implementation \mathcal{U} and the ideal gate \mathcal{Q} averaged over the uniform Haar measure. Since $F_{\text{avg}}(\mathcal{U}, \mathcal{Q}) = F_{\text{avg}}(\mathcal{Q}^\dagger \circ \mathcal{U}, \mathbb{1}) = F_{\text{avg}}(\tilde{\mathcal{U}})$, the average gate fidelity can be obtained from the error channel $\tilde{\mathcal{U}}$ as [193, 194]

$$F_{\text{avg}}(\tilde{\mathcal{U}}) = \frac{\text{tr } \tilde{\mathcal{U}} + d}{d(d+1)} \quad (16.44)$$

$$=: \frac{d \times F_{\text{ent}}(\tilde{\mathcal{U}}) + 1}{d+1}, \quad (16.45)$$

where d is the system dimension and $F_{\text{ent}}(\tilde{\mathcal{U}}) = d^{-2} \text{tr } \tilde{\mathcal{U}}$ is the entanglement fidelity. In the low-noise regime where Equation 16.43 holds, we can write the entanglement fidelity in terms of the cumulant function

$\mathcal{K}_{\alpha\beta}$ approximately as

$$F_{\text{ent}}(\tilde{\mathcal{U}}) = 1 + \frac{1}{d^2} \sum_{\alpha\beta} \text{tr } \mathcal{K}_{\alpha\beta} \quad (16.46)$$

$$=: 1 - \sum_{\alpha\beta} I_{\alpha\beta}(\tilde{\mathcal{U}}). \quad (16.47)$$

Here, we defined $I_{\alpha\beta}$, the infidelity due to a pair of noise sources (α, β) . As we show in Subsection E.1.3, we can simplify the trace of the cumulant function so that the infidelity reads

$$I_{\alpha\beta} = \frac{1}{d} \text{tr } \Gamma_{\alpha\beta}. \quad (16.48)$$

Equation 16.48 reduces to Equation 32 from Reference 157 for a single qubit ($d = 2$) and pure dephasing noise up to a different normalization convention; by pulling the trace through to the generalized filter function $\mathcal{F}_{\alpha\beta,kl}(\omega)$ in Equation 16.24, we recover the relation (setting $\alpha = \beta$ for simplicity)

$$I_{\alpha} = \frac{1}{d} \int_{-\infty}^{\infty} \frac{d\omega}{2\pi} S_{\alpha}(\omega) \mathcal{F}_{\alpha}(\omega) \quad (16.49)$$

with the fidelity filter function $\mathcal{F}_{\alpha}(\omega)$ given by Equation 16.26. Notably, only the decay amplitudes Γ contribute to the fidelity to leading order since the frequency shifts Δ are antisymmetric and therefore vanish under the trace.

16.4.2 State fidelity and measurements

In the context of quantum information processing we are often interested in the probability of measuring the expected state during readout. We can extract this projective readout probability from the transfer matrix in Equation 16.7 by inspecting the transition probability, or state fidelity, between a pure state $\rho = |\psi\rangle\langle\psi|$ and an arbitrary state σ that evolves according to the quantum operation $\mathcal{E} : \sigma \rightarrow \mathcal{E}(\sigma)$. Using the double bracket notation introduced at the beginning of Chapter 16 we then define the state fidelity as

$$\begin{aligned} F(|\psi\rangle, \mathcal{E}(\sigma)) &= \text{tr}(\rho \mathcal{E}(\sigma)) \\ &= \langle\langle \rho | \mathcal{E}(\sigma) \rangle\rangle \\ &= \langle\langle \rho | \mathcal{E} | \sigma \rangle\rangle, \end{aligned} \quad (16.50)$$

where we have expressed the density matrices by vectors and \mathcal{E} as a transfer matrix on the Liouville space \mathcal{L} . We can thus calculate arbitrary pure state fidelities by simple matrix-vector multiplications of the transfer matrices $\mathcal{E} = \mathcal{Q}\tilde{\mathcal{U}}$ and the vectorized density matrices $|\rho\rangle\rangle$ and $|\sigma\rangle\rangle$. In Section 19.3 we employ this measure to simulate a RB experiment where return probabilities are of interest so that $F(|\psi\rangle, \mathcal{E}(\rho)) = \langle\langle \rho | \mathcal{Q}\tilde{\mathcal{U}} | \rho \rangle\rangle$.

General measurements can be incorporated in the superoperator formalism we have employed here in a straightforward manner using the positive operator-valued measure (POVM) formalism [177, 195]. POVMs constitute a set of Hermitian, positive semidefinite operators $\{E_i\}$ (in contrast to the projective measurement $\{|\psi\rangle\langle\psi|, \mathbb{1} - |\psi\rangle\langle\psi|\}$) that fulfill the completeness relation $\sum_i E_i = \mathbb{1}$ and in the double bracket notation may be represented as the row vectors $\langle\langle E_i | \rangle\rangle$ in Liouville space. Consequently, the measurement probability for outcome E_i is given by $\langle\langle E_i | \mathcal{E}(\sigma) \rangle\rangle = \langle\langle E_i | \mathcal{E} | \sigma \rangle\rangle$ if the system was prepared in the state σ and evolved according to \mathcal{E} .

16.4.3 Leakage

In many physical implementations qubits are not encoded in real two-level systems but in two levels of a larger Hilbert space (superconducting transmon [196] or singlet-triplet [197] spin qubits for example) such that population can leak between this computational subspace and other energy levels. Thus, it is often of interest to quantify leakage when assessing gate performance. Recently, Wood and Gambetta [198] have suggested two separate measures for quantifying leakage out of the computational subspace on the one hand and seepage into the subspace on the other. With the filter-function formalism and the transfer matrix of the error process given by Equations 16.7 and 16.17, we can easily extract these quantities.

Using the definitions from Reference 198 and the double bracket notation we can write the leakage rate generated by a quantum operation \mathcal{E} as

$$L_c(\mathcal{E}) := \frac{1}{d_c} \langle\langle \Pi_c | \mathcal{E} | \Pi_c \rangle\rangle \quad (16.51a)$$

and the seepage rate as

$$L_\ell(\mathcal{E}) := \frac{1}{d_\ell} \langle\langle \Pi_\ell | \mathcal{E} | \Pi_\ell \rangle\rangle. \quad (16.51b)$$

Here, $\Pi_{c,\ell}$ are projectors onto the computational and leakage subspaces, respectively, and $d_{c,\ell}$ the corresponding dimensions. For unital channels the leakage and seepage rates are not independent but satisfy $d_c L_c = d_\ell L_\ell$ [198] so that we only need to consider one of the above expressions here (*cf.* Subsection 16.1.2).

Equations 16.51a and 16.51b can be used to determine both coherent and incoherent leakage separately by substituting \mathcal{Q} or \mathcal{U} , respectively, for \mathcal{E} . While the former is due to systematic errors of the applied pulse and could thus be corrected for by calibration, the latter is induced by noise only. Alternatively, the leakage from both contributions can also be determined collectively by substituting \mathcal{U} for \mathcal{E} .

16.5 Performance analysis and efficiency improvements

In this section we focus on computational aspects of the formalism, remarking first on several mathematical simplifications that make the calculation of control matrices and decay amplitudes more economical. Following this, we investigate the computational complexity of the method in comparison with MC techniques and show that our software implementation surpasses the latter's performance in relevant parameter regimes.

16.6 Periodic Hamiltonians

If the control Hamiltonian is periodic, that is $H_c(t) = H_c(t + T)$, we can reduce the computational effort of calculating the control matrix by potentially orders of magnitude (see Section 19.2 for an application in Rabi driving). We start by making the following observations: First, the frequency-domain control matrix of every period of the control is the

same so that $\tilde{\mathcal{B}}^{(g)}(\omega) = \tilde{\mathcal{B}}^{(1)}(\omega)$. Moreover, $e^{i\omega\Delta t_g} = e^{i\omega T}$ for all g so that $e^{i\omega t_{g-1}} = e^{i\omega T(g-1)}$ and by the composition property of transfer matrices $Q^{(g-1)} = [Q^{(1)}]^{g-1}$ where the superscript without parentheses denotes matrix power. We can then simplify Equation 16.29 to read

$$\tilde{\mathcal{B}}(\omega) = \tilde{\mathcal{B}}^{(1)}(\omega) \sum_{g=0}^{G-1} [e^{i\omega T} Q^{(1)}]^g. \quad (16.52)$$

Furthermore, if the matrix $\mathbb{1} - e^{i\omega T} Q^{(1)}$ is invertible, which is typically the case for the vast majority of values of ω , the previous expression can be rewritten as

$$\tilde{\mathcal{B}}(\omega) = \tilde{\mathcal{B}}^{(1)}(\omega) (\mathbb{1} - e^{i\omega T} Q^{(1)})^{-1} (\mathbb{1} - [e^{i\omega T} Q^{(1)}]^G) \quad (16.53)$$

by evaluating the sum as a finite Neumann series. Equation 16.53 offers a significant performance benefit over regular concatenation in the case of many periods G as we will show in Section 16.9. Beyond numerical advantages, it also provides an analytical method for studying filter functions of periodic driving Hamiltonians.

16.7 Extending Hilbert spaces

Examining Equation 16.16, we can see that the columns of the control matrix and therefore also the filter function are invariant (up to normalization) under an extension of the Hilbert space. This allows parallelizing pulses with precomputed control matrices in a very resource-efficient manner if one chooses a suitable operator basis. Note that the same also applies to other representations of quantum operations.

Suppose we extend the Hilbert space \mathcal{H}_1 of a gate for which we have already computed the control matrix by a second Hilbert space \mathcal{H}_2 so that $\mathcal{H}_{12} = \mathcal{H}_1 \otimes \mathcal{H}_2$. If we can find an operator basis whose elements separate into tensor products themselves, *i. e.* $C_{12} = C_1 \otimes C_2$ as for the Pauli basis (*cf.* Section 16.8), the control matrix of the composite gate defined on \mathcal{H}_{12} has the same non-trivial columns as that of the original gate on \mathcal{H}_1 up to a different normalization factor. The remaining columns are simply zero. This is because the trace over a tensor product factors into traces over the individual subsystems so that $\tilde{\mathcal{B}}_{\alpha k}(t) \propto \text{tr}([U_1^\dagger \otimes U_2^\dagger][B_\alpha \otimes \mathbb{1}][U_1 \otimes U_2][\mathbb{1} \otimes C_k]) = \text{tr}(U_1^\dagger B_\alpha U_1 \mathbb{1}) \text{tr}(U_2^\dagger \mathbb{1} U_2 C_k) = 0$ since we assumed that the noise operators B_α are traceless (*cf.* Subsection 16.1.2).

Generalizing this result to multiple originally disjoint Hilbert spaces we write the composite space as $\mathcal{H} = \bigotimes_i \mathcal{H}_i$ and the corresponding basis as $C = \bigotimes_i C_i$. The control matrix of the composite pulse on \mathcal{H} is then a combination of the columns of the control matrices on \mathcal{H}_i for noise operators B_α that are non-trivial, *i. e.* not the identity, only on their original space. For noise operators defined on more than one subspace, *e. g.* $B_{ij} = B_i \otimes B_j$, $B_i \in \mathcal{H}_i$, $B_j \in \mathcal{H}_j$, this evidently holds only for those basis elements that are trivial on either of the subspaces and the columns in the composite control matrix corresponding to non-trivial basis elements ($C_k \otimes C_l : C_k, C_l \neq \mathbb{1}$) need to be computed from scratch.

One can thus reuse precomputed control matrices beyond the concatenation laid out above when studying multi-qubit pulses or algorithms. For concreteness, consider a set of one- and two-qubit pulses whose control

matrices have been precomputed. We can then remap those control matrices to any other qubit in a larger register if the entire Hilbert space is defined by the tensor product of the single-qubit Hilbert spaces, and even map the control matrices of two different pulses to the same time slot on different qubits. Thus, we do not need to perform the possibly costly computation of the control matrices again but instead only need to remap the columns of $\hat{\mathcal{B}}$ to the equivalent basis elements in the basis of the complete Hilbert space, making the assembly of algorithms that consist of a limited set of gates which are used at several points in the algorithm more efficient. In Section 19.4 we simulate a four-qubit QFT algorithm making use of the shortcuts described here.

16.8 Operator bases

Up to this point, we have not explicitly specified the basis that defines the Liouville representation. The only conditions imposed by Equation 16.14 are orthonormality with respect to the Hilbert-Schmidt product and that the basis elements are Hermitian. Yet, the choice of operator basis can have a large impact on the time it takes to compute the control matrix as discussed in the previous section. We therefore give a short overview over two possible choices in the following. As we are mostly interested in the computational properties, we represent linear operators in $L(\mathcal{H})$ as matrices on $\mathbb{C}^{d \times d}$.

The n -qubit Pauli basis fulfills the requirements set by Equation 16.14 and furthermore allows for the simplifications described before. In our normalization convention where $\langle C_i, C_i \rangle = \mathbb{1}$ it can be written as

$$P_n := \{\sigma_i\}_{i=0}^{d^2-1} = 2^{-\frac{n}{2}} \times \{\mathbb{1}, \sigma_x, \sigma_y, \sigma_z\}^{\otimes n} \quad (16.54)$$

with the Pauli matrices σ_x, σ_y and σ_z . While it is obvious that it is separable, meaning it factors into tensor products of the single-qubit Pauli matrices, the dimension of the Pauli basis is restricted to powers of two, $d = 2^n$. An operator basis without this restriction is the generalized Gell-Mann (GGM) basis [199, 200]. In the following we will discuss optimizations pertaining to this basis that are also implemented in the software (see Chapter 18).

The GGM matrices are a generalization of the Gell-Mann matrices known from particle physics to arbitrary dimensions. In our normalization convention, the basis (excluding the identity element) is given by [201]

$$\Lambda_d := \{\Lambda_i\}_{i=1}^{d^2-1} = \{u_{jk}, v_{jk}, w_l\}_{j,k,l} \quad (16.55)$$

with

$$u_{jk} = \frac{1}{\sqrt{2}} (|j\rangle\langle k| + |k\rangle\langle j|), \quad (16.55a)$$

$$v_{jk} = -\frac{i}{\sqrt{2}} (|j\rangle\langle k| - |k\rangle\langle j|), \quad (16.55b)$$

$$w_l = \frac{1}{\sqrt{l(l+1)}} \left(\sum_{m=1}^l |m\rangle\langle m| - l|l+1\rangle\langle l+1| \right), \quad (16.55c)$$

for $1 \leq j < k \leq d$, $1 \leq l \leq d-1$, and an orthonormal vector basis $\{|j\rangle\}_{j=1}^d$ of the Hilbert space. Expanding an arbitrary matrix $A \in \mathbb{C}^{d \times d}$ in the basis

of Equation 16.55 is then simply a matter of adding up the corresponding matrix elements of A according to Equations 16.55a to 16.55c. For instance, the expansion coefficient for the first symmetric basis element is given by $u_{12} = 2^{-1/2}(A_{12}|1\rangle\langle 2| + A_{21}|2\rangle\langle 1|)$. The explicit construction prescription of the GGM basis thus allows calculating inner products of the form $\langle \Lambda_j | A \rangle$ at constant cost instead of the quadratic cost of the trace of a matrix product, speeding up the computation of the transfer matrix from Equation 16.1 (in which case $A = \mathcal{E}(\Lambda_k)$). In numerical experiments, calculating the transfer matrix of a unitary U with dimension d and pre-computed matrix products $A_k = U\Lambda_k U^\dagger$ scaled as $\sim d^{4.16}$. This agrees with the expected scaling of $\sim d^4$ (a transfer matrix has $d^2 \times d^2$ elements) and presents a significant improvement over the explicit calculation with trace overlaps $\text{tr}(\Lambda_j A_k)$ that we observed to scale as $\sim d^{5.93}$ (we expected $\sim d^6$).

Further inspection of the GGM basis additionally reveals an increasing sparsity for large d (the filling factor scales roughly with d^{-2}), so that it is well suited for computing the trace tensor Equation 16.18. Since this tensor has d^8 elements, the amount of memory required for a dense representation becomes unreasonably large quite quickly. To overcome this constraint, we can use a GGM basis instead of a dense basis like the Pauli basis (which has a filling factor of $1/2$). In this case, the resulting tensor is also sparse because the overlap between different basis elements is small. This not only enables storing the tensor in memory but also makes the calculation much faster since one can employ algorithms optimized for operations on sparse arrays (see Chapter 18).

As an illustration, consider a system of four qubits so that the Hilbert space has dimension $d = 2^4$. An operator basis for this space has $d^2 = 2^8$ elements and consequently the tensor T_{ijkl} has $(2^8)^4 = 2^{32}$ entries. Using 128 bit complex floats to represent the entries the tensor would take up ≈ 68 GB of memory in a dense format. Conversely, for a GGM basis stored in a sparse data structure, the resulting trace tensor only takes up ≈ 100 MB of memory. Furthermore, calculating T takes ≈ 2.89 s on an Intel® Core™ i9-9900K eight-core processor since a GGM has a low filling factor. By contrast, the same calculation with a Pauli basis takes ≈ 217 s. This is due to the larger filling factor on the one hand and because sparse matrix multiplication algorithms perform poorly with dense matrices on the other.

16.9 Computational complexity

In order to assess the performance of FFs for computing fidelities compared to MC methods, we determine each method's asymptotic scaling behavior as a function of the system dimension d . For the filter functions, we calculate the fidelities using Equations 16.26 and 16.49 in our software implementation, described in more detail in Chapter 18, and hence neglect contributions of $\mathcal{O}(\xi^4)$ from the frequency shifts Δ . Additionally, we distinguish between three different approaches for calculating the control matrix; first, for a single pulse following Equation 16.36, second for an arbitrary sequence of pulses following Equation 16.29, and third for a periodic sequence of pulses following Equation 16.53. For the single pulse, we run benchmarks using exemplary values for the various parameters on a machine with an AMD FX™-6300 processor with six logical cores and 24 GB of memory. We also discuss the filter function method using left-right conjugation by unitaries instead of the Liouville

Table 16.1: Complexity scaling of the three approaches for calculating average gate fidelities discussed in the text. “FF (explicit)” stands for calculating filter functions from scratch following Equation 16.36, “FF (concat.)” for sequences following Equation 16.29, and “FF (periodic)” for periodic Hamiltonians following Equation 16.53. \mathcal{H} and \mathcal{L} designate the vector space on which calculations are performed. Example values for the dominant contributions listed in the table are given for matrix multiplication exponent $b = 2.376$, dimension $d = 2$, number of time steps $n_{\Delta t} = 1000$, and number of gates $G = 100$ (corresponding to a sequence of 100 single-qubit gates with 10 time steps each) with the remaining parameters as in Figure 16.2. For increasing d the computational advantage of FF (\mathcal{L}) over MC diminishes but is conserved for FF (\mathcal{H}).

METHOD	REFERENCE	DOMINATING SCALING	EXAMPLE VALUES
MC (\mathcal{H})	Equation G.7	$n_{\Delta t} n_{\text{MC}} n_{\text{seg}} (d^b + d^3)$	1.3×10^8
FF (\mathcal{L} , explicit)	Equation 16.36	$n_{\Delta t} n_{\omega} n_{\alpha} d^4 + n_{\Delta t} d^{b+2}$	2.4×10^7
FF (\mathcal{H} , explicit)	Equation 16.36	$n_{\Delta t} n_{\omega} n_{\alpha} (d^2 + d^b)$	1.4×10^7
FF (\mathcal{L} , concat.)	Equation 16.29	$G n_{\omega} n_{\alpha} d^4 + G d^{2b}$	2.4×10^6
FF (\mathcal{H} , concat.)	Equation 16.29	$G n_{\omega} n_{\alpha} d^b$	7.8×10^5
FF (\mathcal{L} , periodic)	Equation 16.53	$n_{\omega} (n_{\alpha} d^4 + d^{2b} [1 + \log G])$	1.0×10^5

representation. The latter has higher memory requirements and is expected to perform poorly for large system dimensions d since one deals with $d^2 \times d^2$ transfer matrices on a Liouville space \mathcal{L} instead of $d \times d$ unitaries on a Hilbert space \mathcal{H} . In the software package, the calculations are currently implemented in Liouville space and calculation by conjugation is only partially supported through the low-level API. However, both representations perform similarly for small dimensions as we show below. Note that for a fair performance comparison the different nature of errors needs to be kept in mind. MC becomes less costly if larger statistical errors can be tolerated, whereas the filter-function formalism is typically limited by higher order errors. For reference, the following considerations are summarized in Table 16.1 for each approach and a representative set of parameters.

The MC algorithm is laid out in detail in Appendix G. To calculate the fidelity using MC, we generate n_{MC} different noise traces that slice every time step Δt of the pulse into $n_{\text{seg}} = f_{\text{UV}} \Delta t$ segments to appropriately sample the spectral density with f_{UV} being the ultraviolet cutoff frequency. In total, there are $n_{\Delta t} n_{\text{MC}} n_{\text{seg}}$ noise samples for each of which the Hamiltonian is diagonalized, exponentiated, and the resulting propagators multiplied to get the final, noisy unitary. The entanglement fidelity is then obtained by averaging the trace overlap $d^{-1} \text{tr}(Q^\dagger U)$ of ideal and noisy unitary over all noise realizations. Taking the complexity of matrix diagonalization to be $\mathcal{O}(d^3)$ and matrix multiplication to be $\mathcal{O}(d^b)$ with $b = 3$ for a naive algorithm and $b = 2.376$ for the Coppersmith-Winograd algorithm [202], we expect MC to scale with the dimension d of the problem as $\sim n_{\Delta t} n_{\text{MC}} n_{\text{seg}} (d^b + d^3)$. For simplicity, we use a white noise spectrum for which $S(\omega) = \text{const.}$ but note that sampling arbitrary spectra induces additional overhead for MC, depending on which method is used to generate the noise traces. Typical time-domain methods include the simulation of the underlying physical process (like two-state fluctuators) or the application of an inverse Fourier transform to white noise multiplied by a frequency-domain transfer function.

By contrast, the computational cost of the filter-function formalism as realized by Equation 16.36 is independent of the form of the spectrum. For this approach we find the leading terms to scale as $\sim n_{\Delta t} n_{\omega} n_{\alpha} d^4 + n_{\Delta t} d^{b+2}$ with n_{α} the number of noise operators and n_{ω} the number of frequency samples. Here, the first term is due to the trace in Equation 16.36 which boils down to the trace of a matrix product, $\sum_{ij} A_{ij} B_{ji}$, that scales with d^2 and is performed once for each of the d^2 basis elements, n_{α} noise operators, $n_{\Delta t}$ time steps, and n_{ω} frequency points. The second term is

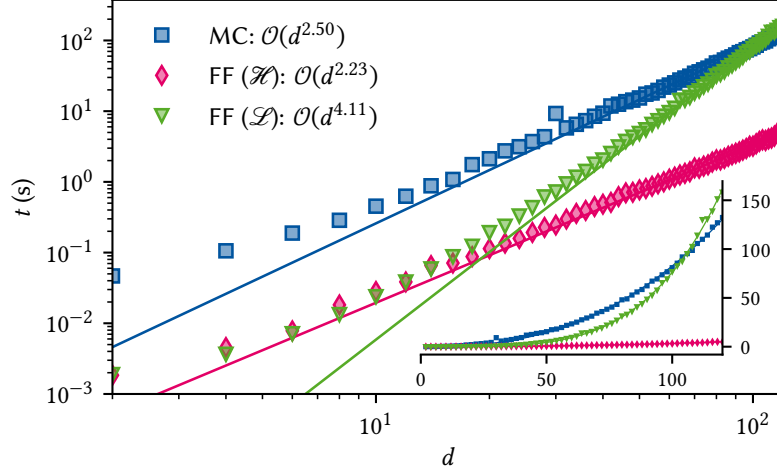


Figure 16.2: Performance of the formalism using Equation 16.36 compared to a Monte Carlo method for a single gate as a function of problem dimension d . Parameters are: $n_{\Delta t} = 1$, $n_{\alpha} = 3$, $n_{\text{MC}} = 100$, $f_{\text{UV}} = 10^2/\Delta t$, $n_{\omega} = 500$ where n_{α} is the number of noise operators considered, n_{MC} the number of Monte Carlo trajectories over which is averaged, and n_{ω} the number of frequency samples. The calculation using filter functions clearly outperforms MC for small system sizes. For dimensions larger than $d \approx 100$ (roughly equivalent to 7 qubits) Monte Carlo (blue squares) performs better than the FF calculation with transfer matrices (green triangles) for this set of parameters and processor due to the better scaling behavior. Using conjugation by unitaries (orange diamonds) significantly outperforms MC also for large dimensions. While the fits to $t = ad^b$ (lines) underestimate the leading order exponent due to the data not being in the asymptotic regime, they support the expected relationship of complexity between the approaches. The inset shows the same data on a linear scale, highlighting the different scaling behaviors for large d .

due to the transformation $C_k \rightarrow \tilde{C}_k^{(g)}$ which requires multiplication of $d \times d$ matrices for every time step and basis element. As $n_{\alpha}n_{\omega} < n_{\text{MC}}n_{\text{seg}}$ for realistic parameters because the ultraviolet cutoff frequency needs to be chosen sufficiently high and the relative error of the method decreases with $1/\sqrt{n_{\text{MC}}}$, we expect that in the case of a single pulse the filter-function formalism in Liouville representation should outperform Monte Carlo calculations for reasonably small dimensions d . Using left-right conjugation, this advantage should hold also for large d . In this case the Hadamard product ($\sim d^2$) as well as matrix multiplication ($\sim d^b$) are carried out for each frequency, noise operator, and time step to calculate the interaction picture noise operators $\tilde{B}_{\alpha}(\omega)$. We thus find this method to scale with $\sim n_{\Delta t}n_{\omega}n_{\alpha}(d^2 + d^b)$.

Figure 16.2 shows exemplary wall times for both methods and $d \in [2, 120]$ that confirm our expectation. Only for about $d \approx 100$ the overhead from the extra time steps and trajectories over which is averaged is compensated for MC. For smaller dimensions the calculation using FFs is faster by almost two orders of magnitude (see the inset showing the same data in a log-log plot). The lines show fits to $t = ad^b$. The data is not quite in the asymptotic regime due to limited memory so that even for large dimension terms of lower power in d contribute significantly to the run time. Even though this causes the fits to underestimate the exponent b , the general trend agrees with our expectation. Note that the crossover does not always occur at the same dimension d . On a different system with an Intel® Core™ i9-9900K eight-core processor the FF method outperformed MC even for $d = 120$ beyond which available memory limited the simulation.

Quantifying the performance gain from using the control matrices' concatenation property to calculate fidelities of gate sequences is more difficult since it strongly depends on the number of gates occurring multiple times in the sequence (enabling reuse of precomputed control matrices) as well as the complexity of the individual gates. The evaluation using

the concatenation rule Equation 16.29 performs asymptotically worse than the evaluation for a complete pulse according to Equation 16.36 because of higher powers of d dominating the calculation in the former case. Performing the G matrix multiplications $\hat{\mathcal{B}}^{(g)}(\omega)Q^{(g-1)}$ from Equation 16.29 is of order $\sim Gn_\omega n_\alpha d^4$, with G the number of pulses in the sequence. Furthermore, calculating the transfer matrix of the total propagators Q_{g-1} involves multiplication of $d \times d$ matrices for all d^4 combinations of basis elements amounting to $\sim Gd^{b+4}$. In case the Liouville representation of the individual pulses' total propagators $P_g, \mathcal{P}^{(g)}$, have been precomputed, the latter computation can be made more efficient since one can just propagate the transfer matrices $\mathcal{P}^{(g)}$ to obtain the cumulative transfer matrices for the sequence, $Q^{(g)} = \prod_{g'=g}^0 Q^{(g')}$, at cost $\sim Gd^{2b}$. The restriction to small dimensions does not apply for conjugation by unitaries as in this case the matrix multiplications involve $d \times d$ matrices and we do not have to compute the Liouville representation. We thus obtain a more favorable asymptotic scaling of $\sim Gn_\omega n_\alpha d^b$.

Utilizing the concatenation property in the Liouville representation thus corresponds to effectively reducing the number of times the calculations scaling with $\sim n_\omega n_\alpha d^4$ have to be carried out but incurs additional calculations scaling with $\sim d^{2b}$. Accordingly, it provides a performance benefit if a sequence consists of either very complex pulses, in which case single repetitions already make the calculation much more efficient, or of few pulses that occur many times. In the extremal case of G repetitions of a single gate the benefit of employing the concatenation property is most pronounced and can be improved even further utilizing the simplifications laid out in Section 16.6. Since matrix inversion has the same complexity as matrix multiplication and taking a matrix to the G th power requires $\mathcal{O}(\log G)$ matrix multiplications, Equation 16.53 should scale with $\sim n_\omega(n_\alpha d^4 + d^{2b} + d^{2b} \log G)$ (the first two terms are due to the final matrix multiplications and are independent of G). It hence allows for a vast speedup over Equation 16.29 in that the asymptotic behavior as a function of the number of gates changes from $\sim G$ to $\sim \log G$. An example of this is presented in Section 19.2 for the context of Rabi driving. Note that this closed form is a unique feature of the transfer matrix representation and not applicable to conjugation by unitaries.

Filter functions from random sampling

17

In our derivation of the average error map $\langle \tilde{\mathcal{U}} \rangle$, Equation 16.9, we employed the cumulant expansion due to Kubo [126, 168]. In his papers, Kubo makes the claim that this expansion is exact for Gaussian noise when truncating after the second order, even for *q-numbers*, i.e., linear operators. For *c-numbers* – scalars – this is a well-known result in statistics; the Gaussian probability distribution is fully described by its first two cumulants, the mean μ and variance σ^2 . However, Fox [127] showed many years later that Kubo’s claim for *q-numbers* does not hold, and that non-commutativity in the Gaussian variables can cause higher-order cumulants to not vanish. There are two limiting cases in which the expansion remains exact; first, for white noise, whose auto-correlation function is singular at $t = 0$, and thus “decouples” higher-order cumulants, and second, commuting noise, for which $[H_c(t), H_n(t)] = 0 \forall t$. Beyond these two cases, we must therefore assume that the map given by Equation 16.9 is merely approximate when including only up to second-order terms from the Magnus expansion.¹ In this chapter, we investigate the extent of this error. To this end, we compute the *exact* filter function (FF) using a Monte Carlo (MC) approach by randomly sampling monochromatic noise fields.

1: Note that the cluster property still holds in all cases, and hence for Gaussian noise only even-order cumulants do not vanish [127, 169, 203, 204].

17.1 Reconstruction by frequency-comb time-domain simulation

For a given interaction-picture quantum operation $\langle \tilde{\mathcal{U}}(\tau) \rangle$ resulting from the quantum system’s evolution under the noise fully characterized by its PSD $S(\omega)$, we *define* the filter function $\mathcal{F}(\omega; \tau)$ by

$$\langle \tilde{\mathcal{U}}(\tau) \rangle = \exp \mathcal{K}(\tau) = \exp \left\{ - \int \frac{d\omega}{2\pi} \mathcal{F}(\omega; \tau) S(\omega) \right\}. \quad (17.1)$$

Now, suppose that

$$S(\omega) = 2\pi\sigma_i^2 \delta(\omega - \omega_i) =: S_i(\omega), \quad (17.2)$$

that is, the PSD of a monochromatic sinusoid of frequency ω_i and root mean square (RMS) σ_i .² Then Equation 17.1 becomes

$$\langle \tilde{\mathcal{U}}_i(\tau) \rangle := \langle \tilde{\mathcal{U}}(\tau) \rangle = \exp \left\{ -2\pi\sigma_i^2 \int \frac{d\omega}{2\pi} \mathcal{F}(\omega; \tau) \delta(\omega - \omega_i) \right\} \quad (17.3)$$

$$= \exp \left\{ -\sigma_i^2 \mathcal{F}(\omega_i; \tau) \right\}, \quad (17.4)$$

where $\langle \tilde{\mathcal{U}}_i(\tau) \rangle$ is the noisy quantum operation generated by monochromatic noise with PSD $S_i(\omega)$ according to Equation 17.2. It is now easy to invert Equation 17.4, and we obtain

$$\mathcal{F}(\omega_i; \tau) = -\sigma_i^{-2} \log \langle \tilde{\mathcal{U}}_i(\tau) \rangle. \quad (17.5)$$

Because we represent quantum operations as matrices in Liouville space, Equation 17.5 is easy to implement on a computer; to sample the exact FF at the set of discrete frequencies $\{\omega_i\}_i$ we simply need to compute $\langle \tilde{\mathcal{U}}_i(\tau) \rangle$

2: Equation 17.2 discretizes $S(\omega)$ by sampling it at points ω_i , i.e.,

$$S(\omega) \sim \lim_{n \rightarrow \infty} \sum_{i=1}^n S_i(\omega).$$

See also Sidenote 15.

using a time-domain simulation method of our choice and take the logarithm!³

Indeed, we can go a step further and split apart the coherent and incoherent contributions to the noisy evolution. Since (in-)coherent quantum operations are represented by (anti-)symmetric matrices in Liouville space, we may define the incoherent and coherent FFs by

$$\begin{aligned}\mathcal{F}_\Gamma(\omega_i; \tau) &= \frac{1}{2} (\mathcal{F}(\omega_i; \tau) + \mathcal{F}(\omega_i; \tau)^\top) \\ &= \frac{1}{2\sigma_i^2} (\log \langle \tilde{\mathcal{U}}_i(\tau) \rangle + \log \langle \tilde{\mathcal{U}}_i(\tau) \rangle^\top),\end{aligned}\quad (17.6)$$

and

$$\begin{aligned}\mathcal{F}_\Delta(\omega_i; \tau) &= \frac{1}{2} (\mathcal{F}(\omega_i; \tau) - \mathcal{F}(\omega_i; \tau)^\top) \\ &= \frac{1}{2\sigma_i^2} (\log \langle \tilde{\mathcal{U}}_i(\tau) \rangle - \log \langle \tilde{\mathcal{U}}_i(\tau) \rangle^\top),\end{aligned}\quad (17.7)$$

respectively. In the filter-function formalism presented in Chapter 16, Equations 17.6 and 17.7 correspond, up to corrections from non-vanishing higher cumulants, to linear combinations of the generalized filter functions from second and first order Magnus expansion, respectively. To be more precise, let us again consider Equation 16.17. Rather than first performing the integrations of Equations 16.20 and 16.21 to obtain the decay amplitudes Γ and frequency shifts Δ and then the contractions with the trace tensor functions g_{ijkl} and f_{ijkl} , first contract the latter with the control matrices to obtain the time-domain filter functions⁴

$$\mathcal{F}_{ij}^{(\Gamma)}(t_1, t_2) = \frac{1}{2} \sum_{kl} g_{ijkl} \tilde{\mathcal{B}}_k(t_1) \tilde{\mathcal{B}}_l(t_2), \quad (17.8)$$

$$\mathcal{F}_{ij}^{(\Delta)}(t_1, t_2) = \frac{1}{2} \sum_{kl} f_{ijkl} \tilde{\mathcal{B}}_k(t_1) \tilde{\mathcal{B}}_l(t_2). \quad (17.9)$$

Again moving to Fourier space and following the same procedure as in Sections 16.2 and 16.3 leads to the coherent and incoherent frequency-domain filter functions $\mathcal{F}_{kl}^{(\Gamma)}(\omega; \tau)$ and $\mathcal{F}_{kl}^{(\Delta)}(\omega; \tau)$ that we must simply integrate over to obtain the average error process $\langle \tilde{\mathcal{U}}(\tau) \rangle$,⁵

$$\langle \tilde{\mathcal{U}}(\tau) \rangle = \exp \left\{ - \int \frac{d\omega}{2\pi} S(\omega) [\mathcal{F}^{(\Gamma)}(\omega; \tau) + \mathcal{F}^{(\Delta)}(\omega; \tau)] \right\}. \quad (17.10)$$

This allows us to analyze in detail deviations of the closed-form expression obtained by means of the cumulant expansion, Equation 17.10, from the exact filter function given by Equation 17.5. In the following, we will lay out explicitly how the latter can be computed in the time domain using a MC method.

To begin with, observe that

$$\langle \tilde{\mathcal{U}}_i(\tau) \rangle = \mathcal{Q}^\top \langle \mathcal{U}_i(\tau) \rangle, \quad (17.11)$$

where as usual \mathcal{Q} is the complete superpropagator of the noise-free time evolution and $\mathcal{U}_i(\tau)$ that of the noisy time evolution generated by a single realization of the noise $b(t)$, both of which are unitary. In MC, we generate N realizations of this noise process in the time domain, compute the full time evolution superpropagator $\mathcal{U}_i(\tau)$, and then evaluate the expectation value $\langle \cdot \rangle$ as the ensemble average to obtain $\langle \mathcal{U}_i(\tau) \rangle$.⁶ Inserting into

3: A similar approach was pursued by Geck in her PhD thesis to compare gate fidelities [205].

4: We consider a single noise operator for simplicity and drop the index for brevity.

5: That is, we have $\mathcal{F}_{ij}^{(\Delta)}(\omega; \tau) = 1/2 \sum_{kl} f_{ijkl} \mathcal{F}_{kl}^{(2)}(\omega; \tau)$ with the latter defined in Equation 16.42 as well as $\mathcal{F}_{ij}^{(\Gamma)}(\omega; \tau) = 1/2 \sum_{kl} g_{ijkl} \mathcal{F}_{kl}(\omega; \tau)$ with the latter defined in Equation 16.25.

6: For N realizations of the stochastic process underlying $b(t)$, the ensemble average of a quantity $A(t)$ that is a function of $b(t)$ is given by

$$\langle A \rangle(t) = \frac{1}{N} \sum_{i=1}^N A_i(t)$$

where i enumerates the realizations of the stochastic process. The relative error of this average scales as $N^{-1/2}$.

Equation 17.4, we find that

$$\mathcal{F}(\omega_i; \tau) = \sigma_i^{-2} \log \langle \tilde{\mathcal{U}}_i(\tau) \rangle = \sigma_i^{-2} \log \mathcal{Q}^\top \langle \mathcal{U}_i(\tau) \rangle. \quad (17.12)$$

If we evaluate Equation 17.12 for a set of frequencies $\{\omega_i\}_i$ sampling the true spectrum $S(\omega)$ sufficiently well, we thus obtain the exact filter function $\mathcal{F}(\omega; \tau)$ (within the accuracy of MC), allowing us to compare the accuracy of the formalism developed in Chapter 16.

So what does a single noise realization of Equation 17.2 in the time domain look like? It is a sinusoid with amplitude $A_i \sim \text{Rayleigh}(\sigma_i)$,⁷ frequency ω_i , and phase $\phi \sim \text{Unif}(0, 2\pi)$,⁸

$$b(t) = A_i \sin(\omega_i t + \phi). \quad (17.13)$$

To obtain the MC estimate of $\langle \tilde{\mathcal{U}}(\tau) \rangle$, we therefore draw N noise traces according to Equation 17.13, solve the Schrödinger equation, and finally perform the ensemble average from which we can deduce the filter function using Equation 17.12. From the spread of the individual MC samples we obtain confidence intervals on the mean of the error transfer matrix by bootstrapping, which we propagate to the filter function by taking the Fréchet derivative of the matrix logarithm in Equation 17.12 [207]. For details on the MC procedure, refer to Appendix G.

7: $\text{Rayleigh}(\sigma)$ is the Rayleigh distribution with probability density function [206]

$$\rho(x) = \frac{x}{\sigma^2} \exp\left\{-\frac{x^2}{2\sigma^2}\right\}.$$

It describes the probability distribution of the distance from the origin of a point drawn from a bivariate normal distribution with mean 0 and standard deviation σ .

8: The probability density function of the uniform distribution $\text{Unif}(a, b)$ is

$$\rho(y) = \begin{cases} (b-a)^{-1} & \text{if } a \leq y < b, \\ 0 & \text{else} \end{cases}$$

17.2 Case studies

Let us now turn to applying the method to a few select case studies. First, we consider a pure-dephasing Hamiltonian with

$$\begin{aligned} H_c(t) &= \Omega \frac{\sigma_z}{2}, \\ H_n(t) &= b(t) \frac{\sigma_z}{2}. \end{aligned} \quad (17.14)$$

Specifically, we let the system evolve under the Hamiltonian in Equation 17.14 for $\tau = \pi/\Omega$ to undergo a π -rotation around the z -axis of the Bloch sphere. For this model, we expect the cumulant expansion to terminate after the second order because control and noise commute, and hence the interaction-picture noise Hamiltonian, $\tilde{H}_n(t)$, always commutes with itself, and therefore the filter-function formalism of Chap-

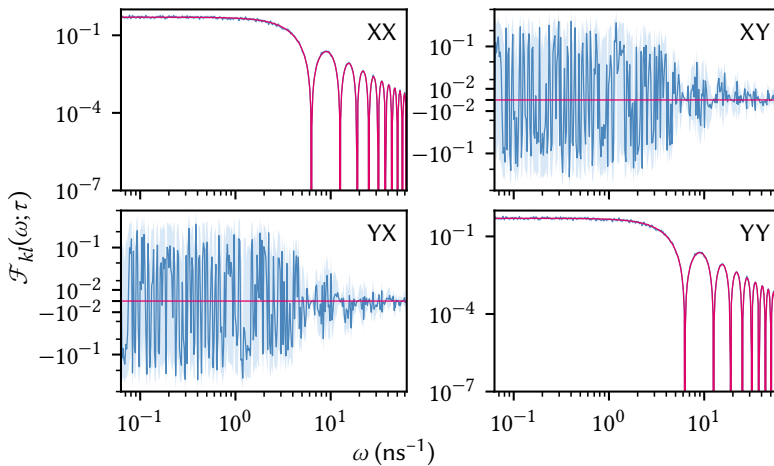


Figure 17.1: Non-zero components of the FF in the Pauli basis \mathbf{P}_1 for the pure dephasing Hamiltonian in Equation 17.14. Magenta lines are from the cumulant expansion, Equation 17.10, blue lines the mean of the MC simulation, Equation 17.12, and light blue shaded areas the 95 % confidence interval. The diagonal elements (XX and YY) agree within the MC confidence intervals, with the zeros at $2\pi n/\tau, n \in \{1, 2, \dots\}$ agreeing down to 10^{-15} where we can expect numerical errors to be limiting. The off-diagonal elements are quite noisy in the MC simulation, but fluctuate about the expected value of zero.

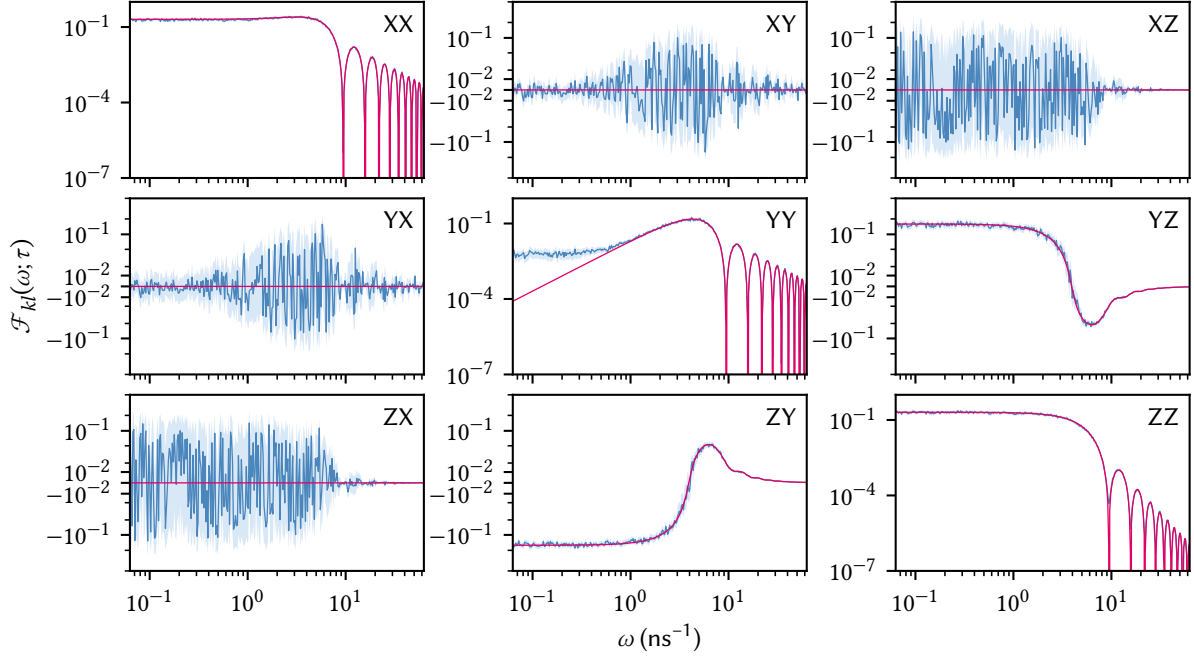


Figure 17.2: FFs for the non-commuting Hamiltonian in Equation 17.15. Cumulant expansion calculation is shown in magenta, MC in blue with light blue shaded areas the confidence intervals. Again, the nominally-zero off-diagonals are susceptible to numerical noise in the MC method. The YY- and ZZ-terms show a deviation of the cumulant expansion calculation, while all others, including the coherent YZ- and ZY-terms appear to be exact up to the numerical uncertainty.

ter 16 should give the exact result. Equation 17.14 can be solved analytically, and gives rise to an ideal dephasing channel whose PTM representation is diagonal, $\langle \tilde{U}(\tau) \rangle = \text{diag}(1, 1 - p, 1 - p, 1)$ with p the dephasing probability whose precise value depends on the form of the PSD $S(\omega)$. Accordingly, the FF $\mathcal{F}_{kl}(\omega; \tau)$ should be zero everywhere but at $k = l \in \{1, 2\} \equiv \{x, y\}$ for the Pauli basis P_1 . Figure 17.1 shows the total “error transfer matrix filter functions” (Equations 17.10 and 17.12) computed with both methods, magenta for the cumulant expansion and blue for the exact MC method. The diagonals agree perfectly within the confidence intervals, while the off-diagonals are dominated by numerical noise in the MC approach. Since the off-diagonals are zero, only the first-order Magnus terms contribute.⁹

The opposite extreme to the pure-dephasing Hamiltonian is obtained when changing the control to be transverse to the noise,

$$\begin{aligned} H_c(t) &= \Omega \frac{\sigma_x}{2}, \\ H_n(t) &= b(t) \frac{\sigma_z}{2}. \end{aligned} \quad (17.15)$$

In this case, control and noise Hamiltonian maximally do not commute at any time ($\tilde{H}_n(t) = \sigma_z \cos \Omega t + i\sigma_y \sin \Omega t$) and we should expect the largest deviations from the exact filter functions in the approximation by truncating the cumulant function after the second order. Figure 17.2 shows the FF for a π -rotation around the x -axis of the Bloch sphere (*i.e.*, $\tau = \pi/\Omega$ once again). This time, all diagonal elements are nonzero, and the YY-term ($\mathcal{F}_{22}(\omega; \tau)$ with $\sigma_2 \equiv \sigma_y$) displays a deviation between cumulant expansion and MC simulation towards low frequencies! This is exactly what we would expect according to Fox [127], namely that the “less white” the noise is, the larger contributions from higher orders will be. Also deviating is the ZZ-term, although not towards DC but where the filter

9: Recall that $\mathcal{F}^{(\Delta)}(\omega; \tau)$ is anti-symmetric.

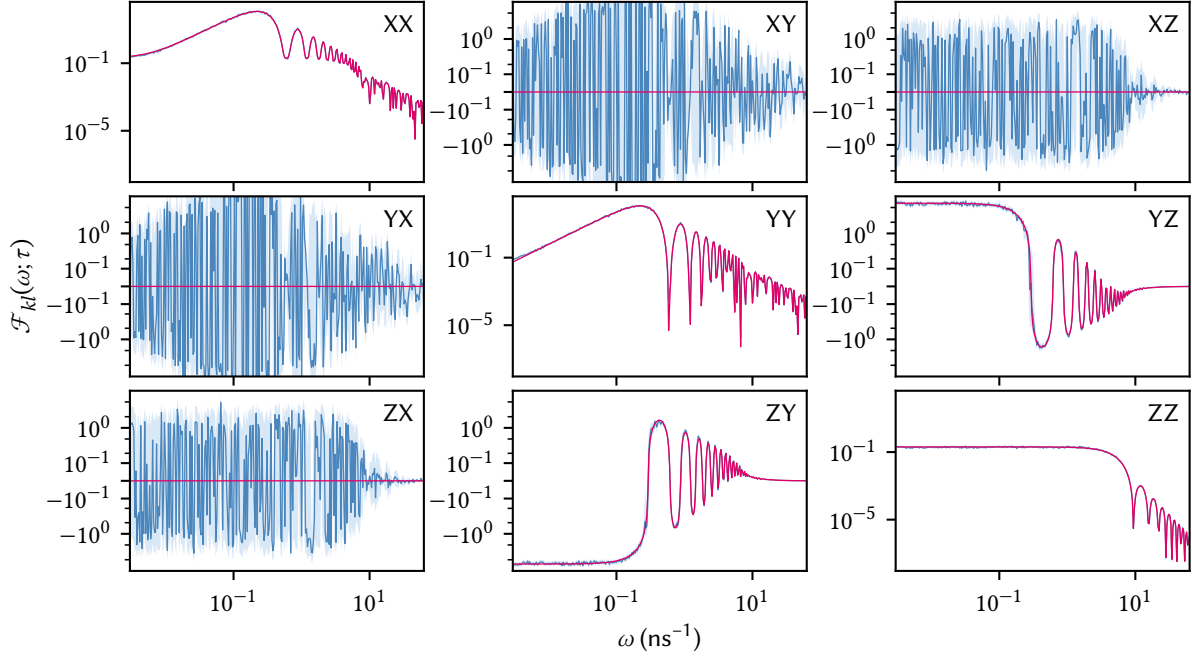


Figure 17.3: FFs for the spin echo (SE) Hamiltonian in Equation 17.16. Cumulant expansion calculation is shown in magenta, MC in blue with light blue shaded areas the confidence intervals. Both coherent and incoherent terms show excellent agreement between both methods.

function computed from the approximated cumulant function drops to zero. By contrast, the XX-term shows good agreement between both methods. Finally, two non-diagonal elements are nonzero, YZ and ZY, anti-symmetric terms which arise from the second-order Magnus and incur coherent errors. For these, the cumulant approximation is excellent, showing no deviation within the confidence intervals.

Finally, as a last example we consider the prototypical filter-function use case: the SE. Here, the qubit idles for a time τ_0 before and after a π rotation around the x -axis of the Bloch sphere, so that the Hamiltonian is given by

$$\begin{aligned} H_c(t) &= \Omega(t) \frac{\sigma_x}{2}, \\ H_n(t) &= b(t) \frac{\sigma_z}{2}, \end{aligned} \quad (17.16)$$

with $\Omega(t) = \pi/\tau_\pi$ if $t \in [\tau_0, \tau_0 + \tau_\pi]$ and zero else. This pulse sequence is known to cancel quasistatic dephasing noise as the phase picked up on the equator of the Bloch sphere during the first period of free evolution is exactly cancelled by the phase picked up during the second period after the π -pulse. Since the previous example demonstrated that the filter-function formalism based on the second-order cumulant expansion neglects contributions from higher orders in the case of transverse noise, we might expect the SE sequence to show similar behavior. Figure 17.3 shows the results of the simulation. The picture is similar – albeit more complex – to before, with nominally-zero terms suffering from numerical noise. However, in contrast to the simple π -pulse Hamiltonian in Equation 17.15, the YY and ZZ terms show excellent agreement between the exact MC method and the cumulant expansion. We may speculate that the higher-order contributions not captured by the cumulant method in the previous case drop out due to the symmetry of the Hamiltonian.

In conclusion,

The `filter_functions` software package

18

In this section we give a brief overview over the `filter_functions` software package implementing the main features of the formalism derived above.¹ This includes the calculation of the decay amplitudes Γ , frequency shifts Δ , and fidelities as well as the calculation of the control matrices for single gates and both generic and periodic sequences of gates. Moreover, control matrices may be efficiently extended to and merged on larger Hilbert spaces. Calculations using unitary conjugation instead of transfer matrices are implemented but at this point not available in the high-level API.

1: For more details we refer the reader to the [documentation](#).

Our software is written in Python and published under the GPLv3 license [170]. It features a broad coverage through unit tests and extensive API documentation as well as didactic examples (see also Chapter 19). The package relies on the NumPy [208] and SciPy [209] libraries for vectorized array operations. Data visualization is handled by matplotlib [210]. For tensor multiplications with optimized contraction order we use `opt_einsum` [211] for which `sparse` [212], a library aiming to extend the SciPy sparse module to multi-dimensional arrays, serves as a backend in the calculation of the trace tensor from Equation 16.18. Lastly, the package is written to interface with `qopt` [172] and `QuTiP` [171], frameworks for the simulation and optimization of open quantum systems, and mirrors the latter's data structure for Hamiltonians ensuring easy interoperability between the two.

18.1 Package overview

In the `filter_functions` package all operations are understood as sequences of pulses that are applied to a quantum system. These pulses are represented by instances of the `PulseSequence` class which holds information about the physical system (control and noise Hamiltonians) as well as the mathematical description (*e.g.* the basis used for the Liouville representation). As indicated above, the Hamiltonians $H_c(t)$ and $H_n(t)$ are given in a similar structure as in `QuTiP`. That is, a Hamiltonian is expressed as a sum of Hermitian operators with the time dependence encoded in piecewise constant coefficients so that

$$H_c(t) = \sum_i a_i^{(g)} A_i = \text{const.} \quad (18.1a)$$

$$H_n(t) = \sum_\alpha s_\alpha^{(g)} B_\alpha = \text{const.} \quad (18.1b)$$

for $t \in (t_{g-1}, t_g]$, $g \in \{1, \dots, G\}$ and where the $a_i^{(g)}$ are the amplitudes of the i th control field. Note that the noise variables $b_\alpha(t)$ are missing from Equation 18.1b because they are captured by the spectral density $S(\omega)$. In the software, Equations 18.1a and 18.1b are represented as lists whose i th element corresponds to a sublist of two elements: the i th operator and the i th coefficients $[a_i^{(0)}, \dots, a_i^{(G)}]$.

The `PulseSequence` class provides methods to calculate and cache the filter function according to Equation 16.30. Alternatively, filter functions

may also be cached manually to permit using the package with analytical solutions for the control matrix. Concatenation of pulses is implemented by the functions `concatenate()` and `concatenate_periodic()` which will attempt to use the cached attributes of the `PulseSequence` instances representing the pulses to efficiently calculate the filter function of the composite pulse following Equation 16.29 and Equation 16.53, respectively.

Operator bases fulfilling Equation 16.14 are implemented by the `Basis` class. There are two predefined types of bases:

1. Pauli bases P_n for $n = 2^d$ qubits from Equation 16.54 and
2. GGM bases Λ_d of arbitrary dimension d from Equation 16.55.

The Pauli basis is both unitary and separable while the GGM basis is sparse for large dimensions but neither unitary nor separable. As mentioned in Section 16.7 (see also Section 19.4), using a separable basis can provide significant performance benefits for calculating the filter functions of algorithms. On the other hand, a sparse basis makes the calculation of the trace tensor T_{ijkl} and therefore also of the error transfer matrix $\tilde{\mathcal{U}}$ much faster (*cf.* Section 16.8). Additionally, the user can define custom bases using the class constructor.

The error transfer matrix $\tilde{\mathcal{U}}$ can be calculated for a given pulse and noise spectrum using the `error_transfer_matrix()` function. Various other quantities can be computed from $\tilde{\mathcal{U}}$ as outlined in Section 16.4. Furthermore, the package includes a plotting module that offers several functions, *e.g.* for the visualization of filter functions or the evolution of the Bloch vector using `QuTiP`.

18.2 Workflow

We now give a short introduction into the workflow of the `filter_` functions package by showing how to calculate the dephasing filter function of a simple Hahn SE sequence [213] as an example. The sequence consists of a single π -pulse of finite duration around the x -axis of the Bloch sphere in between two periods of free evolution. We can hence divide the control fields into three constant segments and write the control Hamiltonian as

$$H_c^{(\text{SE})}(t) = \frac{\sigma_x}{2} \times \begin{cases} \pi/t_\pi, & \text{if } \tau \leq t < \tau + t_\pi \\ 0, & \text{otherwise} \end{cases} \quad (18.2)$$

with τ the duration of the free evolution period and t_π that of the π pulse. For the noise Hamiltonian we only need to define the deterministic time dependence $s_\alpha(t)$ and operators B_α since the noise strength is captured by the spectrum $S(\omega)$. Thus we have $s_z(t) = 1$ and $B_z = \sigma_z/2$ for pure dephasing noise that couples linearly to the system.

In the software, we first define a `PulseSequence` object representing the SE sequence. As was already mentioned, the control and noise Hamiltonians are given as a list containing lists for every control or noise operator that is considered. These sublists consist of the respective operator as a NumPy array or `QuTiP` `Qobj` and the amplitudes ($a_i^{(g)}$ or $s_\alpha^{(g)}$) in an iterable data structure such as a list. We can hence instantiate the `PulseSequence` with the following code:

```

import filter_functions as ff
import qutip as qt
from math import pi
tau, t_pi = (1, 1e-3)
# Control Hamiltonian for pi rotation in 2nd time step
H_c = [[qt.sigmax()/2, [0, pi/t_pi, 0]]]
# Pure dephasing noise Hamiltonian with linear coupling
H_n = [[qt.sigmaz()/2, [1, 1, 1]]]
# Durations of piecewise constant segments
dt = [tau, t_pi, tau]
ECHO = ff.PulseSequence(H_c, H_n, dt)

```

where a basis is automatically chosen since we did not specify it in the constructor in the last line. Calculating the filter function of the pulse for a given frequency vector ω can then be achieved by calling

```
F = ECHO.get_filter_function(omega)
```

where F is the dephasing filter function $\mathcal{F}_{zz}(\omega)$ as we only defined a single noise operator. Finally, we calculate the error transfer matrix \tilde{U} for the noise spectral density $S_{zz}(\omega) = \omega^{-2}$,

```

S = 1/omega**2
U = ff.error_transfer_matrix(ECHO, S, omega)

```

This code uses the control matrix previously cached when the filter function was first computed. Therefore, only the integration in Equation 16.24 and the calculation of the trace tensor in Equation 16.18 are carried out in the last line.

An alternative approach to calculate the spin echo filter function is to employ the concatenation property. For this, we interpret the SE as a sequence consisting of three separate pulses. Each of the pulses has a single time segment during which a constant control is applied and concatenating the separate `PulseSequence` instances yields the `PulseSequence` representing a spin echo. This way analytical control matrices may be used to calculate the control matrix of the composite sequence. Pulses can be concatenated by using either the `concatenate()` function or the overloaded `@` operator:

```

# Define PulseSequence objects as shown above
FID = ff.PulseSequence(...)
NOT = ff.PulseSequence(...)
# Cache the analytical control matrices at frequency omega
FID.cache_control_matrix(omega, B_FID)
NOT.cache_control_matrix(omega, B_NOT)
# Concatenate the pulses
ECHO = FID @ NOT @ FID

```

Since we have cached the control matrices of the FID and NOT pulses, that of the ECHO object is also automatically calculated and stored. Concatenating `PulseSequence` objects is implemented as an arithmetic operator of the class to reflect the intrinsic composition property of the control matrices.

Further development of the software has focused on making it available in a gate optimization and simulation framework [214]. Besides using it to compute decoherence effects and fidelities, analytical derivatives of the filter functions have been implemented to allow for optimizing pulse parameters in the presence of non-Markovian noise within the framework of quantum optimal control [172, 215].

Additionally, building an interface with `qupulse` [216, 217], a software toolkit for parametrizing and sequencing control pulses and relaying

them to control hardware, would implement the capability to compute filter functions of pulses assembled in `qupulse`, thereby allowing a user in the lab to easily inspect the noise susceptibility characteristics of the pulse they are currently applying to their device.

Example applications

We now present example applications of the software package and the formalism. As stated before, we focus on the decay amplitudes Γ and its associated filter functions and assume that the unitary errors generated by the frequency shifts Δ are either small (as is the case for gate fidelities) or calibrated out. All of the examples shown below are part of the software documentation as either interactive Jupyter notebooks [218] or Python scripts. In the following, we give angular frequencies and energies in units of inverse times (e.g. s^{-1}) while ordinary frequencies are given in Hz and we write $\langle \tilde{\mathcal{U}}(\tau) \rangle = \mathcal{U}$ for legibility.

19.1 Singlet-triplet two-qubit gates

In order to benchmark fidelity predictions of our implementation as well as demonstrate its application to nontrivial pulses, we compute the first-order infidelity of the two-qubit gates presented in Reference 219 and compare the results to the reference's Monte Carlo calculations. There, a numerically optimized gate set consisting of $\{X_{\pi/2} \otimes I, Y_{\pi/2} \otimes I, \text{CNOT}\}$ for exchange-coupled singlet-triplet spin qubits is introduced, taking into account different noise spectra and realistic control hardware.

For readers unfamiliar with the reference we briefly summarize the physical system and noise model entering the optimization. The authors consider four electrons confined in a linear array of four quantum dots in a semiconductor heterostructure. Each electron $i \in \{1, 2, 3, 4\}$ experiences a different static magnetic field B_i so that there is a gradient $b_{ij} = B_i - B_j$ between two adjacent dots i and j . This gives rise to spin quantization along the magnetic field axis and defines the eigenstates $\{|\uparrow\downarrow\rangle, |\downarrow\uparrow\rangle\}$ that span the computational subspace of a single qubit so that the accessible Hilbert space of the two-qubit system is spanned by $\{|\uparrow\downarrow\rangle, |\downarrow\uparrow\rangle\}^{\otimes 2}$. The magnitude of the exchange interaction J_{ij} between two adjacent dots i and j is controlled via gate electrodes located on top of the heterostructure that can be pulsed on a nanosecond timescale with an arbitrary waveform generator (AWG). Changing the gate voltages changes the detuning ϵ_{ij} of the electrochemical potential between dots and in turn leads to a change in exchange coupling according to the phenomenological model $J_{ij}(\epsilon_{ij}) \propto \exp(\epsilon_{ij})$.

The pulses are defined by a set of discrete detuning voltages ϵ_{ij} passed to an AWG with a sample rate of 1 GS/s and constant magnetic field gradients b_{ij} are assumed. To reflect the fact that the qubits experience a different pulse than what is programmed into the AWG due to cable dispersion and non-ideal control hardware, the detunings are convoluted with an experimental impulse response [219]. Finally, the signal is discretized as piecewise constant by slicing each segment into five steps, yielding a time increment of $\Delta t = 0.2 \text{ ns}$.

To find optimal detuning pulses, a Levenberg-Marquardt algorithm iteratively minimizes the infidelity, leakage, and trace distance from the target unitary. For the infidelity, contributions from quasistatic magnetic field noise as well as quasistatic and white charge noise are taken into account during each iteration. Because treating colored (correlated) noise using

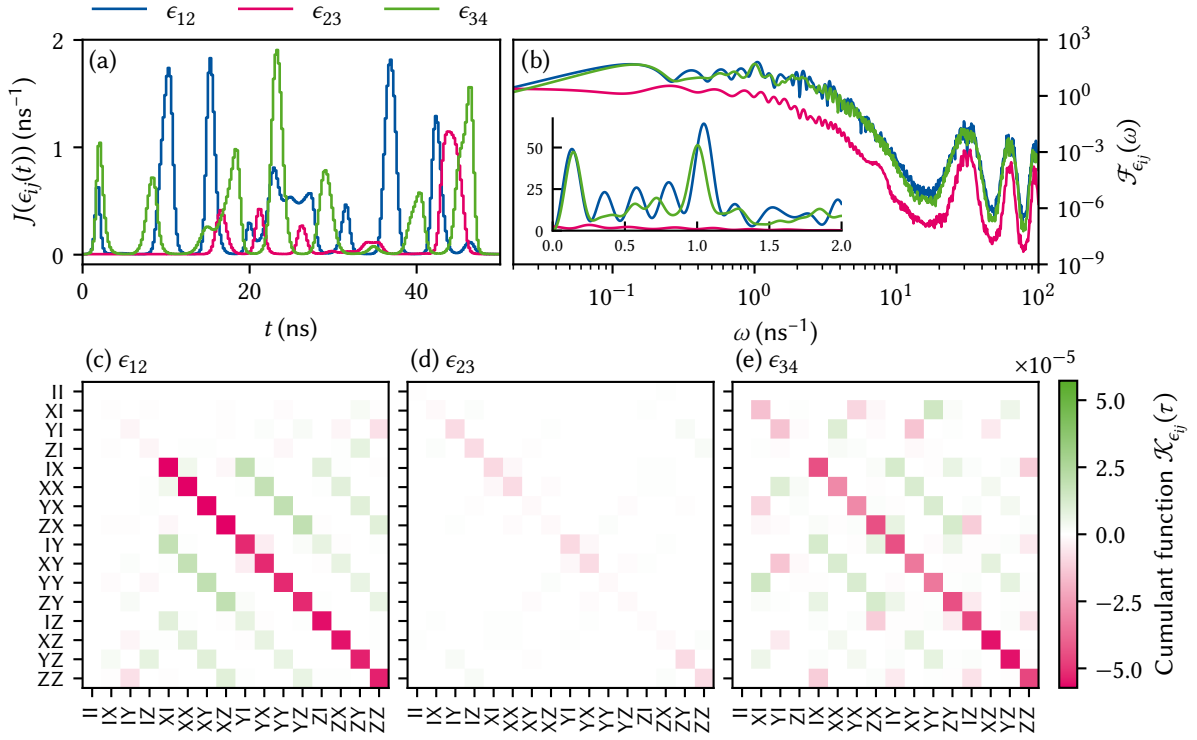


Figure 19.1: (a) Exchange interaction $J(\epsilon_{ij})$ for the CNOT gate presented in Reference 219 as function of time. (b) Filter functions $\mathcal{F}_{\epsilon_{ij}}$ for noise in the detunings evaluated on the computational subspace. The filter functions are modulated by oscillations at high frequencies due to numerical artifacts of the finite step size for the time evolution. The inset shows the filter functions in the DC regime on a linear scale with distinct peaks around $\omega = 2\pi/\tau$ and $\omega = 50/\tau$ ($\tau = 50$ ns). (c)–(e) Computational subspace block of the first order approximation of the error transfer matrix, given by the cumulant function \mathcal{K}_{aa} excluding second order contributions, for the CNOT gate and the three detunings $\alpha \in \{\epsilon_{12}, \epsilon_{23}, \epsilon_{34}\}$. Note that in panel (e) the order of the rows and columns was permuted for better comparability.

Monte Carlo methods is computationally expensive (*cf.* Section 16.9), the infidelity due to fast $1/f$ -like noise is only computed for the final gate and not used during the optimization.

Two-qubit interactions are mediated via the exchange J_{23} that makes the states $|\uparrow\uparrow\downarrow\downarrow\rangle$ and $|\downarrow\downarrow\uparrow\uparrow\rangle$ accessible. They constitute levels outside of the computational subspace that ideally should only be occupied during an entangling gate operation. A non-vanishing population of these states after the operation has ended is therefore unwanted and considered leakage, the magnitude of which we could quantify following Subsection 16.4.3. However, here we limit ourselves to determine the infidelity contribution from fast, *viz.* non-quasistatic, charge noise entering the system through ϵ_{ij} . That is, we consider noise sources $\alpha \in \{\epsilon_{12}, \epsilon_{23}, \epsilon_{34}\}$. We take the non-linear dependence of the Hamiltonian on the detunings ϵ_{ij} into account by setting $s_{\epsilon_{ij}}(t) = \partial J_{ij}(\epsilon_{ij}(t)) / \partial \epsilon_{ij}(t) \propto J_{ij}(\epsilon_{ij}(t))$.

Figure 19.1 shows the filtered (convoluted) exchange interaction J_{ij} between each pair of dots during the pulse sequence in panel (a) and filter functions plotted as function of frequency in panel (b) for the three different detunings. For a detailed description on how the filter functions were computed in the presence of additional leakage levels refer to Section E.2. As one would expect from the fact that the intermediate (inter-qubit) exchange interaction J_{23} (orange dash-dotted lines) is only turned on for short times to entangle the qubits, the filter function for ϵ_{23} is smaller by roughly an order of magnitude than the intra-qubit exchange filter functions. Notably, the filter functions for ϵ_{12} and ϵ_{34} show clear charac-

a	THIS WORK		REFERENCE 219	
	0	0.7	0	0.7
$X_{\pi/2} \otimes I$	1.7×10^{-3}	5.8×10^{-5}	1.9×10^{-3}	5.7×10^{-5}
$Y_{\pi/2} \otimes I$	1.6×10^{-3}	5.7×10^{-5}	1.7×10^{-3}	5.6×10^{-5}
CNOT	1.4×10^{-3}	6.3×10^{-5}	1.6×10^{-3}	6.3×10^{-5}

Table 19.1: Fast charge noise infidelity contributions to the total average gate fidelity of the two-qubit gate set from Reference 219 without capacitive coupling for GaAs S-T₀ qubits compared to the original results. The fidelities are consistent with results from the reference within the uncertainty bounds of 3% of the Monte Carlo calculation. The infidelities presented here are all average gate infidelities (cf. Equation 16.44, References 193 and 194).

teristics of DCGs, that is they drop to zero as $\omega \rightarrow 0$, and decouple from quasistatic noise with an error suppression $\propto \omega^2$. This is not unexpected as the optimization minimizes quasistatic noise contributions to the infidelity. In addition, one can also observe small oscillations with period 5 ns^{-1} in frequency space that arise as a numerical artifact of the piecewise constant discretization of the control parameters as investigations have shown. If high-frequency spectral components are expected to play a significant role, one needs to be aware of these effects and adjust the simulation parameters appropriately.

The inset of Figure 19.1(b) shows the same filter functions for the DC tail on a linear scale. Most notably, $\mathcal{F}_{\epsilon_{12}}$ and $\mathcal{F}_{\epsilon_{34}}$ have maxima around $\omega = 2\pi/\tau$, *i.e.* exactly the frequency matching the pulse duration, and around $\omega = 50/\tau = 1 \text{ ns}^{-1}$ with $\tau_{\text{CNOT}} = 50 \text{ ns}$. The former is the typical window in which a pulse is most susceptible to noise whereas the latter matches the absolute value of the magnetic field gradients, $b_{12} = -b_{34} = 1 \text{ ns}^{-1}$, indicating that the peak corresponds to the qubit dynamics generated by the magnetic field gradients. Panels (c)–(e) show the cumulant functions $\mathcal{K}_{\epsilon_{ij}}(\tau)$ of the detuning error channels ϵ_{ij} on the computational subspace. $\mathcal{K}_{\epsilon_{12}}$ displays clear characteristics of a Pauli channel with only elements on the diagonal and secondary diagonals deviating from zero significantly whereas $\mathcal{K}_{\epsilon_{34}}$ (the target qubit) possesses a more complicated structure.

We now compute the infidelity contribution originating from fast charge noise using Equation 16.44 but tracing only over the computational subspace to compare to the Monte Carlo calculations of Reference 219 (see Section E.2 for further details). Like the reference, we use a noise spectrum $S_{\epsilon,a}(f) \propto 1/f^a$ with $S_{\epsilon,a}(1 \text{ MHz}) = 4 \times 10^{-20} \text{ V}^2/\text{Hz}$ and consider white noise ($a = 0$) and correlated noise with $a = 0.7$ [141] with infrared and ultraviolet cutoffs $1/\tau$ and 100 ns^{-1} , respectively. Table 19.1 compares the results in this work with the reference. The values computed here are consistent with the more elaborate Monte Carlo calculations within a few percent. Notably, the deviation is smaller for the smaller noise levels with $a = 0.7$, in line with the fact that we have only computed the contributions from the decay amplitudes Γ and thus the leading order perturbation. If we had additionally evaluated the frequency shifts Δ we could have obtained the exact fidelity in the case of Gaussian noise.

19.2 Rabi driving

A widely used method for qubit control is Rabi driving [139, 144, 156, 220]. If we restrict ourselves to the resonant case for simplicity, the control Hamiltonian takes on the general form $H_{\text{C}} = \omega_0 \sigma_z/2 + A \sin(\omega_0 t + \phi) \sigma_x$.

Here, ω_0 is the resonance frequency, A the drive amplitude corresponding to the Rabi frequency in the weak driving limit $A/\omega_0 \ll 1$, $\Omega_R \approx A$, and ϕ an adjustable phase giving control over the rotation axis in the xy -plane of the Bloch sphere. This Hamiltonian and associated decoherence mechanisms are well-studied in the weak driving regime, where the rotating-wave approximation (RWA) can be applied to remove fast-oscillating terms in the rotating frame [221, 222]. There is a comprehensive understanding of how spectral densities transform to this frame and which frequencies are most relevant to loss of coherence [223].

By contrast, the description of a system in the strong driving regime, where $A/\omega_0 \sim 1$, is more complicated since the RWA cannot be applied without making large errors. Yet, an improved understanding is desirable because strong driving allows for much shorter gate times and thus shifts the window of relevant noise frequencies towards higher energies where the total noise power is typically lower, *e.g.* for $1/f$ noise. Conversely, faster control also requires more accurate timing to prevent rotation errors. It is therefore of interest to have tools that can provide a comprehensive picture for Rabi pulses over a wide range of driving amplitudes. By making use of the concatenation property of the filter functions, our formalism can do just that.

The problem that arises when trying to numerically investigate Rabi pulses in the weak driving regime in the lab frame is that typical control operations have a duration $\tau \gg T$ with $T = 2\pi/\omega_0$. Since the sampling time step Δt should additionally be chosen much smaller than a single drive period in order to sample the time evolution accurately ($\Delta t \ll T$), brute-force simulations are costly.

For $T/\Delta t = 100$ samples per period and assuming Rabi and drive frequencies in typical regimes for SiGe and metal-oxide-semiconductor (MOS) quantum dots [224, 225] or trapped ions [156], $\Omega_R = 1 \mu\text{s}^{-1}$ and $\omega_0 = 20 \text{ ns}^{-1}$, a Monte Carlo simulation of a π -rotation with approximately 3% relative error would require 10^9 samples in total. Using the filter-function formalism, we can drastically reduce the simulation time even beyond the improvement gained from concatenating precomputed filter functions of individual drive periods using Equation 16.29. This can be achieved with Equation 16.53, which simplifies the calculation of the control matrix for periodic Hamiltonians.

To benchmark our implementation, we use the parameters from above and calculate the control matrix of a NOT gate generated by a Rabi Hamiltonian with three different methods on an Intel® Core™ i9-9900K eight-core processor. First, we use Equation 16.29 in a brute force approach. Second, we utilize the concatenation property following Equation 16.36. Third, we employ the simplified expression given by Equation 16.53. The brute force approach takes 250 s of wall time whereas calculating the filter function using the standard concatenation is faster by two orders of magnitude, taking 1.5 s to run. Lastly, the calculation utilizing the optimized method is faster again by two orders of magnitude and is completed in 0.056 s.

As an example application, we calculate the filter functions for continuous Rabi driving in the weak and strong driving regimes. For weak driving, we use the parameters from the benchmark above for a pulse of duration $\tau_{\text{weak}} \approx 20 \mu\text{s}$ that corresponds to 20 identity rotations in total. For the strong driving regime, we use the approximate analytical solution for a flux qubit biased at its symmetry point from Reference 226 with $A = \omega_0/4$ to drive the qubit for $\tau_{\text{strong}} \approx 4 \text{ ns}$ so that we achieve the same amount of identity rotations as in the weak driving case. In

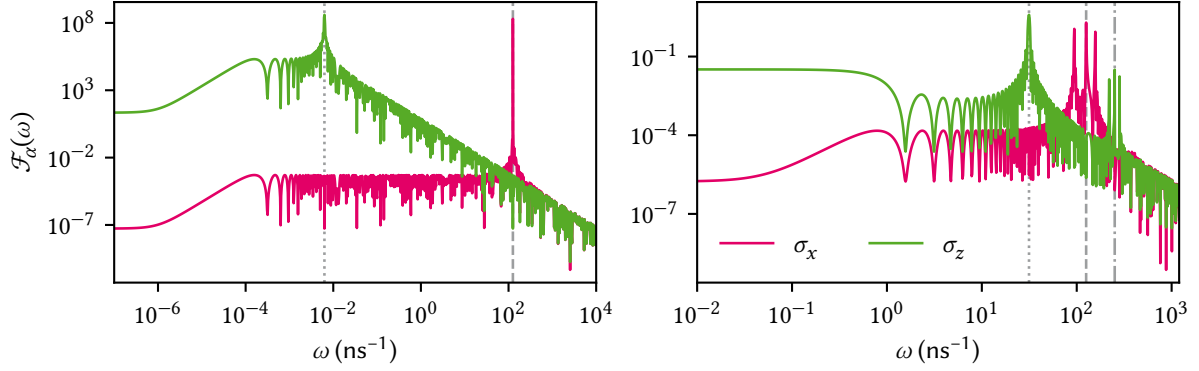


Figure 19.2: Filter functions for weak (a) and strong (b) Rabi driving (20 identity gates in total). gray dashed (dotted) lines indicate the respective drive (Rabi) frequencies ω_0 (Ω_R). (a) Weak driving with $A/\omega_0 \ll 1$. The filter function \mathcal{F}_x for noise operator σ_x is approximately constant up to the resonance frequency where it peaks sharply and then aligns with the filter function \mathcal{F}_z for σ_z . \mathcal{F}_z peaks at the Rabi frequency before rolling off with ω^{-2} and a DC level that is almost ten orders of magnitude larger than the DC level of the transverse filter function \mathcal{F}_x . (b) Strong driving with $A/\omega_0 \sim 1$. Again \mathcal{F}_z peaks at Ω_R whereas \mathcal{F}_x has three distinct peaks at ω_0 and $\omega_0 \pm \Omega_R$. These features also appear at $2\omega_0$ in \mathcal{F}_z due to the strong coupling (dash-dotted line).

the reference, strong driving in this regime is shown to give rise to non-negligible counterrotating terms that modulate the Rabi oscillations and which are well-described by Floquet theory applied to the Rabi driving Hamiltonian. While for the regime studied here only two additional modes appear, the results extend to the regime where $A > \omega_0$ and up to eight different frequency components were observed.

Figure 19.2 shows the filter functions \mathcal{F}_x and \mathcal{F}_z for the σ_x and σ_z noise operators in the weak (a) and the strong (b) driving regime. Both display sharp peaks at their Rabi frequencies and the resonance frequency for \mathcal{F}_z and \mathcal{F}_x , respectively. We expect these features as they correspond to perturbations of the qubit Hamiltonian that are resonant with the qubit dynamics about an axis orthogonal to them. For weak driving, \mathcal{F}_x is constant up to the resonance frequency where it peaks sharply and then aligns with \mathcal{F}_z . The latter has a peak at the Rabi frequency before rolling off with ω^{-2} and a DC level that is almost ten orders of magnitude larger than that of the transverse filter function. This behavior is consistent with the results by Yan et al. [223], who show that the noise sources dominating decoherence during driven evolution are $S_x(\omega_0)$ and $S_z(\Omega_R)$. Note that the piecewise-constant control approximation causes the weak driving filter functions to level off towards low frequencies after an initial roll-off (here at $\omega \sim 1 \text{ ms}^{-1}$). By decreasing the discretization time step Δt , one can shift the frequency at which this effect occurs to lower frequencies and thus attribute the feature to a numerical artefact of the approximation. However, the decoupling properties depend quite sensitively on the pulse duration.

In case of strong driving, the two filter functions are closer in amplitude for lower frequencies. In addition, \mathcal{F}_x also peaks at $\omega = \omega_0 \pm \Omega_R$. These peaks also show up at higher frequencies in the dephasing filter function \mathcal{F}_z , reflecting frequency mixing in the strong coupling regime. While both filter functions show characteristics of a DCG in the weak driving regime, that is they drop to zero as $\omega \rightarrow 0$, this is not the case in the strong driving regime. Instead, there they approach a constant level for small frequencies. On top of rotation errors from timing inaccuracies, we may thus expect naive strong driving gates to be more susceptible to quasistatic noise than weak driving gates. By shaping the pulse envelope of the strong driving gate the decoupling properties could be recovered.

19.3 Randomized Benchmarking

Standard randomized benchmarking (SRB) and related methods, for example interleaved randomized benchmarking (IRB), are popular tools to assess the quality of a qubit system and the operations used to control it [178, 227, 228]. The basic protocol consists of constructing K random sequences of varying length m of gates drawn from the Clifford group,¹ and appending a final inversion gate so that the identity operation should be performed in total. Each of these pulse sequences is applied to an initial state $|\psi\rangle$ in order to measure the survival probability $p(|\psi\rangle)$ after the sequence. In reality, the applied operations are subject to noise and experimental imprecisions. This renders them imperfect and results in a survival probability smaller than one. Assuming gate-independent errors, the average gate fidelity F_{avg} is then obtained by fitting the measured survival probabilities for each sequence length to the zeroth-order exponential model [178]

$$p(|\psi\rangle) = A \left(1 - \frac{dr}{d-1}\right)^m + B, \quad (19.1)$$

where $r = 1 - F_{\text{avg}}$ is the average error per single gate to be extracted from the fit, A and B are parameters capturing state preparation and measurement (SPAM) errors, and d is the dimensionality of the system.

One of the main assumptions of the SRB protocol is that temporal correlations of the noise are small on timescales longer than the average gate time [178]. If this requirement is not satisfied, *e.g.* if $1/f$ noise plays a dominant role, the decay of the sequence fidelity can have non-exponential components [230–232] and a single exponential fit will not produce the true average gate fidelity [233, 234]. The filter-function formalism suggests itself to numerically probe RB experiments in such systems for two reasons. First, it enables the study of gate performance subject to noise with correlation times longer than individual gate times. This regime, where a simple description in terms of individual, isolated quantum operations fails, is accessible in the filter-function formalism because universal classical noise can be included by the power spectral density $S(\omega)$. Second, the simulation of a RB experiment can be performed efficiently by using the concatenation property. Because RB sequences are compiled from a limited set of gates whose filter functions may be precomputed, one only needs to concatenate m filter functions for a single sequence of length m to gain access to the survival probability.

Since for sufficiently long RB sequences $r \in \mathcal{O}(1)$, and we would need to include the frequency shifts Δ in a full simulation following Equation 16.9 because the low-noise approximation Equation 16.43 does not hold in this regime. Unfortunately, the concatenation property does not hold for Δ . Therefore, we focus on the high-fidelity regime where the exponential decay of the sequence fidelity may be approximated to linear order and only the decay amplitudes Γ need to be considered.

In order to evaluate the survival probability of a RB experiment using filter functions, we employ the state fidelity from Subsection 16.4.2 and focus on the single-qubit case with $d = 2$ and the (normalized) Pauli basis from Equation 16.54. Because the ideal action of a RB sequence is the identity we have $\mathcal{Q} = \mathbb{1}$. Assuming we prepare and measure in the computational basis, $|\psi\rangle \in \{|0\rangle, |1\rangle\}$ so that $\sqrt{2} |\rho\rangle\rangle = |\sigma_0\rangle\rangle \pm |\sigma_3\rangle\rangle$, we

1: The Clifford group is a subgroup of the special unitary group with the advantage that compositions are easy to compute and that averaging over all unitaries can under reasonable assumptions be replaced by averaging over all Cliffords. This makes the Clifford gates a convenient choice for benchmarking. For a nice, short introduction as well as further references, see [229]

simplify Equation 16.50 to

$$\begin{aligned} F(|\psi\rangle, \mathcal{U}_{\text{RB}}(|\psi\rangle\langle\psi|)) &= \frac{1}{2}(\tilde{\mathcal{U}}_{00} + \tilde{\mathcal{U}}_{33} \pm \tilde{\mathcal{U}}_{03} \pm \tilde{\mathcal{U}}_{30}) = \frac{1 + \tilde{\mathcal{U}}_{33}}{2} \\ &\approx 1 - \frac{1}{2} \sum_{k \neq 3} \Gamma_{kk}. \end{aligned} \quad (19.2)$$

For the second equality we used that $\tilde{\mathcal{U}}$ is trace-preserving and unital (cf. Subsection 16.1.2) while in the last step we approximated the expression using Equations 16.22 and 16.43. For our simulation, we neglect SPAM errors so that $A = B = 0.5$, choose $|\psi\rangle = |0\rangle$, and approximate Equation 19.1 as

$$p(|0\rangle) = F(|0\rangle, \mathcal{U}_{\text{RB}}(|0\rangle\langle 0|)) \approx 1 - rm \quad (19.3)$$

for small gate errors $r \ll 1$ since this is the regime which we can efficiently simulate using the concatenation property.

We simulate single-qubit SRB experiments using three different gate sets to generate the 24 elements of the Clifford group. For the first gate set we implement the group by naive “single” rotations about the symmetry axes of the cube. Each pulse corresponds to a single time segment during which one rotation is performed so that the j th element is given by $Q_j = \exp(-i\phi_j \mathbf{n}_j \cdot \boldsymbol{\sigma})$. We compile the other two gate sets from primitive $\pi/2$ x - and y -rotations so that on average each Clifford gate consists of 3.75 primitive gates (see Reference 235). For the specific implementation of the primitive $\pi/2$ -gates we compare “naive” rotations, *i.e.* with a single time segment so that $Q_j = \exp(-i\pi\sigma_j/4)$ for $j \in \{x, y\}$, and the “optimized” gates from Reference 219. Pulse durations are chosen such that the average duration of all 24 Clifford gates generated from a single gate set is equal for all three gate sets. This is to ensure that the different implementations of the Clifford gates are sensitive to the same noise frequencies.

We investigate white noise and correlated noise with $S(\omega) \propto \omega^{-0.7}$ assuming the same noise spectrum on each Cartesian axis of the Bloch sphere and normalize the noise power for each gate set and noise type (white and correlated) so that the average Clifford infidelity r is the same throughout. We then randomly draw $K = 100$ sequences for 11 different lengths $m \in [1, 101]$ and concatenate the m Clifford gates using Equation 16.29 to compute the control matrix of the entire sequence. For the integral in Equation 16.24 we choose the ultraviolet cutoff frequency two orders of magnitude above the inverse duration of the shortest pulse, $f_{\text{UV}} = 10^2/\tau_{\text{min}}$. Similarly, the infrared cutoff is chosen as $f_{\text{IR}} = 10^{-2}/m_{\text{max}}\tau_{\text{max}}$ with $m_{\text{max}} = 101$ and $\tau_{\text{max}} = 7\tau_{\text{min}}$ (since the longest gate is compiled from seven primitive gates with duration τ_{min}) to guarantee that all nontrivial structure of the filter functions is adequately resolved at small frequencies.² Finally, we fit Equation 19.3 to the infidelities computed for the different noise spectra.

The results of the simulation are shown in Figure 19.3(a) and (b) for white and correlated noise, respectively. For white noise, the survival probability agrees well with the SRB prediction for all gate types whereas for $1/f$ -like noise the “single” gates (green pluses) deviate considerably. Hence, fitting the zeroth-order SRB model to such data will not reveal the true average gate fidelity although errors are of order unity. We note that References 230 and 166 found similar results using different methods for $1/f$ and perfectly correlated DC noise, respectively. The former observed SRB to estimate r within 25 % and the latter found the mean of the

2: For a precise fidelity estimate, the infrared cutoff should be extended to $f = 0$. However, we are only interested in a qualitative picture and neglect this part of the spectrum here. At frequencies much smaller than $\approx 1/\tau$ where τ is the duration of the entire control operation, the filter function is constant and we therefore do not disregard any interesting features by setting $f_{\text{IR}} = 10^{-2}/\tau = 10^{-2}/m_{\text{max}}\tau_{\text{max}}$.

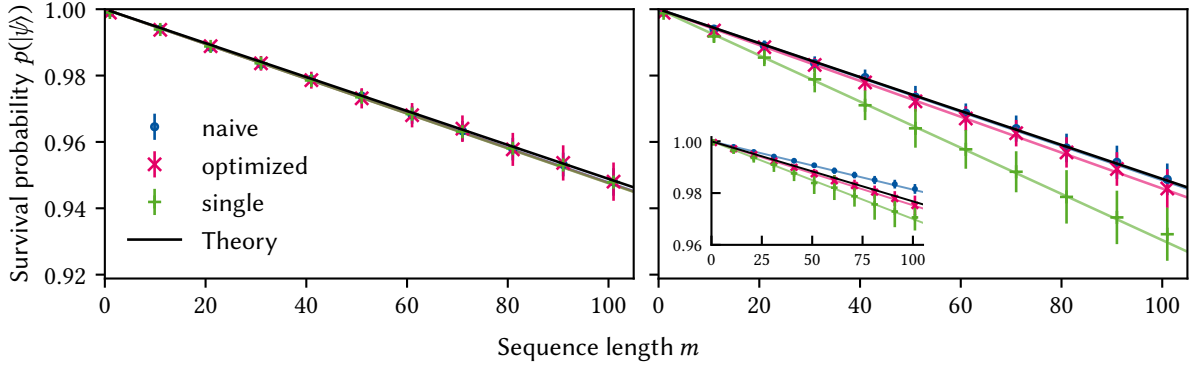


Figure 19.3: Simulation of a SRB experiment using 100 random sequences per point for different gate and noise types (see the main text for an explanation of the gate type monikers). Dashed lines are fits of Equation 19.3 to the data while the solid black lines correspond to a zeroth-order SRB model with $A = B = 0.5$ and the true average gate infidelity per Clifford r . Errorbars show the standard deviation of the SRB sequence fidelities, illustrating that for the “single” gate set noise correlations can lead to amplified destructive and constructive interference of errors. The same noise spectrum is used for all three error channels (σ_x , σ_y , σ_z) and the large plots show the sum of all contributions. (a) Uncorrelated white noise with the noise power adjusted for each gate type so that the average error per gate r is constant over all gate types. No notable deviation is seen between different gate types. (b) Correlated $1/f$ -like noise with noise power adjusted to match the average Clifford fidelity in (a). The decay of the “single” gate set differs considerably from that of the other gate sets and the SRB decay expected for the given average gate fidelity, whereas “naive” and “optimized” gates match the zeroth order SRB model well, indicating that correlations in the noise affect the relation between SRB decay and average gate fidelity in a gate-set-dependent way. Inset: contributions from σ_z -noise show that the sequence fidelity can be better than expected for certain gate types and noise channels.

SRB fidelity distribution to deviate from the mode, thereby giving rise to incorrectly estimated fidelities.

On top of affirming the findings by the references, our results demonstrate that the accuracy of the predictions made by SRB theory, *i. e.* that the RB decay rate directly corresponds to the average error rate of the gates, not only depends on the gate implementation but also on which error channels are assumed. This can be seen from the inset of Figure 19.3(b), where only dephasing noise (σ_z) contributions are shown. For this noise channel and the “naive” gates (blue points), one finds a slower RB decay than expected from the actual average gate fidelity, so that the latter would be overestimated by an RB experiment, whereas the “single” gates show the opposite behavior. Depending on the gate set and relevant error channels, non-Markovian noise may thus even lead to improved sequence fidelities due to errors interfering destructively. This behavior is captured by the pulse correlation filter functions whose contributions to the sequence fidelity lead to the deviations from the SRB prediction.

Notably, the data for the “optimized” gates (magenta crosses) agree with the prediction for every noise channel individually which implies that correlations between pulses are suppressed. This highlights the formalism’s attractiveness for numerical gate optimization as the pulse correlation filter functions $\mathcal{F}^{(gg')}(\omega)$ may be exploited to suppress correlation errors. To be more explicit, the correlation decay amplitudes $\Gamma^{(gg')}$ from Equation 16.31 can be used to construct cost functions for quantum optimal control algorithms like gradient ascent pulse engineering (GRAPE) [236, 237] or chopped random-basis (CRAB) [238]. By constructing linear combinations of $\Gamma^{(gg')}$ with different pulse indices g and g' , correlations between any number of pulses can be specifically targeted and suppressed using numerical pulse optimization.

19.4 Quantum Fourier transform

To demonstrate the flexibility of our software implementation, we calculate filter functions for a four-qubit quantum Fourier transform (QFT) [55, 239] circuit. The QFT routine plays an important role in many quantum algorithms such as Shor’s algorithm [240] and quantum phase estimation [55]. For the underlying gate set, we assume a standard Rabi driving model with in-phase/quadrature (IQ) control and nearest neighbor exchange. That is, we assume full control of the x - and y -axes of the individual qubits as well as the exchange interaction mediating coupling between two neighboring qubits. This system allows for native access to the minimal gate set $\mathcal{G} = \{X_i(\pi/2), Y_i(\pi/2), \text{CR}_{ij}(\pi/2^3)\}$ where $\text{CR}_{ij}(\phi)$ denotes a controlled rotation by ϕ about z with control qubit i and target qubit j . Controlled- z rotations by angles $\pi/2^m$ as required for the QFT can thus be obtained by concatenating 2^{3-m} minimal gates $\text{CR}_{ij}(\pi/2^3)$.

Despite native access to all necessary gates, we employ QuTiP’s implementation [171] of the GRAPE algorithm [236, 237] to generate the gates in order to highlight our method’s suitability for numerically optimized pulses. For the optimization we choose a time step of $\Delta t = 1$ ns and a total gate duration of $\tau = 30$ ns. For completeness, see Section E.3 for details on the optimized gates. We then construct the remaining required gates by sequencing these elementary gates, *i.e.* the Hadamard gate $H_i = X_i(\pi/2) \circ X_i(\pi/2) \circ Y_i(\pi/2)$, where $B \circ A$ denotes the composition of gates A and B such that gate A is executed before gate B . To map the canonical circuit [55] onto our specific qubit layout with only nearest-neighbor coupling, we furthermore introduce SWAP operations to couple distant qubits. These gates can be implemented by three CNOTs, $\text{SWAP}_{ij} = \text{CNOT}_{ij} \circ \text{CNOT}_{ji} \circ \text{CNOT}_{ij}$. The CNOTs in turn are obtained by a Hadamard transform of the controlled phase gate, $\text{CNOT}_{ij} = H_j \circ \text{CR}_{ij}(\pi) \circ H_j$. The complete quantum circuit is shown at the top of Figure 19.4; for the canonical circuit with all-to-all connectivity refer to Reference 55. In total, there are 442 elementary pulses, 198 of which are required for the three SWAPs on the first two qubits, so that the entire algorithm would take ~ 13 μ s to run. Note that the circuit could be compressed in time by parallelizing some operations but for simplicity we only execute gates sequentially and do not execute dedicated idling gates.

In order to leverage the extensibility of the filter function approach (see Section 16.7), we use a Pauli basis for the pulses and proceed as follows:

1. Instantiate the `PulseSequence` objects for the elementary gates \mathcal{G} for the first two qubits and cache the control matrices.
2. Compile all required single- and two-qubit pulses by concatenating the `PulseSequences` that implement \mathcal{G} .
3. Extend the `PulseSequences` to the full four-qubit Hilbert space.
4. Recursively concatenate recurring gate sequences by concatenating four-qubit `PulseSequences`, *e.g.* $\text{SWAP}_{10} \circ \text{CR}_{10}(\pi/2^1) \circ H_0$, in order to optimally use the performance benefit offered by Equation 16.29.
5. Concatenate the last `PulseSequences` to get the complete QFT pulse.

For our gate parameters and 400 frequency points, this procedure takes around 5 s on an Intel® Core™ i9-9900K eight-core processor, whereas computing the filter functions naively using Equation 16.36 takes around 4 min. The resulting filter functions are shown in Figure 19.4 for the noise operators affecting the first qubit. Evidently, the fidelity of the algorithm is most susceptible to DC noise; below roughly $1 \mu\text{s}^{-1}$ the filter

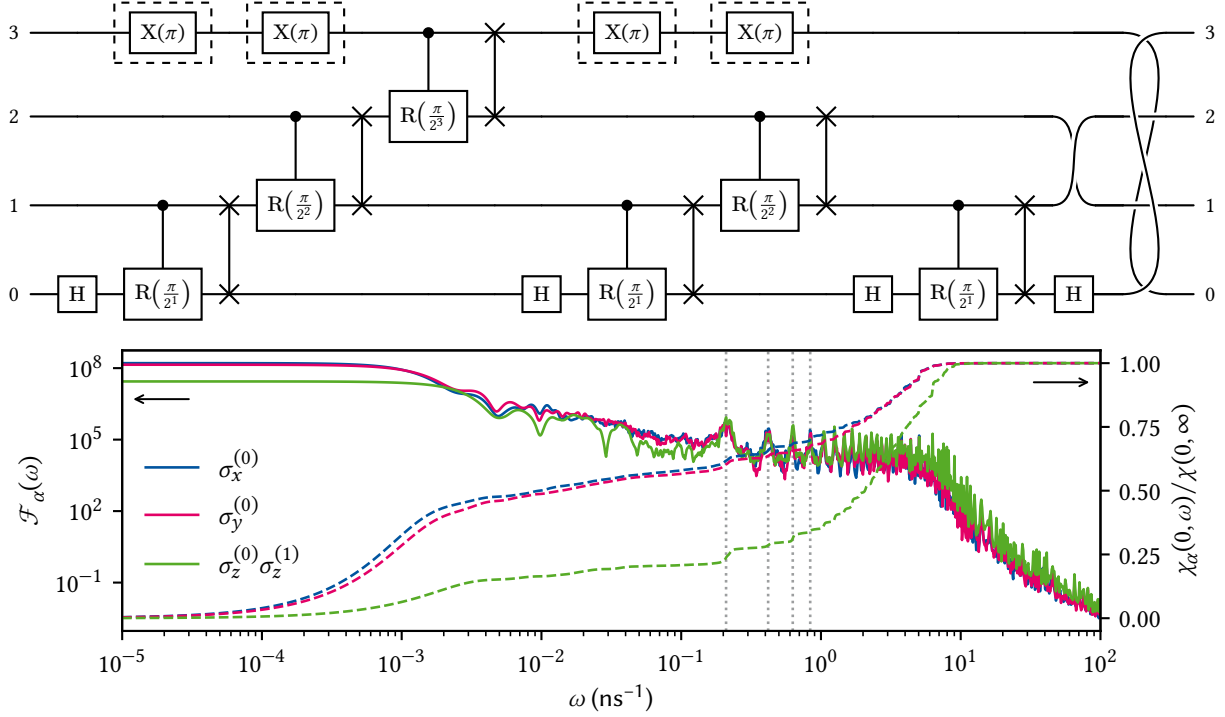


Figure 19.4: Top: Circuit for a QFT on four qubits with nearest-neighbor coupling. Labels next to the wires indicate the qubit index with the permutations at the end of the circuit replacing the final SWAP operations. X-gates in dashed boxes indicate optional echo pulses that leave the action nominally unchanged. Bottom: Filter functions for noise operators on the first qubit ($i = 0$) without echoes. Dotted gray lines indicate the positions of the n th harmonic, $\omega_n = 2\pi n/\tau$ with $\tau = 30$ ns the duration of the gates in G, for $n \in \{1, 2, 3, 4\}$. The filter functions have a baseline of around 10^4 in the range $\omega \in [10^{-1}, 10^1]$ ns $^{-1}$ before they drop down to follow the usual $1/\omega^2$ behavior. The dashed lines show the error sensitivities $\chi_\alpha(\omega_1, \omega_2) := \int_{\omega_1}^{\omega_2} d\omega \mathcal{F}_\alpha(\omega)$ in the frequency band $[0, \omega]$ as a fraction of the total sensitivity $\chi_\alpha(0, \infty)$. These are closely related to the entanglement fidelity (cf. Equations 16.26 and 16.49) and suggest that high frequencies up to the knee at $\omega \approx 10$ ns $^{-1}$ cannot be neglected if the cutoff frequency of the noise is sufficiently high or the spectrum does not drop off quickly enough (note the linear scale as opposed to the logarithmic scale for the filter functions).

functions level off at their maximum value. In the GHz range there is a plateau with sharp peaks corresponding to the n harmonics of the inverse pulse duration $\omega_n = 2\pi n/\tau$, where the leftmost belongs to $n = 1$. The dashed lines show the error sensitivities $\chi_\alpha(\omega_1, \omega_2) := \int_{\omega_1}^{\omega_2} d\omega \mathcal{F}_\alpha(\omega)$ in the frequency band $[0, \omega]$ relative to the total sensitivity $\chi_\alpha(0, \infty)$. For a white spectrum, *i.e.* $S(\omega) = \text{const.}$, this quantifies the fraction of the total entanglement infidelity that is accumulated up to frequency ω (cf. Equations 16.26 and 16.49). Thus, to obtain a precise estimate of the algorithm's fidelity, five frequency decades need to be taken into account.

To obtain insight into the efficacy of running DD sequences on idling qubits in an algorithm, we insert spin echoes (two $X(\pi)$ gates amounting to an identity gate) on the fourth qubit before and after the gate operations taking place on this qubit. Exploiting the fact that we assemble the final filter function by concatenating the filter functions of each of the 16 clock cycles, we compute the pulse correlation infidelities (cf. Equations 16.31 and 16.48 as well as Equation 11 of Reference 124),

$$I_{\alpha\beta}^{(gg')} = \frac{1}{d} \text{tr} \Gamma_{\alpha\beta}^{(gg')}, \quad g, g' \in \{0, 1, \dots, 15\} \quad (19.4)$$

for $\alpha = \beta \equiv \sigma_y^{(3)}$. The off-diagonal elements of this matrix ($g \neq g'$) capture correlation effects that arise from the concatenation operation alone, while the diagonal elements correspond to the contributions from each single pulse³ individually. In particular, off-diagonal contributions

3: Or here rather: each single clock cycle of the circuit.

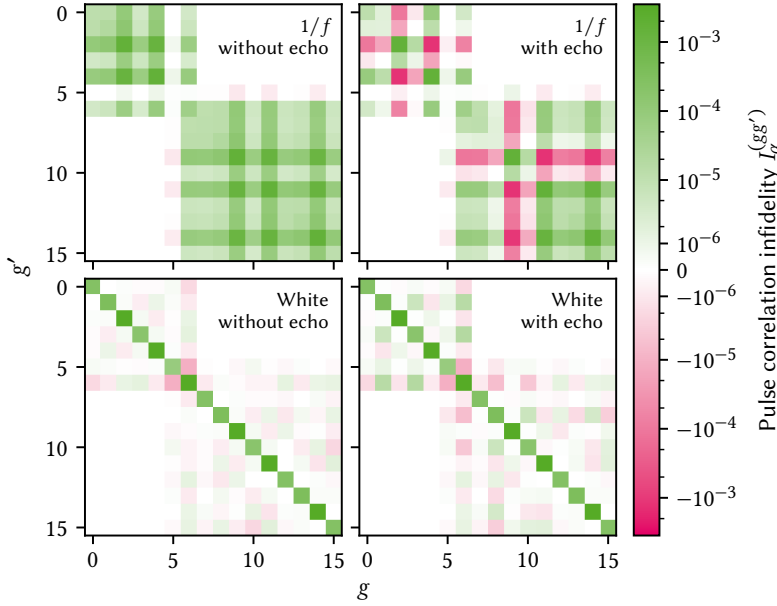


Figure 19.5: Pulse correlation infidelity contributions $I^{(gg')}$ for the noise operator $\sigma_y^{(3)}$ and different noise types (rows) and circuits (columns). The right column corresponds to the circuit with the $X(\pi)$ pulses indicated with dashed boxes in Figure 19.4 inserted, causing echo effects that reduce the overall infidelity for correlated noise. For uncorrelated noise, their effect is negligible.

can be negative, leading to a reduction in infidelity (an enhancement in fidelity) compared to the naive picture of simply adding all individual infidelities,⁴ $I = \sum_g I^{(gg')}$. For uncorrelated (white) noise, we expect $I^{(gg')} \approx 0$ for $g \neq g'$ because the noise has no “memory”, that is, cannot transport effects from one time step to another. Indeed, the sum rule for fidelity filter functions, which we prove in Subsection E.1.4, states that for white noise the fidelity depends only on the total duration τ and can therefore not be influenced by whichever control operation happened before or after. This stands in contrast to correlated (e.g., $1/f$) noise, where interference can cause random phases picked up at one point in the sequence be reversed at another [124].

In Figure 19.5, we show the correlation infidelities $I^{(gg')}$ computed for the QFT algorithm shown in Figure 19.4. The figure shows results for $1/f$ noise in the top row, and white noise in the bottom, while the first column shows the algorithm without the echo pulses and the second with. To facilitate a qualitative comparison, the noise level in the simulation was adjusted so that for white noise the total infidelity without echoes was the same as for $1/f$ noise. The infidelity in the case of white noise is indeed dominated by the diagonal elements as we would expect. Adding decoupling pulses does not change the fidelity significantly as the addition does not change the total duration of the circuit. In the case of $1/f$ noise, however, the picture is quite different. Here, the overall fidelity is reduced in the circuit without echos as there are significant contributions from correlations at $g \neq g'$. Adding the echo pulses causes some of these contributions to change sign and lead to a reduction in total infidelity of this noise channel by a factor of five. In Section G.1, we perform MC and GKSL master equation simulations of the QFT circuit to validate the fidelity predictions made by the filter-function formalism.

These insights demonstrate that our method represents a useful tool to analyze how and to which degree small algorithms are affected by correlated errors, and how this effect depends on the gate implementation. It could thus also be used to choose or optimize gates in an algorithm-specific way.

4: Recall that we are approximating the error process to linear order so that $F \sim \prod_g \exp(1 - \epsilon_g) \approx 1 - \sum_g \epsilon_g$.

Before we conclude, let us address two possible avenues for future work, one for the formalism itself and one for its application.

To extend our approach to the filter-function formalism beyond the scope discussed in this work, the most evident path forward is to allow for quantum mechanical baths instead of purely classical ones. Such an extension would facilitate studying for example non-unital T_1 -like processes. In fact, the filter-function formalism was originally introduced considering quantum baths such as spin-boson models [148, 149] or more general baths [147, 153, 241], but it remains an open question whether this can be applied to our presentation of the formalism and the numerical implementation in particular. In a fully quantum-mechanical treatment, (sufficiently weak) noise coupling into the quantum system can be modelled via a set of bath operators $\{D_\alpha(t)\}_\alpha$ so that $H_n(t) = \sum_\alpha B_\alpha(t) \otimes D_\alpha(t)$ (the classical case is recovered by replacing $D_\alpha(t) \rightarrow b_\alpha(t)\mathbb{1}$) [242]. Accordingly, the ensemble average over the stochastic bath variables $\{b_\alpha(t)\}_\alpha$ needs to be replaced by the quantum expectation value $\text{tr}_B(\cdot \rho_B)$ with respect to the state ρ_B of the bath B . One therefore needs to deal with correlation functions of bath operators instead of stochastic variables. An immediate consequence for numerical applications is hence an increased dimensionality of the system, which could be dealt with by using analytical expressions for the partial trace over the bath.

For future applications of our method, it would be interesting to study the effects of noise correlations in quantum error correction (QEC) schemes [7, 243, 244]. While extensive research has been performed on QEC, noise is usually assumed to be uncorrelated between error correction cycles. In this respect, our formalism may shed light on effects that need to be taken into account for a realistic description of the protocol. As outlined above, we can compute expectation values of (stabilizer) measurements in a straightforward manner from the error transfer matrix. Unfortunately, this implies performing the ensemble average over different noise realizations, therefore removing all correlations between subsequent measurement outcomes for a given noise realization. Hence, the same feature that allows us to calculate the quantum process for correlated noise, namely that we compute only the final map by averaging over all “paths” leading to it, prevents us from studying correlations between consecutive cycles. To overcome this limitation in the context of quantum memory one could invoke the principle of deferred measurement [55] and move all measurements to the end of the circuit, replacing classically controlled operations dependent on the measurement outcomes by conditional quantum operations. Alternatively, to incorporate the probabilistic nature of measurements, one could devise a branching model that implements the classically controlled recovery operation by following both conditional branches of measurement outcomes with weights corresponding to the measurement probabilities as computed from the ensemble-averaged error transfer matrix. An intriguing connection also exists to the quantum Zeno effect, for which quantum systems subject to periodic projective measurements have been identified with a filter function [147, 245, 246].

As quantum control schemes become more sophisticated and take into account realistic hardware constraints and sequencing effects, their analytical description becomes cumbersome, making numerical tools inval-

able for analyzing pulse performance. In the above, we have shown that the filter-function formalism lends itself naturally to these tasks since the central objects of our formulation, the interaction picture noise operators, obey a simple composition rule which can be utilized to efficiently calculate them for a sequence of quantum gates. Because the nature of the noise is encoded in a power spectral density in the frequency domain, its effects are isolated from the description of the control until they are evaluated by the overlap integral of noise spectrum and filter function. Hence, the noise operators are highly reusable in calculations and can serve as an economic way of simulating pulse sequences.

Building on the results of a separate publication [124], we have presented a general framework to study decoherence mechanisms and pulse correlations in quantum systems coupled to generic classical noise environments. By combining the quantum operations and filter-function formalisms, we have shown how to compute the Liouville representation of the exact error channel of an arbitrary control operation in the presence of Gaussian noise. For non-Gaussian noise our results become perturbative in the noise strength. Furthermore, we have introduced the `filter_functions` Python software package that implements the aforementioned method. We showed both analytically and numerically that our software implementation can outperform Monte Carlo techniques by orders of magnitude. By employing the formalism and software to study several examples we demonstrated the wide range of possible applications.

The capacity for applications in quantum optimal control has already been established above. In a forthcoming publication, we will present analytical derivatives for the fidelity filter function, Equation 16.26, and their implementation in the software package [215]. Together with the infidelity, Equation 16.49, they can serve as efficient cost functions for pulse optimization in the presence of realistic, correlated noise [172]. Since our method offers insight into correlations between pulses at different positions in a sequence, the pulse correlation filter function $F^{(gg')}(\omega)$ with $g \neq g'$ can additionally serve as a tool for studying under which conditions pulses decouple from noise with long correlation times. Such insight would be valuable to design pulses for algorithms. Another interesting application could be quantum error correction in the regime of long-time correlated noise as outlined above, where we also briefly touched upon a possible extension of the framework to quantum mechanical baths.

The tools presented here, both analytical and numerical as implemented in the `filter_functions` software package [170], provide an accessible way for computing filter functions in generic control settings across the different material platforms employed in quantum technologies and beyond.

Acknowledgements This part of the present thesis is based in large parts

APPENDIX

Filter Functions



E.1 Additional derivations

In this appendix we show additional derivations omitted from the main text.

E.1.1 Derivation of the single-qubit cumulant function in the Liouville representation

For a single qubit, the Pauli basis $\{\sigma_i\}_{i=0}^3 = 1/\sqrt{2} \times \{\mathbb{1}, \sigma_x, \sigma_y, \sigma_z\}$ is a natural choice to define the Liouville representation. In this case, the trace tensor Equation 16.18 can be simplified and thus Equation 16.17 given a more intuitive form which we derive in this appendix. Since the cumulant function is linear in the noise indices α, β we drop them in the following for legibility. Our results hold for both a single pair of noise indices and the total cumulant. We start by observing the relation

$$T_{klj} = \text{tr}(\sigma_k \sigma_l \sigma_j) = \frac{1}{2}(\delta_{kl}\delta_{ij} - \delta_{ki}\delta_{lj} + \delta_{kj}\delta_{li}) \quad (\text{E.1})$$

for the Pauli basis elements $\sigma_k, k \in \{1, 2, 3\}$. Including the identity element σ_0 in the trace tensor gives additional terms. However, as we show now none of these contribute to \mathcal{K} because they cancel out.

First, since the noise Hamiltonian $H_n(t)$ is traceless and therefore $\tilde{\mathcal{B}}_{\alpha 0}(t) = 0$, we have $\Gamma_{kl}, \Delta_{kl} \propto (1 - \delta_{k0})(1 - \delta_{l0})$, i.e. the first column and row of both the decay amplitude and frequency shift matrices are zero, and hence terms in the sum of Equation 16.17 with either $k = 0$ or $l = 0$ vanish. Next, for $i = j = 0$ all of the traces cancel out as can be easily seen. The last possible cases are given by $i = 0, j \neq 0$ and vice versa. For these cases we have

$$T_{kl0j} = T_{klj0} = \frac{1}{\sqrt{2}} \text{tr}(\sigma_k \sigma_l \sigma_j) = \frac{i}{2} \varepsilon_{klj} \quad (\text{E.2})$$

with ε_{klj} the completely antisymmetric tensor. Both of the above cases vanish in \mathcal{K} since, taking the case $j = 0$ for example,

$$\frac{1}{2} (T_{kl0i} - T_{k0li} - T_{kil0} + T_{ki0l}) = \frac{i}{2} (\varepsilon_{kli} - \varepsilon_{kli} - \varepsilon_{kil} + \varepsilon_{kil}) = 0 \quad (\text{E.3a})$$

for the decay amplitudes Γ and

$$\frac{1}{2} (T_{kl0i} - T_{lk0i} - T_{kli0} + T_{lki0}) = \frac{i}{2} (\varepsilon_{kli} - \varepsilon_{lki} - \varepsilon_{kli} + \varepsilon_{lki}) = 0 \quad (\text{E.3b})$$

for the frequency shifts Δ . Hence, only terms with $i, j > 0$ contribute and we can plug the simplified expressions for the trace tensor T_{klj} , Equation E.1, into Equation 16.17 to write the cumulant function for a single

E.1 Additional derivations 160

E.1.1 Derivation of the single-qubit cumulant function in the Liouville representation 160

E.1.2 Evaluation of the integrals in Equation 16.40 . . 161

E.1.3 Simplifying the calculation of the entanglement infidelity 161

E.1.4 Sum rule 162

E.2 Singlet-Triplet Gate Fidelity 163

E.3 GRAPE-optimized gate set for QFT 164

E.4 Convergence Bounds 165

E.4.1 Magnus Expansion 166

E.4.2 Infidelity 167

qubit and the Pauli basis concisely as

$$\mathcal{K}_{ij}(\tau) = -\frac{1}{2} \sum_{kl} \left[\Delta_{kl} (T_{klji} - T_{lkji} - T_{klij} + T_{lkij}) \right. \\ \left. + \Gamma_{kl} (T_{klji} - T_{kjli} - T_{kilj} + T_{kijl}) \right] \quad (\text{E.4})$$

$$= -\sum_{kl} \left[\Delta_{kl} (\delta_{ki} \delta_{lj} - \delta_{kj} \delta_{li}) + \Gamma_{kl} (\delta_{kl} \delta_{ij} - \delta_{kj} \delta_{li}) \right] \quad (\text{E.5})$$

$$= \Delta_{ji} - \Delta_{ij} + \Gamma_{ij} - \delta_{ij} \text{tr } \Gamma \quad (\text{E.6})$$

$$= \begin{cases} -\sum_{k \neq i} \Gamma_{kk} & \text{if } i = j, \\ -\Delta_{ij} + \Delta_{ji} + \Gamma_{ij} & \text{if } i \neq j, \end{cases} \quad (\text{E.7})$$

as given in the main text.

E.1.2 Evaluation of the integrals in Equation 16.40

Here we calculate the integrals appearing in the calculation of the frequency shifts Δ , Equation 16.41, given by

$$I_{ijmn}^{(g)}(\omega) = \int_{t_{g-1}}^{t_g} dt e^{i\Omega_{ij}^{(g)}(t-t_{g-1})-i\omega t} \int_{t_{g-1}}^t dt' e^{i\Omega_{mn}^{(g)}(t'-t_{g-1})+i\omega t'}. \quad (\text{E.8})$$

The inner integration is simple to perform and we get

$$I_{ijmn}^{(g)}(\omega) = \int_{t_{g-1}}^{t_g} dt e^{i\Omega_{ij}^{(g)}(t-t_{g-1})-i\omega(t-t_{g-1})} \\ \times \begin{cases} \frac{e^{i(\omega+\Omega_{mn}^{(g)})(t-t_{g-1})} - 1}{i(\omega + \Omega_{mn}^{(g)})} & \text{if } \omega + \Omega_{mn}^{(g)} \neq 0 \\ t - t_{g-1} & \text{if } \omega + \Omega_{mn}^{(g)} = 0. \end{cases} \quad (\text{E.9})$$

Shifting the limits of integration and performing integration by parts in the case $\omega + \Omega_{mn}^{(g)} = 0$ then yields

$$I_{ijmn}^{(g)}(\omega) = \begin{cases} \frac{1}{\omega + \Omega_{mn}^{(g)}} \left(\frac{e^{i(\Omega_{ij}^{(g)} - \omega)\Delta t_g - 1}}{\Omega_{ij}^{(g)} - \omega} - \frac{e^{i(\Omega_{ij}^{(g)} + \Omega_{mn}^{(g)})\Delta t_g - 1}}{\Omega_{ij}^{(g)} + \Omega_{mn}^{(g)}} \right) & \text{if } \omega + \Omega_{mn}^{(g)} \neq 0, \\ \frac{1}{\Omega_{ij}^{(g)} - \omega} \left(\frac{e^{i(\Omega_{ij}^{(g)} - \omega)\Delta t_g - 1}}{\Omega_{ij}^{(g)} - \omega} - i\Delta t_g e^{i(\Omega_{ij}^{(g)} - \omega)\Delta t_g} \right) & \text{if } \omega + \Omega_{mn}^{(g)} = 0 \wedge \Omega_{ij}^{(g)} - \omega \neq 0, \\ \frac{\Delta t_g^2}{2} & \text{if } \omega + \Omega_{mn}^{(g)} = 0 \wedge \Omega_{ij}^{(g)} - \omega = 0. \end{cases} \quad (\text{E.10})$$

E.1.3 Simplifying the calculation of the entanglement infidelity

In the main text, we claimed that the contribution of noise sources (α, β) to the total entanglement infidelity $I_{\text{ent}}(\tilde{\mathcal{U}}) = \sum_{\alpha\beta} I_{\alpha\beta}$ reduces from the trace of the cumulant function \mathcal{K} to

$$I_{\alpha\beta} = -\frac{1}{d^2} \text{tr } \mathcal{K}_{\alpha\beta} \quad (\text{E.11})$$

$$= \frac{1}{d} \text{tr } \Gamma_{\alpha\beta}. \quad (\text{E.12})$$

To show this, we substitute \mathcal{K} by its definition in terms of Δ and Γ according to Equation 16.17. This yields for the trace

$$\begin{aligned}\mathrm{tr} \mathcal{K}_{\alpha\beta} &= -\frac{1}{2} \sum_{kl} \delta_{ij} (f_{ijkl} \Delta_{\alpha\beta,kl} + g_{ijkl} \Gamma_{\alpha\beta,kl}) \\ &= -\frac{1}{2} \sum_{ikl} \Gamma_{\alpha\beta,kl} (T_{klii} + T_{lkii} - 2T_{kili})\end{aligned}\quad (\text{E.13})$$

since Δ is antisymmetric. In order to further simplify the trace tensors on the right hand side of Equation E.13, we observe that the orthonormality and completeness of the operator basis \mathbf{C} defining the Liouville representation of \mathcal{K} (cf. Equation 16.14) is equivalent to requiring that $\mathbf{C}^\dagger \mathbf{C} = \mathbb{1}$ with \mathbf{C} reshaped into a $d^2 \times d^2$ matrix by a suitable mapping. This condition may also be written as

$$\begin{aligned}\delta_{ac} \delta_{bd} &= \sum_k C_{k,ab}^* C_{k,cd} \\ &= \sum_k C_{k,ba} C_{k,cd}\end{aligned}\quad (\text{E.14})$$

because every element C_k is Hermitian. Using this relation in Equation E.13 then yields

$$\begin{aligned}\mathrm{tr} \mathcal{K}_{\alpha\beta} &= -\frac{1}{2} \sum_{kl} \Gamma_{\alpha\beta,kl} (2d\delta_{kl} - 2\mathrm{tr}(C_k)\mathrm{tr}(C_l)) \\ &= -d\mathrm{tr} \Gamma_{\alpha\beta}.\end{aligned}\quad (\text{E.15})$$

The last equality only holds true for bases with a single non-traceless element (the identity), such as the bases discussed in Section 16.8. This is because in this case, $\mathrm{tr}(C_k) = 0$ for $k > 0$ whereas $\Gamma_{\alpha\beta,kl} = 0$ for either $k = 0$ or $l = 0$ since Γ is a function of the traceless noise Hamiltonian for which $\mathrm{tr}(C_0 H_n) \propto \mathrm{tr} H_n = 0$ (i.e. the first column of the control matrix is zero, see Equations 16.16 and 16.21). Finally, substituting Equation E.15 into Equation E.11 we obtain our result

$$I_{\alpha\beta} = \frac{1}{d} \mathrm{tr} \Gamma_{\alpha\beta}. \quad (\text{E.16})$$

E.1.4 Sum rule

For white noise, the infidelity to leading order does not depend on the internal dynamics of the control operation but only on the total duration τ . To see this, take Equation 16.21 and substitute the correlation function of white noise, $\langle b_\alpha(t_1) b_\alpha(t_2) \rangle = S_0 \delta(t_1 - t_2)$. The integrals then simplify to

$$\Gamma_{\alpha\alpha,kl} = S_0 \int_0^\tau dt \tilde{\mathcal{B}}_{\alpha k}(t) \tilde{\mathcal{B}}_{\alpha l}(t). \quad (\text{E.17})$$

In order to compute the infidelity, we require the trace over the matrix of decay amplitudes (Equation 16.48), so

$$I_\alpha = \frac{S_0}{d} \mathrm{tr} \Gamma_{\alpha\alpha} = \frac{1}{d} \sum_k \int_0^\tau dt \tilde{\mathcal{B}}_{\alpha k}^2(t). \quad (\text{E.18})$$

Now recall that $\tilde{\mathcal{B}}$ is a vector on Liouville space and we can write $\tilde{\mathcal{B}}_\alpha(t) \doteq |\tilde{B}_\alpha(t)\rangle\rangle \equiv \langle\langle \tilde{B}_\alpha(t) |$ because it is Hermitian. Thus,

$$I_\alpha = \frac{S_0}{d} \int_0^\tau dt \langle\langle \tilde{B}_\alpha(t) | \tilde{B}_\alpha(t) \rangle\rangle = \frac{1}{d} \int_0^\tau dt \|\tilde{B}_\alpha(t)\|^2, \quad (\text{E.19})$$

and if $B_\alpha(t) = B_\alpha$, i. e., is time-independent, the integral evaluates simply to τ ,

$$I_\alpha = \frac{S_0 \tau}{d} \|\tilde{B}_\alpha\|^2, \quad (\text{E.20})$$

because the control unitary $U_c(t)$ conserves the norm. Since also $I_\alpha = \int d\omega / 2\pi d S(\omega) \mathcal{F}_\alpha(\omega)$ with the fidelity filter function $\mathcal{F}_\alpha(\omega)$ (Equations 16.26 and 16.49), this result also implies the sum rule

$$\int \frac{d\omega}{2\pi} \mathcal{F}_\alpha(\omega) = \tau \|\tilde{B}_\alpha\|^2, \quad (\text{E.21})$$

a result previously obtained by Cywiński et al. [150]. This means that pulse shaping and similar techniques never yield a leading-order fidelity enhancement if the noise is white in the relevant regime of frequencies as the fidelity only depends on the total duration of the pulse.

E.2 Singlet-Triplet Gate Fidelity

In this appendix we lay out in more detail how the fidelity of the optimized S-T₀ qubit gates from Reference 235 was calculated using filter functions. In two singlet-triplet qubits, angular momentum conservation suppresses occupancy of states with non-vanishing magnetic spin quantum number m_s so that the total accessible state space of dimension $d = 6$ is spanned by $\{|\uparrow\downarrow\uparrow\downarrow\rangle, |\uparrow\downarrow\downarrow\uparrow\rangle, |\downarrow\uparrow\uparrow\downarrow\rangle, |\downarrow\uparrow\downarrow\uparrow\rangle, |\uparrow\uparrow\downarrow\downarrow\rangle, |\downarrow\downarrow\uparrow\uparrow\rangle\}$. A straightforward method to single out the computational subspace (CS) dynamics from those on the whole space would be to simply project the error transfer matrix $\tilde{\mathcal{U}} \approx \mathbb{1} + \mathcal{K}$ with \mathcal{K} the cumulant function onto the CS as proposed by Wood and Gambetta [198], that is calculate the fidelity as $F_{\text{ent}} = d_c^{-2} \text{tr}(\Pi_c \tilde{\mathcal{U}})$ where Π_c is the Liouville representation of the projector onto the CS and $d_c = 4$ the dimension of the CS. However, here we use a more involved procedure in order to gain more insight from the error transfer matrix as well as to obtain a better comparison to the fidelities computed by Cerfontaine et al. [235], who map the final 6×6 propagator to the closest unitary on the 4×4 CS during their Monte Carlo simulation.

To calculate the fidelity of the target unitary on the 4×4 CS, we thus construct an orthonormal operator basis \mathbf{C} of the full 6×6 space that is partitioned into elements which are nontrivial only on the CS on the one hand and elements which are nontrivial only on the remaining space on the other such that $\mathbf{C} = \mathbf{C}^c \cup \mathbf{C}^\ell$. Using such a basis, we can then trace only over CS elements of the error transfer matrix $\tilde{\mathcal{U}}$ in Equation 16.46 to obtain the fidelity of the gate on the CS. Moreover, we retain the opportunity to characterize the gates on the basis of the Pauli matrices.

Since there is no obvious way to extend the Pauli basis for two qubits to the complete space we proceed as follows: For the CS, we pad the

two-qubit Pauli basis with zeros on the leakage levels, *i.e.*

$$C_i^c \doteq \begin{matrix} & |\uparrow\uparrow\downarrow\downarrow\rangle & |\downarrow\downarrow\uparrow\uparrow\rangle \\ \begin{matrix} \langle\uparrow\uparrow\downarrow\downarrow| \\ \langle\downarrow\downarrow\uparrow\uparrow| \end{matrix} & \begin{pmatrix} P_i & 0 & 0 \\ 0 & 0 & 0 \\ 0 & 0 & 0 \end{pmatrix} \end{matrix}, \quad i \in \{0, \dots, 15\}, \quad (\text{E.22})$$

where the P_i are normalized two-qubit Pauli matrices (*cf.* Equation 16.54) in the basis $\{|\uparrow\uparrow\downarrow\downarrow\rangle, |\uparrow\downarrow\uparrow\downarrow\rangle, |\downarrow\uparrow\uparrow\downarrow\rangle, |\downarrow\downarrow\uparrow\uparrow\rangle\}$. To complete the basis we require an additional 20 elements orthogonal to the 16 padded Pauli matrices. We obtain the remaining elements by first expanding the C_i^c in an arbitrary basis $\{\Lambda_i\}_{i=0}^{35}$ of the complete space (we choose a generalized Gell-Mann (GGM) basis, Equation 16.55, for simplicity), yielding a 16×36 matrix of expansion coefficients:

$$M_{ij} = \text{tr}(C_i^c \Lambda_j). \quad (\text{E.23})$$

We then compute an orthonormal vector basis V (a matrix of size 36×20) for the null space of M using singular value decomposition $M = U\Sigma V^\dagger$ and acquire the corresponding basis matrices as

$$C_i^\ell = \sum_j \Lambda_j V_{ji}, \quad i \in \{0, \dots, 19\}. \quad (\text{E.24})$$

Finally, to account for the fact that Reference 235 map the total propagator to the closest unitary on the CS, we exclude the identity Pauli element $C_0^c \propto \text{diag}(1, 1, 1, 1, 0, 0)$ from the trace over the computational subspace part of \tilde{U} represented in the basis $C = C^c \cup C^\ell$ when calculating the fidelity,

$$F_{\text{ent}} = \frac{1}{16} \sum_{i=1}^{15} \tilde{U}_{ii}, \quad (\text{E.25})$$

since for unitary operations on the CS we have $\mathcal{K}_{00} \approx 1 - \tilde{U}_{00} = 1 - \text{tr}(C_0^c \tilde{U} C_0^c \tilde{U}^\dagger) = 0$. Hence, excluding \tilde{U}_{00} from the trace corresponds to partially disregarding non-unitary components of the error channel on the computational subspace. Although not the only element that differs compared to the closest subspace unitary, \mathcal{K}_{00} contains the most obvious contribution, whereas those of other elements are more difficult to disentangle into unitary and non-unitary components.

Similar to the fidelity, we also obtain the canonical filter function shown in panel (b) of Figure 19.1 by summing only over columns one through 15 of the control matrix, $F_{\epsilon_{ij}}(\omega) = \sum_{k=1}^{15} |\tilde{B}_{\epsilon_{ij}k}(\omega)|^2$. In fact, including the first column, corresponding to the padded identity matrix C_0^c , in the filter function removes the DCG character of $F_{\epsilon_{12}}(\omega)$ and $F_{\epsilon_{34}}(\omega)$, which instead approach a constant level of around 20 (note that the filter function is dimensionless in our units) at zero frequency. This is consistent with the fact that the gates were optimized using quasistatic and fast white noise contributions to the fidelity after mapping to the closest unitary on the computational subspace. We have performed Monte Carlo resimulations that support this reading. In Figure E.1 we show the filter functions once including and once excluding the contributions from C_0^c .

E.3 GRAPE-optimized gate set for QFT

For completeness, in this appendix we give details on the GRAPE-optimized pulses for the gate set $G = \{X_i(\pi/2), Y_i(\pi/2), \text{CR}_{ij}(\pi/2^3)\}$ used in Sec-

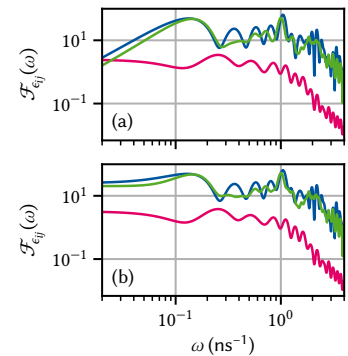


Figure E.1: Filter functions of the voltage detunings ϵ_{ij} excluding (a) and including (b) the zero-padded identity matrix basis element $C_0^c \propto \text{diag}(1, 1, 1, 1, 0, 0)$ for the computational subspace. Evidently, including C_0^c removes the dynamically corrected gate (DCG) character, namely that $F_{\epsilon_{ij}}(\omega) \rightarrow 0$ as $\omega \rightarrow 0$, of the gates but has little effect on the high-frequency behavior. As the pulse optimization minimizes, among other figures of merit, the infidelity of the final propagator mapped to the closest unitary on the computational subspace due to quasistatic and fast white noise, this indicates that excluding C_0^c from the filter function corresponds to partially ne-

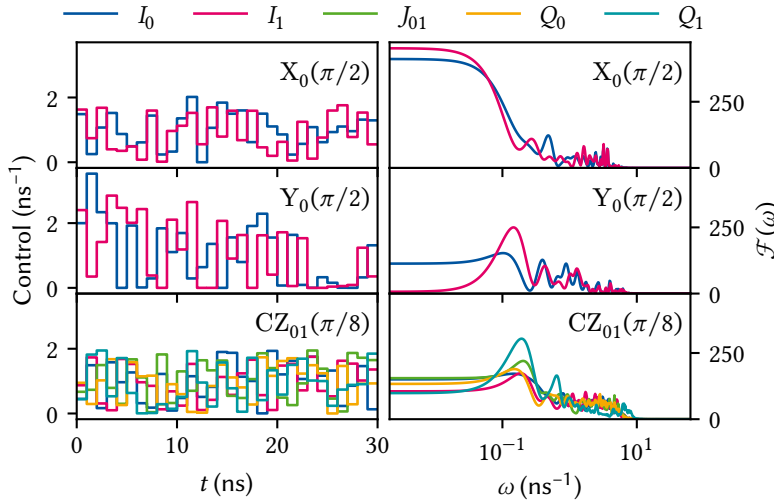


Figure E.2: Control fields (top row) and corresponding filter functions (bottom row) of the gradient ascent pulse engineering (GRAPE)-optimized pulses in G. (a),(b) $X_0(\pi/2)$; (c),(d) $Y_0(\pi/2)$; (e),(f) $CZ_{01}(\pi/8)$. Note that the optimization is neither very sophisticated nor realistic as the algorithm only maximizes the systematic (coherent) fidelity $\text{tr}(UQ_{\text{targ}}^\dagger)/d$ and the randomly distributed initial control amplitudes are not subject to any constraints.

tion 19.4 to simulate a quantum Fourier transform (QFT) algorithm. As mentioned in the main text, we consider a toy Rabi driving model with in-phase/quadrature (IQ) single-qubit control and exchange to mediate inter-qubit coupling. Cast in the language of quantum optimal control theory this translates to a vanishing drift (static) Hamiltonian, $H_d = 0$, and a control Hamiltonian in the rotating frame given by

$$H_c(t) = H_c^{(0)}(t) \otimes \mathbb{1} + \mathbb{1} \otimes H_c^{(1)}(t) + H_c^{(01)}(t), \quad (\text{E.26})$$

$$H_c^{(i)}(t) = I_i(t)\sigma_x^{(i)} + Q_i(t)\sigma_y^{(i)}, \quad (\text{E.27})$$

$$H_c^{(ij)}(t) = J_{ij}(t)\sigma_z^{(i)} \otimes \sigma_z^{(j)}, \quad (\text{E.28})$$

where $I_i(t)$ and $Q_i(t)$ are the in-phase and quadrature pulse envelopes and $\sigma_{x,y}^{(i)}$ are the Pauli matrices acting on the i th and extended trivially to the other qubit. As our goal is only of illustrative nature and not to provide a detailed gate optimization, we obtain the controls $\{I_0(t), Q_0(t), I_1(t), Q_1(t), J_{12}(t)\}$ for the gate set G using the GRAPE algorithm implemented in QuTiP [171] initialized with randomly distributed amplitudes. The resulting pulses and the corresponding filter functions for the relevant noise operators are shown in Figure E.2.

E.4 Convergence Bounds

In this appendix we give bounds for the convergence of the expansions employed in the main text for the case of purely autocorrelated noise, $S_{\alpha\beta}(\omega) = \delta_{\alpha\beta}S_{\alpha\beta}(\omega) = S_\alpha(\omega)$, following the approach by Green et al. [158]. For Gaussian noise, our expansion is exact when including first and second order Magnus expansion (ME) terms. Hence, the convergence radius of the Magnus expansion (ME) becomes infinite and the fidelity can be computed exactly by evaluating the matrix exponential Equation 16.11. For non-Gaussian noise, the following considerations apply.

E.4.1 Magnus Expansion

The ME of the error propagator Equation 16.8a converges if $\int_0^\tau dt \|\tilde{H}_n(t)\| < \pi$ with $\|A\|^2 = \langle A, A \rangle = \sum_{ij} |A_{ij}|^2$ the Frobenius norm [183]. We assume a time dependence of the noise operators of the form $B_\alpha(t) = s_\alpha(t)B_\alpha$. By the Cauchy-Schwarz inequality we then have

$$\begin{aligned} \|\tilde{H}_n(t)\|^2 &= \|H_n(t)\|^2 \\ &= \sum_{\alpha\beta} s_\alpha(t)s_\beta(t)b_\alpha(t)b_\beta(t)\langle B_\alpha, B_\beta \rangle \\ &\leq \sum_{\alpha\beta} s_\alpha(t)s_\beta(t)b_\alpha(t)b_\beta(t)\|B_\alpha\|\|B_\beta\| \\ &\leq \left[\sum_\alpha \sum_{g=1}^G \vartheta^{(m)}(t)s_\alpha^{(m)}b_\alpha^{(m)}\|B_\alpha\| \right]^2 \end{aligned} \quad (\text{E.29})$$

where $b_\alpha^{(m)}$ is the maximum value that the noise assumes during the pulse, $\vartheta^{(g)}(t) = \theta(t - t_{g-1}) - \theta(t - t_g)$ is one during the g th time interval and zero else, and where we approximated the time evolution as piecewise constant. Then, in order to guarantee convergence of the ME,

$$\begin{aligned} \int_0^\tau dt \|\tilde{H}_n(t)\| &\leq \int_0^\tau dt \left| \sum_\alpha \sum_{g=1}^G \vartheta^{(m)}(t)s_\alpha^{(m)}b_\alpha^{(m)}\|B_\alpha\| \right| \\ &= \sum_\alpha b_\alpha^{(m)}\|B_\alpha\| \sum_{g=1}^G s_\alpha^{(m)} \int_{t_{g-1}}^{t_g} dt \\ &= \sum_\alpha C_m \delta b_\alpha \|B_\alpha\| \sum_{g=1}^G s_\alpha^{(m)} \Delta t_g \\ &=: N \end{aligned} \quad (\text{E.30})$$

where we have expressed the in principle unknown maximum noise amplitude $b_\alpha^{(m)}$ in terms of the root mean square value δb_α . That is, $b_\alpha^{(m)} = C_m \langle b_\alpha(0)^2 \rangle^{1/2} = C_m \delta b_\alpha$ for a sufficiently large value C_m . Finally, realizing that $\delta b_\alpha^2 = \int \frac{d\omega}{2\pi} S_\alpha(\omega)$ and by the triangle inequality,

$$\begin{aligned} N &= C_m \sum_\alpha \|B_\alpha\| \left[\int_{-\infty}^{\infty} \frac{d\omega}{2\pi} S_\alpha(\omega) \right]^{1/2} \sum_{g=1}^G s_\alpha^{(m)} \Delta t_g \\ &\leq C_m \left[\sum_\alpha \|B_\alpha\|^2 \int_{-\infty}^{\infty} \frac{d\omega}{2\pi} S_\alpha(\omega) \left(\sum_{g=1}^G s_\alpha^{(m)} \Delta t_g \right)^2 \right]^{1/2} \\ &=: C_m \xi \\ &\stackrel{!}{<} \pi \end{aligned} \quad (\text{E.31})$$

where we have introduced the parameter ξ . Thus, the expansion converges if $\xi < \pi/C_m$. However, we note that in practice the rms noise amplitude δb_α will often be infinite, limiting the usefulness of this bound for certain noise spectra.

E.4.2 Infidelity

Again assuming a time dependence $B_\alpha(t) = s_\alpha(t)B_\alpha$ as well as piecewise-constant control, we note that for the infidelity we have (cf. Equation 16.46)

$$\begin{aligned}
 |\text{tr}(\Gamma)| &= \left| \sum_\alpha \int_0^\tau dt_2 \int_0^\tau dt_1 \langle b_\alpha(t_1)b_\alpha(t_2) \rangle \sum_k \tilde{\mathcal{B}}_{\alpha k}(t_1)\tilde{\mathcal{B}}_{\alpha k}(t_2) \right| \\
 &\leq \left| \sum_\alpha \int_0^\tau dt_2 \int_0^\tau dt_1 \langle b_\alpha(t_1)b_\alpha(t_2) \rangle \sum_{g,g'=1}^G \mathfrak{g}^{(m)}(t_1)\mathfrak{g}^{(g')}(t_2) s_\alpha^{(m)} s_\alpha^{(g')} \|B_\alpha\|^2 \right| \\
 &\leq \sum_\alpha \|B_\alpha\|^2 \underbrace{\langle b_\alpha^2(0) \rangle}_{\int \frac{d\omega}{2\pi} S_\alpha(\omega)} \sum_{g,g'=1}^G s_\alpha^{(m)} s_\alpha^{(g')} \left| \int_{t_{g'-1}}^{t_{g'}} dt_2 \int_{t_{g-1}}^{t_g} dt_1 \underbrace{\langle b_\alpha(t_1)b_\alpha(t_2) \rangle}_{|\cdot| \leq 1} \right| \\
 &\leq \sum_\alpha \left[\|B_\alpha\|^2 \int_{-\infty}^{\infty} \frac{d\omega}{2\pi} S_\alpha(\omega) \left(\sum_{g=1}^G s_\alpha^{(m)} \Delta t_g \right)^2 \right] \\
 &= \xi^2, \tag{E.32}
 \end{aligned}$$

where, going from the second to the third line, we have factored out the total power of noise source α from the cross-correlation function, $\langle b_\alpha(t_1)b_\alpha(t_2) \rangle = \langle b_\alpha^2(0) \rangle \langle \overline{b_\alpha(t_1)b_\alpha(t_2)} \rangle$. Thus, the first order infidelity Equation 16.46 is upper-bounded by $d^{-1}\xi^2$, the same parameter also bounding the convergence of the ME, and higher orders can be neglected if $\xi^2 \ll 1$.

Note that similar arguments can be made for the higher orders of the ME [158]. In particular, the n th order ME term containing n -point correlation functions of the noise is of order $\mathcal{O}(\xi^n)$ as stated in the main text.

Concatenation of second-order filter functions



In this appendix, we lay out how the second-order filter functions of atomic pulse segments can be reused to compute the filter function of the concatenated sequence. While it is not possible to perform the calculation entirely without concern for the internal structure of the individual segments due to the nested time integral (*cf.* Equation 16.40), it is also not necessary to compute everything from scratch as we show below.

We begin by setting some notation. Wherever possible, we omit indices and thus imply matrix multiplication between objects. We assume a single noise operator and drop the corresponding index; we can easily add them again later since none of the manipulations involve the noise indices. We fully adopt the picture that control matrices can be concatenated by summing over individual time steps, which may either be single piecewise-constant segments or entire sequences, corresponding to Equation 16.36 or Equation 16.29, respectively. To make clear that the control “matrices” are in fact vectors in Liouville space, we write them as bras wherever advantageous,¹

$$\tilde{B}(\omega) \doteq \langle\langle \tilde{B}(\omega) | \rangle. \quad (\text{F.1})$$

In the following, we will consider a sequence of piecewise-constant time steps split up into subsequences (“gates”) and will deal on the one hand with quantities that depend exclusively on the internal structure of a subsequence and those that do not on the other. For the former, we will denote their internal time step by a parenthesised superscript, *e.g.* $A^{(i)}$, which means the i th time step of A . The latter will have no superscript as they do not depend on the internal structure. We will furthermore distinguish between *local* quantities, which do not depend on the preceding dynamics (that is, are functions of the subsequence alone), and denote the subsequence index they belong to by a parenthesised subscript, *e.g.* $A_{(i)}$ for some quantity A of sequence i . Quantities which are *non-local* and thus depend on the preceding dynamics, but only on local quantities thereof, will have parenthesised subscripts with arrows indicating the range of the sequence, *e.g.* $A_{(i \rightarrow 1)}$ with $A_{(1 \rightarrow 1)} \equiv A_{(1)}$. By contrast, non-local quantities that depend on other non-local quantities will then be denoted in a “posterior” fashion, *e.g.*, $A_{(i|i-1 \rightarrow 1)}$ if A is a function of subsequence i and depends on all previous subsequences $i-1, \dots, 1$. As an illustrating example, consider the first-order concatenation rule for control matrices, Equation 16.29. With this notation, we can write it as²

$$\begin{aligned} \langle\langle \tilde{B}_{(g \rightarrow 1)}(\omega) | \rangle &= \sum_{g'=1}^g \langle\langle \tilde{B}_{(g'|g'-1 \rightarrow 1)}(\omega) | \rangle \\ &= \langle\langle \tilde{B}_{(1)}(\omega) | \rangle + \langle\langle \tilde{B}_{(2|1)}(\omega) | \rangle + \langle\langle \tilde{B}_{(3|2 \rightarrow 1)}(\omega) | \rangle + \dots \end{aligned} \quad (\text{F.2})$$

with

$$\langle\langle \tilde{B}_{(g|g-1 \rightarrow 1)}(\omega) | \rangle := e^{i\omega t_{g-1}} \langle\langle \tilde{B}_{(g)}(\omega) | \rangle \mathcal{Q}_{(g-1 \rightarrow 1)}, \quad (\text{F.3})$$

$$\mathcal{Q}_{(g-1 \rightarrow 1)} := \prod_{g'=g-1}^1 \mathcal{Q}_{(g')}, \quad (\text{F.4})$$

1: Recall our convention of using Roman font for Hilbert-space operators and calligraphic font for their Liouville-space duals.

2: The same definition holds for control matrices computed from Equation 16.36, in which case the subscripts would become superscripts. Similarly, sub- and superscripts can be combined.

where $\langle\langle \tilde{B}_{(g)}(\omega) \rangle\rangle$ is the control matrix of the g th gate and $\mathcal{Q}_{(g)}$ the corresponding control superpropagator. For complete sequences, typically denoted by $g = G$, we drop the subscript, $\langle\langle \tilde{B}_{(G \rightarrow 1)}(\omega) \rangle\rangle \equiv \langle\langle \tilde{B}(\omega) \rangle\rangle$. Finally, we drop the specifier $\mathcal{F}^{(2)}$ distinguishing the second- from the first-order filter function for brevity; in this section, we always mean the former.

We start from Equation 16.40, from which for reasons that will become clear shortly we define the second-order filter function by

$$\mathcal{F}_{\alpha\beta,kl}(\omega) := \mathcal{N}_{\alpha\beta,kl}(\omega) + \sum_{g=1}^G \mathcal{J}_{\alpha\beta,kl}^{(g|g-1 \rightarrow 1)}(\omega) \quad (\text{F.5})$$

with

$$\mathcal{N}_{\alpha\beta,kl}(\omega) := \sum_{g=1}^G \tilde{\mathcal{B}}_{\alpha k}^{(g|g-1 \rightarrow 1)*}(\omega) \tilde{\mathcal{B}}_{\beta l}^{(g-1 \rightarrow 1)}(\omega), \quad (\text{F.5a})$$

$$\mathcal{J}_{\alpha\beta,kl}^{(g|g-1 \rightarrow 1)}(\omega) := s_{\alpha}^{(g)} \tilde{B}_{\alpha,ij}^{(g)} \tilde{C}_{k,ji}^{(g \rightarrow 1)} I_{ijmn}^{(g)}(\omega) \tilde{C}_{l,nm}^{(g \rightarrow 1)} \tilde{B}_{\beta,mn}^{(g)} s_{\beta}^{(g)}, \quad (\text{F.5b})$$

\tilde{B} and \tilde{C} defined in Subsection 16.2.2, and where repeated indices are contracted. Comparing to the nested time integral, the first summand in the brackets contains all contributions from complete time segments up to the one containing the inner integration variable t , whereas the second captures the final, incomplete segment with $t_{g-1} < t \leq t_g$. Now imagine the sequence of piecewise-constant time steps, $g \in \{1, \dots, G\}$, being split apart at some index $1 < \gamma < G$ and thereby being divided into two subsequences $g \in \{1, \dots, \gamma\}$ and $h \in \{1, \dots, \eta\} \equiv g \in \{\gamma + 1, \dots, G\}$ with $G = \gamma + \eta$. Our goal is to obtain an expression for the second-order filter function $\mathcal{F}(\omega)$ that is – as much as possible – a sum of local terms of these subsequences g and h .

Up to γ , the filter function $\mathcal{F}_{(2 \rightarrow 1)}(\omega) \equiv \mathcal{F}(\omega)$ is simply that of the first sequence, $\mathcal{F}_{(1)}(\omega)$, and we thus have for $g > \gamma^3$

$$\begin{aligned} \mathcal{F}_{(2|1)}(\omega) &= \mathcal{F}(\omega) - \mathcal{F}_{(1)}(\omega) \\ &= \sum_{g=\gamma+1}^G \left[|\tilde{B}^{(g|g-1 \rightarrow 1)}(\omega)\rangle\langle\langle \tilde{B}^{(g-1 \rightarrow 1)}(\omega) \rangle\rangle + \mathcal{J}^{(g|g-1 \rightarrow 1)}(\omega) \right], \quad (\text{F.6}) \end{aligned}$$

where we already plugged in Equation F.5a. We must now express the quantities $\tilde{\mathcal{B}}^{(g|g-1 \rightarrow 1)}(\omega)$, $\tilde{\mathcal{B}}^{(g-1 \rightarrow 1)}(\omega)$, and $\mathcal{J}^{(g|g-1 \rightarrow 1)}(\omega)$ locally in terms of the index h . To this end, we first write down the step-wise control matrix $\tilde{\mathcal{B}}^{(g|g-1 \rightarrow 1)}(\omega)$ in the second sequence and split off phases and propagators from the first sequence,

$$\begin{aligned} \langle\langle \tilde{B}^{(g|g-1 \rightarrow 1)}(\omega) \rangle\rangle &= e^{i\omega t_g} \langle\langle \tilde{B}^{(g)}(\omega) \rangle\rangle \mathcal{Q}^{(g-1 \rightarrow 1)} \\ &= e^{i\omega(t_{\gamma} + t_h)} \langle\langle \tilde{B}_{(2)}^{(h)}(\omega) \rangle\rangle \mathcal{Q}_{(2)}^{(h-1)} \mathcal{Q}_{(1)} \\ &= e^{i\omega \tau_{(1)}} \langle\langle \tilde{B}_{(2)}^{(h|h-1 \rightarrow 1)}(\omega) \rangle\rangle \mathcal{Q}_{(1)} \\ &= \langle\langle \tilde{B}_{(2|1)}^{(h|h-1 \rightarrow 1)}(\omega) \rangle\rangle, \quad (\text{F.7}) \end{aligned}$$

where $\tau_{(1)} = t_{\gamma}$ is the duration of the first sequence and $h = g - \gamma$. Next, we consider the cumulative control matrix $\tilde{\mathcal{B}}^{(g-1 \rightarrow 1)}(\omega)$. Because in the total sequence it is given by the sum over all $\tilde{\mathcal{B}}^{(g'|g' \rightarrow 1)}(\omega)$ up to $g - 1$, we can split off the complete control matrix of the first sequence and express

3: We drop indices for legibility as stated above; $\mathcal{J}^{(g|g-1 \rightarrow 1)}(\omega)$ is a matrix on Liouville space, whereas $\tilde{\mathcal{B}}^{(g|g-1 \rightarrow 1)}(\omega)$ and $\tilde{\mathcal{B}}^{(g-1 \rightarrow 1)}(\omega)$ are Liouville-space row vectors and their product here is an outer product, $|\tilde{B}^{(g|g-1 \rightarrow 1)}(\omega)\rangle\langle\langle \tilde{B}^{(g-1 \rightarrow 1)}(\omega) \rangle\rangle$, resulting in a matrix on Liouville space.

the remainder by summing over $\tilde{B}_{(2|1)}^{(h)}(\omega)$ from Equation F.7:

$$\begin{aligned} \langle\langle \tilde{B}^{(g-1 \rightarrow 1)}(\omega) \rangle\rangle &= \langle\langle \tilde{B}_{(1)}(\omega) \rangle\rangle + e^{i\omega\tau_{(1)}} \sum_{h'=1}^{g-1-\gamma} \langle\langle \tilde{B}_{(2)}^{(h'|h' \rightarrow 1)}(\omega) \rangle\rangle \mathcal{Q}_{(1)} \\ &= \langle\langle \tilde{B}_{(1)}(\omega) \rangle\rangle + e^{i\omega\tau_{(1)}} \langle\langle \tilde{B}_{(2)}^{(h-1 \rightarrow 1)}(\omega) \rangle\rangle \mathcal{Q}_{(1)} \\ &= \langle\langle \tilde{B}_{(2 \rightarrow 1)}^{(h-1 \rightarrow 1)}(\omega) \rangle\rangle \end{aligned} \quad (\text{F.8})$$

Finally, we need to unravel $\mathcal{J}^{(g|g-1 \rightarrow 1)}(\omega)$. We start from Equation 16.36, consider a time step $g \geq \gamma$ in the second sequence with $h = g - \gamma$, and rewrite

$$\begin{aligned} \mathcal{J}_{kl}^{(g|g-1 \rightarrow 1)}(\omega) &= s_{(2)}^{(g)} \tilde{B}_{ij}^{(g)} \tilde{C}_{kji}^{(g \rightarrow 1)} I_{ijn}^{(g)}(\omega) \tilde{C}_{lmn}^{(g \rightarrow 1)} \tilde{B}_{mn}^{(g)} s_{(2)}^{(g)} \\ &= s_{(2)}^{(h)} \tilde{B}_{(2),ij}^{(h)} \tilde{C}_{(2 \rightarrow 1),kji}^{(h \rightarrow 1)} I_{ijn}^{(h)}(\omega) \tilde{C}_{(2 \rightarrow 1),lmn}^{(h \rightarrow 1)} \tilde{B}_{(2),mn}^{(h)} s_{(2)}^{(h)} \\ &= \mathcal{J}_{(2|1),kl}^{(h|h-1 \rightarrow 1)}(\omega) \end{aligned} \quad (\text{F.9})$$

because all quantities except for $\tilde{C}_{(2|1)}^{(g)}$ depend on their timestep g alone, and where i, j, m, n index the Hilbert space dimensions of the operators, while k, l are the usual indices for the basis elements and therefore Liouville space dimensions. On that term, we can factor out the propagators of the first complete sequence,⁴

$$\tilde{C}_{(2 \rightarrow 1),kij}^{(h \rightarrow 1)} = \left[V_{(2)}^{(h)\dagger} Q_{(2)}^{(h-1 \rightarrow 1)} Q_{(1)} C_k Q_{(1)}^\dagger Q_{(2)}^{(h-1 \rightarrow 1)\dagger} V_{(2)}^{(h)} \right]_{ij}. \quad (\text{F.10})$$

We can now finally put all pieces together and, starting from Equation F.6, plug in Equations F.7 to F.9, so that we obtain⁵

$$\begin{aligned} \mathcal{F}_{(2|1)}(\omega) &= \sum_{h=1}^{\eta} \left[|\tilde{B}_{(2|1)}^{(h|h-1 \rightarrow 1)}(\omega)\rangle\rangle \langle\langle \tilde{B}_{(2 \rightarrow 1)}^{(h-1 \rightarrow 1)}(\omega) \rangle\rangle + \mathcal{J}_{(2|1)}^{(h|h-1 \rightarrow 1)}(\omega) \right] \\ &= \sum_{h=1}^{\eta} \left\{ e^{-i\omega\tau_{(1)}} \mathcal{Q}_{(1)}^\top |\tilde{B}_{(2)}^{(h|h-1 \rightarrow 1)}(\omega)\rangle\rangle \right. \\ &\quad \times \left[\langle\langle \tilde{B}_{(1)}(\omega) \rangle\rangle + e^{i\omega\tau_{(1)}} \langle\langle \tilde{B}_{(2)}^{(h-1 \rightarrow 1)}(\omega) \rangle\rangle \mathcal{Q}_{(1)} \right] + \mathcal{J}_{(2|1)}^{(h|h-1 \rightarrow 1)}(\omega) \left. \right\}. \end{aligned} \quad (\text{F.11})$$

To simplify the unwieldy first summand in the curly braces further, we expand the product,

$$\begin{aligned} e^{-i\omega\tau_{(1)}} \mathcal{Q}_{(1)}^\top |\tilde{B}_{(2)}^{(h|h-1 \rightarrow 1)}(\omega)\rangle\rangle &\left[\langle\langle \tilde{B}_{(1)}(\omega) \rangle\rangle + e^{i\omega\tau_{(1)}} \langle\langle \tilde{B}_{(2)}^{(h-1 \rightarrow 1)}(\omega) \rangle\rangle \mathcal{Q}_{(1)} \right] \\ &= e^{-i\omega\tau_{(1)}} \mathcal{Q}_{(1)}^\top |\tilde{B}_{(2)}^{(h|h-1 \rightarrow 1)}(\omega)\rangle\rangle \langle\langle \tilde{B}_{(1)}(\omega) \rangle\rangle \\ &\quad + \mathcal{Q}_{(1)}^\top |\tilde{B}_{(2)}^{(h|h-1 \rightarrow 1)}(\omega)\rangle\rangle \langle\langle \tilde{B}_{(2)}^{(h-1 \rightarrow 1)}(\omega) \rangle\rangle \mathcal{Q}_{(1)}. \end{aligned} \quad (\text{F.12})$$

If we now pull in the sum over the time steps h , we can identify in the first term the control matrix and Equation F.2, and in the second the contribution from complete segments to the second-order filter function, Equation F.5a).⁶

$$\begin{aligned} \sum_{h=1}^{\eta} (\text{r.h.s Equation F.12}) \\ = e^{-i\omega\tau_{(1)}} \mathcal{Q}_{(1)}^\top |\tilde{B}_{(2)}(\omega)\rangle\rangle \langle\langle \tilde{B}_{(1 \rightarrow 1)}(\omega) \rangle\rangle + \mathcal{Q}_{(1)}^\top \mathcal{N}_{(2)}(\omega) \mathcal{Q}_{(1)}. \end{aligned} \quad (\text{F.13})$$

4: Note that the $Q_{(i)}$ here are Hilbert space propagators, not their Liouville space counter parts $\mathcal{Q}_{(i)}$, and that $Q_{(2)}^{(h-1 \rightarrow 1)} \equiv Q_{h-1}$ in the notation of Subsection 16.2.1.

5: Recall that \mathcal{Q} is the Liouville representation of the unitary operator Q and as such – and because our chosen basis C is Hermitian – is an orthogonal matrix for which $\mathcal{Q}^\top \mathcal{Q} = \mathbb{1}$.

6: We write explicitly $\langle\langle \tilde{B}_{(1 \rightarrow 1)}(\omega) \rangle\rangle$ to emphasize that this is the *cumulative* control matrix.

As a last step, we recognize that the bra in the first term is nothing else but Equation F.3 so that we can write the filter function succinctly as

$$\begin{aligned}\mathcal{F}_{(2|1)}(\omega) &= |\tilde{B}_{(2|1)}(\omega)\rangle\langle\tilde{B}_{(1\rightarrow 1)}(\omega)| + \mathcal{Q}_{(1)}^\top \mathcal{N}_{(2)}(\omega) \mathcal{Q}_{(1)} + \sum_{h=1}^{\eta} \mathcal{J}_{(2|1)}^{(h|h-1\rightarrow 1)}(\omega) \\ &= \mathcal{N}_{(2|1)}(\omega) + \sum_{h=1}^{\eta} \mathcal{J}_{(2|1)}^{(h|h-1\rightarrow 1)}(\omega).\end{aligned}\quad (\text{F.14})$$

In Equation F.14, all terms except the last are known ahead of time if the first- and second-order filter functions of the subsequences as well as the control matrix of the concatenated sequence have been computed. We can extend this result to sequences consisting of an arbitrary number of G subsequences with lengths $\{\eta_g\}_{g=1}^G$ by recursively shifting indices in Equation F.14 up by one and subsequently adding $\mathcal{F}_{(2|1)}(\omega)$, allowing us to write the concatenation rule for second-order filter functions as

$$\mathcal{F}(\omega) = \sum_{g=1}^G \mathcal{F}_{(g|g-1\rightarrow 1)}(\omega) \quad (\text{F.15})$$

$$= \sum_{g=1}^G \left[\mathcal{N}_{(g|g-1\rightarrow 1)}(\omega) + \sum_{h_g=1}^{\eta_g} \mathcal{J}_{(g|g-1\rightarrow 1)}^{(h_g|h_g-1\rightarrow 1)}(\omega) \right] \quad (\text{F.15a})$$

with

$$\begin{aligned}\mathcal{N}_{(g|g-1\rightarrow 1)}(\omega) &= |\tilde{B}_{(g|g-1\rightarrow 1)}(\omega)\rangle\langle\tilde{B}_{(g-1\rightarrow 1)}(\omega)| + \mathcal{Q}_{(g-1\rightarrow 1)}^\top \mathcal{N}_{(g)}(\omega) \mathcal{Q}_{(g-1\rightarrow 1)}\end{aligned}\quad (\text{F.15b})$$

and

$$\begin{aligned}\mathcal{J}_{(g|g-1\rightarrow 1),kl}^{(h|h-1\rightarrow 1)}(\omega) &= s_{(g)}^{(h)} \tilde{B}_{(g),ij}^{(h)} \tilde{C}_{(g\rightarrow 1),kji}^{(h\rightarrow 1)} I_{(g),ijmn}^{(h)}(\omega) \tilde{C}_{(g\rightarrow 1),lnm}^{(h\rightarrow 1)} \tilde{B}_{(g),mn}^{(h)} s_{(g)}^{(h)}.\end{aligned}\quad (\text{F.15c})$$

Equation F.15 is our final result. Before we analyze it in more detail, let us first briefly discuss the special case where $G = 1$. Then, $\mathcal{Q}_{(0)} = \mathbb{1}$, $\langle\tilde{B}_{(0)}| = 0$, and hence $|\tilde{B}_{(1)}(\omega)\rangle\langle\tilde{B}_{(0)}(\omega)| = 0$ so that Equation F.15 reduces to Equation F.5 as it should.

To compute the second-order filter function of a sequence of quantum gates most efficiently, Equation F.15 suggests the following procedure:

1. Compute the control matrix for all gates individually. This requires the quantities $V_{(g)}^{(h)}$, $\tilde{B}_{(g)}^{(h)}$, and $\mathcal{Q}_{(g)}$ to be computed, allowing them to be reused in Equation F.10.
2. Compute the second-order filter function for all gates individually. This requires the quantities $I_{(g)}^{(h)}(\omega)$ (Equation 16.41) and $\mathcal{N}_{(g)}(\omega)$ to be computed, allowing them to be reused in Equations F.15b and F.15c, respectively.
3. Compute the control matrix of the entire sequence. This requires the quantities $\tilde{B}_{(g|g-1\rightarrow 1)}(\omega)$ and $\tilde{B}_{(g\rightarrow 1)}(\omega)$ to be computed, allowing them to be reused in Equation F.15b.

In this way, the only computations that need to be performed once for each gate g to evaluate Equation F.15 are the outer product and matrix multiplications in Equation F.15b. Additionally, for every time step of the entire sequence, the quantity $\tilde{C}_{(g\rightarrow 1)}^{(h\rightarrow 1)}$ needs to be computed following

Equation F.10, the contraction in Equation F.15c performed, and finally $\mathcal{J}_{(g|g-1 \rightarrow 1)}^{(h|h-1 \rightarrow 1)}(\omega)$ added to the result. In total, this requires $\mathcal{O}(G + H)$ computations, where $H = \sum_{g=1}^G \eta_g$ is the total number of time steps, yielding a favorable linear scaling in H compared to a naive approach that is $\mathcal{O}(H^2)$ due to the nested time integral.

Monte Carlo and GKSL master equation simulations



G.1 Validation of QFT fidelities

In this section, we perform Gorini-Kossakowski-Sudarshan-Lindblad (GKSL) master equation and Monte Carlo (MC) simulations to verify the fidelities predicted for the QFT circuit in the main text. We focus on noise exclusively on the third qubit, entering through the noise operator $B_\alpha \equiv \sigma_y^{(3)}$.

this

We assemble the QFT circuit discussed in the main text from a minimal gate set consisting of three atomic gates, $G = \{X_i(\pi/2), Y_i(\pi/2), CR_{ij}(\pi/2^3)\}$ on or between qubits i and j . We consider a simple model involving four single-spin qubits with in-phase (I) and quadrature (Q) single-qubit control and nearest neighbor exchange coupling so that the control Hamiltonian reads

$$H_c(t) = \sum_{\langle i,j \rangle} I_i(t)\sigma_x^{(i)} + Q_i(t)\sigma_y^{(i)} + J_{ij}(t)\sigma_z^{(i)} \otimes \sigma_z^{(j)} \quad (G.1)$$

where $\sigma_\alpha^{(i)}$ is the trivial extension of the Pauli matrix σ_α of qubit i to the full tensor product Hilbert space. For simplicity, we assume periodic boundary conditions so that qubits 1 and 4 are nearest neighbors as well. Similarly, we define the noise Hamiltonian as

$$H_n(t) = \sum_{\langle i,j \rangle} b_I(t)\sigma_x^{(i)} + b_Q(t)\sigma_y^{(i)} + b_J(t)\sigma_z^{(i)} \otimes \sigma_z^{(j)} \quad (G.2)$$

with the noise fields $b_\alpha(t)$ for $\alpha \in \{I, Q, J\}$.

To validate the fidelity for white noise, we use a GKSL master equation [131, 132] in superoperator form. We represent linear maps $\mathcal{A} : \rho \rightarrow \mathcal{A}(\rho)$ by matrices in the Pauli transfer matrix (PTM) representation as (see Reference 123 for more details)

$$\mathcal{A}_{ij} := \text{tr}(\sigma_i \mathcal{A}(\sigma_j)) \quad (G.3)$$

and operators as column vectors (*i.e.*, generalized Bloch vectors) as

$$\rho_i := \text{tr}(\sigma_i \rho), \quad (G.4)$$

allowing us to write the Lindblad equation

$$\frac{d}{dt}\rho(t) = -i[H(t), \rho(t)] + \sum_\alpha \gamma_\alpha \left(L_\alpha \rho(t) L_\alpha^\dagger - \frac{1}{2} \{L_\alpha^\dagger L_\alpha, \rho(t)\} \right) \quad (G.5)$$

as a linear differential equation in matrix form,

$$\frac{d}{dt}\rho_i(t) = \sum_j \left(-i\mathcal{H}_{ij}(t) + \sum_\alpha \gamma_\alpha \mathcal{D}_{\alpha,ij} \right) \rho_j(t). \quad (G.6)$$

Here, $\mathcal{H}_{ij}(t) = \text{tr}(\sigma_i [H(t), \sigma_j])$ and $\mathcal{D}_{\alpha,ij} = \text{tr}(\sigma_i L_\alpha \sigma_j L_\alpha^\dagger - \frac{1}{2} \{L_\alpha^\dagger L_\alpha, \sigma_j\})$.

By setting $L_\alpha \equiv \sigma_y^{(3)}$ as well as $\gamma_\alpha \equiv S_0/2$ with S_0 the amplitude of the one-sided noise power spectral density (PSD) so that $S(\omega) = S_0$, we can compare the fidelity obtained from the filter functions to that from the explicit simulation of Equation G.6. The latter is computed as $F_{\text{avg}} =$

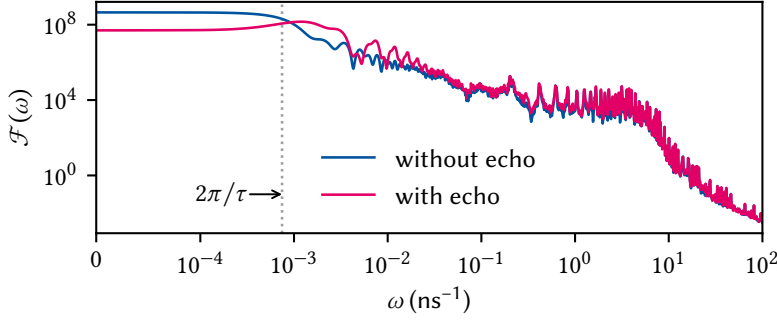


Figure G.1: Filter functions for noise operator $\sigma_y^{(3)}$ for the QFT circuit without (blue) and with (magenta) additional echo pulses. Introducing the echoes shifts spectral weight towards higher frequencies, reducing the DC level of the filter function by two orders of magnitude and thus leading to an improved fidelity for $1/f$ noise.

$d^{-2} \text{tr}(Q^\dagger \mathcal{U})$, where Q is the superpropagator due to the Hamiltonian evolution alone (*i.e.*, the ideal evolution without noise).

For the Monte Carlo simulation, we explicitly generate time traces of $b_Q(t)$ (*cf.* Equation G.2) by drawing pseudo-random numbers from a distribution whose PSD is $S(f) = S_0/f$. To do this, we draw complex, normally distributed samples in frequency space (*i.e.* white noise), scale it with the square root of the PSD, and finally perform the inverse Fourier transform. We choose an oversampling factor of 16 so that the time discretization of the simulation is $\Delta t_{\text{MC}} = \Delta t/16 = 62.5 \text{ ps}$ ($\Delta t = 1 \text{ ns}$ is the time step of the pulses used in the filter function (FF) simulation), leading to a highest resolvable frequency of $f_{\text{max}} = 16 \text{ GHz}$. Conversely, we increase the frequency resolution by sampling a time trace longer by a given factor, giving frequencies below f_{min} (16 kHz for pink, 0 Hz for white noise) weight zero, and truncating it to the number of time steps in the algorithm times the oversampling factor. This yields a time trace with frequencies $f \in [f_{\text{min}}, f_{\text{max}}]$ and a given resolution (we choose $\Delta f = 160 \text{ Hz}$). For reference, we show the fidelity filter functions for the circuit with and without echo pulses in this frequency band in Figure G.1.

We then proceed to diagonalize the Hamiltonian $H(t) = H_c(t) + H_n(t)$ and compute the propagator for one noise realization as

$$U(t) = \prod_g V^{(g)} \exp(-i\Omega^{(g)} \Delta t_{\text{MC}}) V^{(g)\dagger}, \quad (\text{G.7})$$

where $V^{(g)}$ is the unitary matrix of eigenvectors of $H(t)$ during time segment g and $\Omega^{(g)}$ the diagonal matrix of eigenvalues. Finally, we obtain an estimate for the average gate fidelity F_{avg} from the entanglement fidelity F_{ent} as

$$\langle F_{\text{avg}} \rangle = \left\langle \frac{dF_{\text{ent}} + 1}{d + 1} \right\rangle = \left\langle \frac{|\text{tr}(Q^\dagger U(\tau))|^2 + d}{d(d + 1)} \right\rangle. \quad (\text{G.8})$$

Here, $Q \equiv U_c(t = \tau)$ is the noise-free propagator at time τ of completion of the circuit and $\langle \cdot \rangle$ denotes the ensemble average over N Monte Carlo realizations of Equation G.7, *i.e.*, $\langle A \rangle = N^{-1} \sum_{i=1}^N A_i$. The standard error of the mean can be obtained as $\sigma_{\langle F_{\text{avg}} \rangle} = \sigma_{F_{\text{avg}}} / \sqrt{N}$ with $\sigma_{F_{\text{avg}}}$ the standard deviation over the Monte Carlo traces.

Table G.1 compares the infidelities $I = 1 - F$ from GKSL and MC simulations to the filter function predictions following Equation 16.48. Note that the precise value of the filter function result depends quite sensitively on the frequency sampling due to the sharp peaks in the gigahertz range (Figure G.1). As the table shows, both the GKSL and the MC cal-

Table G.1: Infidelities $I_{\text{avg}} = 1 - F_{\text{avg}}$ of the QFT circuit due to noise on $\sigma_y^{(3)}$. MC values are averages over $N = 1000$ random traces and have a relative error of 3 %. We included frequencies in the range of $\omega \in [0, 100] \text{ ns}^{-1}$ for white noise, and $\omega \in [100 \text{ ms}^{-1}, 100 \text{ ns}^{-1}]$ for pink noise. FF values are computed with $n_\omega = 1000$ samples logarithmically distributed over the same interval. Prefactors in the power law $S(\omega) = A\omega^\alpha$ are $2 \times 10^{-6} \text{ ns}^{-1}$ and 10^{-9} ns^{-2} , respectively.

METHOD	WHITE NOISE		$1/f$ NOISE	
	WITHOUT ECHO	WITH ECHO	WITHOUT ECHO	WITH ECHO
GKSL	8.38×10^{-3}	8.38×10^{-3}	—	—
MC	8.74×10^{-3}	8.00×10^{-3}	2.11×10^{-2}	4.28×10^{-3}
FF	8.38×10^{-3}	8.40×10^{-3}	2.12×10^{-2}	4.46×10^{-3}

culations agree well with the predictions made by our filter-function formalism.

Bibliography

- [1] Jonathan P. Dowling and Gerard J. Milburn. “Quantum Technology: The Second Quantum Revolution.” In: *Philosophical Transactions of the Royal Society of London. Series A: Mathematical, Physical and Engineering Sciences* 361.1809 (Aug. 15, 2003). Ed. by A. G. J. MacFarlane, pp. 1655–1674. DOI: [10.1098/rsta.2003.1227](https://doi.org/10.1098/rsta.2003.1227) (cited on page 2).
- [2] Alain Aspect. *Einstein and the Quantum Revolutions*. Trans. by David Kaiser Translated by Teresa Lavender Fagan. The France Chicago Collection. Chicago, IL: University of Chicago Press, Oct. 2024. 112 pp. (cited on page 2).
- [3] A. A. Clerk et al. “Introduction to Quantum Noise, Measurement, and Amplification.” In: *Reviews of Modern Physics* 82.2 (Apr. 15, 2010), pp. 1155–1208. DOI: [10.1103/RevModPhys.82.1155](https://doi.org/10.1103/RevModPhys.82.1155) (cited on page 2).
- [4] Tobias Hangleiter et al., *Python-Spectrometer* version 2024.11.1, Nov. 21, 2024. Zenodo. DOI: [10.5281/ZENODO.13789861](https://doi.org/10.5281/ZENODO.13789861), (cited on page 3).
- [5] Till Huckemann. PhD thesis. Aachen: RWTH Aachen University, 2025 (cited on page 20).
- [6] Dorit Aharonov, Alexei Kitaev, and John Preskill. “Fault-Tolerant Quantum Computation with Long-Range Correlated Noise.” In: *Physical Review Letters* 96.5 (Feb. 7, 2006), p. 050504. DOI: [10.1103/PhysRevLett.96.050504](https://doi.org/10.1103/PhysRevLett.96.050504) (cited on page 21).
- [7] Naomi H. Nickerson and Benjamin J. Brown. “Analysing Correlated Noise on the Surface Code Using Adaptive Decoding Algorithms.” In: *Quantum* 3 (Apr. 8, 2019), p. 131. DOI: [10.22331/q-2019-04-08-131](https://doi.org/10.22331/q-2019-04-08-131). arXiv: [1712.00502](https://arxiv.org/abs/1712.00502) (cited on pages 21, 149).
- [8] B. D. Clader et al. “Impact of Correlations and Heavy Tails on Quantum Error Correction.” In: *Physical Review A* 103.5 (May 24, 2021), p. 052428. DOI: [10.1103/PhysRevA.103.052428](https://doi.org/10.1103/PhysRevA.103.052428) (cited on page 21).
- [9] *csd — SciPy v1.15.2 Manual*. URL: <https://docs.scipy.org/doc/scipy-1.15.2/reference/generated/scipy.signal.csd.html> (visited on 04/15/2025) (cited on page 22).
- [10] J.S. Rojas-Arias et al. “Spatial Noise Correlations beyond Nearest Neighbors in ^{28}Si /Si-Ge Spin Qubits.” In: *Physical Review Applied* 20.5 (Nov. 9, 2023), p. 054024. DOI: [10.1103/PhysRevApplied.20.054024](https://doi.org/10.1103/PhysRevApplied.20.054024) (cited on page 22).
- [11] J. Yoneda et al. “Noise-Correlation Spectrum for a Pair of Spin Qubits in Silicon.” In: *Nature Physics* (Oct. 9, 2023). DOI: [10.1038/s41567-023-02238-6](https://doi.org/10.1038/s41567-023-02238-6) (cited on page 22).
- [12] Thomas Descamps et al. “Millikelvin Confocal Microscope with Free-Space Access and High-Frequency Electrical Control.” In: *Review of Scientific Instruments* 95.8 (Aug. 9, 2024), p. 083706. DOI: [10.1063/5.0200889](https://doi.org/10.1063/5.0200889) (cited on pages 24, 56).
- [13] Wolfgang P. Schleich et al. “Quantum Technology: From Research to Application.” In: *Applied Physics B* 122.5 (Apr. 27, 2016), p. 130. DOI: [10.1007/s00340-016-6353-8](https://doi.org/10.1007/s00340-016-6353-8) (cited on page 24).
- [14] Masoud Mohseni et al. “Commercialize Quantum Technologies in Five Years.” In: *Nature* 543.7644 (Mar. 2017), pp. 171–174. DOI: [10.1038/543171a](https://doi.org/10.1038/543171a) (cited on page 24).
- [15] *Quantum Technologies - BMBF*. Bundesministerium für Bildung und Forschung - BMBF. URL: https://www.bmbf.de/EN/Research/EmergingTechnologies/QuantumTechnologies/quantumtechnologies_node.html (visited on 06/20/2025) (cited on page 24).
- [16] *Quantum Technologies*. CEN-CENELEC. URL: <https://www.cenelec.eu/areas-of-work/cen-cenelec-topics/quantum-technologies/> (visited on 06/20/2025) (cited on page 24).
- [17] *Quantum | Shaping Europe’s Digital Future*. URL: <https://digital-strategy.ec.europa.eu/en/policies/quantum> (visited on 06/20/2025) (cited on page 24).
- [18] Markus Aspelmeyer, Tobias J. Kippenberg, and Florian Marquardt. “Cavity Optomechanics.” In: *Reviews of Modern Physics* 86.4 (Dec. 30, 2014), pp. 1391–1452. DOI: [10.1103/RevModPhys.86.1391](https://doi.org/10.1103/RevModPhys.86.1391) (cited on page 24).
- [19] Shabir Barzanjeh et al. “Optomechanics for Quantum Technologies.” In: *Nature Physics* 18.1 (Jan. 2022), pp. 15–24. DOI: [10.1038/s41567-021-01402-0](https://doi.org/10.1038/s41567-021-01402-0) (cited on page 24).

- [20] John Goold et al. “The Role of Quantum Information in Thermodynamics—a Topical Review.” In: *Journal of Physics A: Mathematical and Theoretical* 49.14 (Apr. 8, 2016), p. 143001. DOI: [10.1088/1751-8113/49/14/143001](https://doi.org/10.1088/1751-8113/49/14/143001) (cited on page 24).
- [21] Sebastian Deffner and Steve Campbell. *Quantum Thermodynamics: An Introduction to the Thermodynamics of Quantum Information*. Morgan & Claypool Publishers, July 1, 2019 (cited on page 24).
- [22] Loris Maria Cangemi, Chitrak Bhadra, and Amikam Levy. “Quantum Engines and Refrigerators.” In: *Physics Reports*. Quantum Engines and Refrigerators 1087 (Oct. 10, 2024), pp. 1–71. DOI: [10.1016/j.physrep.2024.07.001](https://doi.org/10.1016/j.physrep.2024.07.001) (cited on page 24).
- [23] Francesco Campaioli et al. “Colloquium: Quantum Batteries.” In: *Reviews of Modern Physics* 96.3 (July 9, 2024), p. 031001. DOI: [10.1103/RevModPhys.96.031001](https://doi.org/10.1103/RevModPhys.96.031001) (cited on page 24).
- [24] C. L. Degen, F. Reinhard, and P. Cappellaro. “Quantum Sensing.” In: *Reviews of Modern Physics* 89.3 (July 25, 2017), p. 035002. DOI: [10.1103/RevModPhys.89.035002](https://doi.org/10.1103/RevModPhys.89.035002) (cited on pages 24, 60).
- [25] Steven D. Bass and Michael Doser. “Quantum Sensing for Particle Physics.” In: *Nature Reviews Physics* 6.5 (May 2024), pp. 329–339. DOI: [10.1038/s42254-024-00714-3](https://doi.org/10.1038/s42254-024-00714-3) (cited on page 24).
- [26] W. Kohn and D. Sherrington. “Two Kinds of Bosons and Bose Condensates.” In: *Reviews of Modern Physics* 42.1 (Jan. 1, 1970), pp. 1–11. DOI: [10.1103/RevModPhys.42.1](https://doi.org/10.1103/RevModPhys.42.1) (cited on page 24).
- [27] A. A. High et al. “Spontaneous Coherence in a Cold Exciton Gas.” In: *Nature* 483.7391 (Mar. 2012), pp. 584–588. DOI: [10.1038/nature10903](https://doi.org/10.1038/nature10903) (cited on page 24).
- [28] Monique Combescot, Roland Combescot, and François Dubin. “Bose–Einstein Condensation and Indirect Excitons: A Review.” In: *Reports on Progress in Physics* 80.6 (June 1, 2017), p. 066501. DOI: [10.1088/1361-6633/aa50e3](https://doi.org/10.1088/1361-6633/aa50e3) (cited on page 24).
- [29] Yusuke Morita, Kosuke Yoshioka, and Makoto Kuwata-Gonokami. “Observation of Bose-Einstein Condensates of Excitons in a Bulk Semiconductor.” In: *Nature Communications* 13.1 (Sept. 14, 2022), p. 5388. DOI: [10.1038/s41467-022-33103-4](https://doi.org/10.1038/s41467-022-33103-4) (cited on page 24).
- [30] Lifu Zhang et al. “Electrical Control and Transport of Tightly Bound Interlayer Excitons in a MoSe₂/hBN/MoSe₂ Heterostructure.” In: *Physical Review Letters* 132.21 (May 24, 2024), p. 216903. DOI: [10.1103/PhysRevLett.132.216903](https://doi.org/10.1103/PhysRevLett.132.216903) (cited on page 24).
- [31] David D. Awschalom et al. “Quantum Technologies with Optically Interfaced Solid-State Spins.” In: *Nature Photonics* 12.9 (9 Sept. 2018), pp. 516–527. DOI: [10.1038/s41566-018-0232-2](https://doi.org/10.1038/s41566-018-0232-2) (cited on pages 24, 61).
- [32] Koji Azuma et al. “Quantum Repeaters: From Quantum Networks to the Quantum Internet.” In: *Reviews of Modern Physics* 95.4 (Dec. 20, 2023), p. 045006. DOI: [10.1103/RevModPhys.95.045006](https://doi.org/10.1103/RevModPhys.95.045006) (cited on pages 24, 61).
- [33] Tobias Heindel et al. “Quantum Dots for Photonic Quantum Information Technology.” In: *Advances in Optics and Photonics* 15.3 (Sept. 30, 2023), p. 613. DOI: [10.1364/AOP.490091](https://doi.org/10.1364/AOP.490091). arXiv: [2309.04229](https://arxiv.org/abs/2309.04229) [cond-mat, physics:quant-ph] (cited on page 24).
- [34] Joanna M. Zajac, Tobias Huber-Loyola, and Sven Hofling. *Quantum Dots for Quantum Repeaters*. May 12, 2025. DOI: [10.48550/arXiv.2503.13775](https://doi.org/10.48550/arXiv.2503.13775). Pre-published (cited on page 24).
- [35] Thomas Descamps. “Electrostatic Exciton Trap in a Thin Semiconductor Membrane for Optical Coupling to a GaAs Spin Qubit.” PhD thesis. Aachen: RWTH Aachen University, 2021 (cited on pages 24, 56, 62, 98, 100).
- [36] Takafumi Fujita et al. “Distinguishing Persistent Effects in an Undoped GaAs/AlGaAs Quantum Well by Top-Gate-Dependent Illumination.” In: *Journal of Applied Physics* 129.23 (June 21, 2021), p. 234301. DOI: [10.1063/5.0047558](https://doi.org/10.1063/5.0047558) (cited on page 56).
- [37] A. Shetty et al. “Effects of Biased and Unbiased Illuminations on Two-Dimensional Electron Gases in Dopant-Free GaAs/AlGaAs.” In: *Physical Review B* 105.7 (Feb. 7, 2022), p. 075302. DOI: [10.1103/PhysRevB.105.075302](https://doi.org/10.1103/PhysRevB.105.075302) (cited on page 56).
- [38] Huiyi Wang. “Stability Investigation of GaAs Quantum Dot Devices under Illumination.” MA thesis. Aachen: RWTH Aachen University, Nov. 4, 2023. 65 pp. (cited on page 56).
- [39] Maxim Reznikov. “Investigating Device Stability and Exploring New Materials for Semiconductor Spin Qubit Optical Interfaces.” MA thesis. Aachen: RWTH Aachen University, June 2024 (cited on pages 56, 100).

- [40] Kui Wu et al. “Modeling an Efficient Singlet-Triplet-Spin-Qubit-to-Photon Interface Assisted by a Photonic Crystal Cavity.” In: *Physical Review Applied* 21.5 (May 24, 2024), p. 054052. doi: [10.1103/PhysRevApplied.21.054052](https://doi.org/10.1103/PhysRevApplied.21.054052) (cited on page 56).
- [41] Meryem Benelajla et al. “Physical Origins of Extreme Cross-Polarization Extinction in Confocal Microscopy.” In: *Physical Review X* 11.2 (Apr. 7, 2021), p. 021007. doi: [10.1103/PhysRevX.11.021007](https://doi.org/10.1103/PhysRevX.11.021007) (cited on pages 56, 57).
- [42] Andreas V. Kuhlmann et al. “A Dark-Field Microscope for Background-Free Detection of Resonance Fluorescence from Single Semiconductor Quantum Dots Operating in a Set-and-Forget Mode.” In: *Review of Scientific Instruments* 84.7 (July 2013), p. 073905. doi: [10.1063/1.4813879](https://doi.org/10.1063/1.4813879) (cited on page 57).
- [43] P. Steindl et al. “Cross-Polarization-Extinction Enhancement and Spin-Orbit Coupling of Light for Quantum-Dot Cavity Quantum Electrodynamics Spectroscopy.” In: *Physical Review Applied* 19.6 (June 29, 2023), p. 064082. doi: [10.1103/PhysRevApplied.19.064082](https://doi.org/10.1103/PhysRevApplied.19.064082) (cited on page 57).
- [44] Robert H. Hadfield and Göran Johansson, eds. *Superconducting Devices in Quantum Optics*. Quantum Science and Technology. Cham: Springer International Publishing, 2016 (cited on page 58).
- [45] Harpreet Singh Arora et al. “Superconductivity in Metallic Twisted Bilayer Graphene Stabilized by WSe₂.” In: *Nature* 583.7816 (July 2020), pp. 379–384. doi: [10.1038/s41586-020-2473-8](https://doi.org/10.1038/s41586-020-2473-8) (cited on page 58).
- [46] Yiran Zhang et al. “Enhanced Superconductivity in Spin-Orbit Proximitized Bilayer Graphene.” In: *Nature* 613.7943 (Jan. 12, 2023), pp. 268–273. doi: [10.1038/s41586-022-05446-x](https://doi.org/10.1038/s41586-022-05446-x) (cited on page 58).
- [47] A. K. Geim and I. V. Grigorieva. “Van Der Waals Heterostructures.” In: *Nature* 499.7459 (July 2013), pp. 419–425. doi: [10.1038/nature12385](https://doi.org/10.1038/nature12385) (cited on page 58).
- [48] Alexander Popert et al. “Optical Sensing of Fractional Quantum Hall Effect in Graphene.” In: *Nano Letters* 22.18 (Sept. 28, 2022), pp. 7363–7369. doi: [10.1021/acs.nanolett.2c02000](https://doi.org/10.1021/acs.nanolett.2c02000) (cited on page 58).
- [49] Michele Masseroni et al. “Spin-Orbit Proximity in MoS₂/Bilayer Graphene Heterostructures.” In: *Nature Communications* 15.1 (Oct. 26, 2024), p. 9251. doi: [10.1038/s41467-024-53324-z](https://doi.org/10.1038/s41467-024-53324-z) (cited on page 58).
- [50] Tian Xie et al. *Optical Imaging of Flavor Order in Flat Band Graphene*. May 13, 2024. doi: [10.48550/arXiv.2405.08074](https://doi.org/10.48550/arXiv.2405.08074). Pre-published (cited on page 58).
- [51] Anna M Seiler et al. “Layer-Selective Spin-Orbit Coupling and Strong Correlation in Bilayer Graphene.” In: *2D Materials* 12.3 (May 2025), p. 035009. doi: [10.1088/2053-1583/add74a](https://doi.org/10.1088/2053-1583/add74a) (cited on page 58).
- [52] David Tebbe et al. “Tailoring the Dielectric Screening in WS₂-Graphene Heterostructures.” In: *npi 2D Materials and Applications* 7.1 (Apr. 8, 2023), p. 29. doi: [10.1038/s41699-023-00394-0](https://doi.org/10.1038/s41699-023-00394-0) (cited on page 58).
- [53] David Tebbe et al. Unpublished. 2025 (cited on page 58).
- [54] Eike Icking. “Electrostatically Tunable Band Structure in Bernal-stacked Bilayer-Graphene-Based Heterostructures.” PhD thesis. Aachen: RWTH Aachen University, 2024 (cited on page 58).
- [55] Michael A. Nielsen and Isaac L. Chuang. *Quantum Computation and Quantum Information: 10th Anniversary Edition*. 10th ed. Cambridge University Press, 2011 (cited on pages 60, 107, 146, 149).
- [56] Christoph Simon. “Towards a Global Quantum Network.” In: *Nature Photonics* 11.11 (11 Nov. 2017), pp. 678–680. doi: [10.1038/s41566-017-0032-0](https://doi.org/10.1038/s41566-017-0032-0) (cited on page 60).
- [57] H. J. Kimble. “The Quantum Internet.” In: *Nature* 453.7198 (7198 June 2008), pp. 1023–1030. doi: [10.1038/nature07127](https://doi.org/10.1038/nature07127) (cited on page 60).
- [58] C H Bennett and G Brassard. “Quantum Cryptography: Public Key Distribution and Coin Tossing.” In: International Conference on Computers, Systems & Signal Processing. Vol. 1. Bangalore, India, Dec. 1984, pp. 175–179. doi: [10.1016/j.tcs.2014.05.025](https://doi.org/10.1016/j.tcs.2014.05.025) (cited on page 60).
- [59] Artur K. Ekert. “Quantum Cryptography Based on Bell’s Theorem.” In: *Physical Review Letters* 67.6 (Aug. 5, 1991), pp. 661–663. doi: [10.1103/PhysRevLett.67.661](https://doi.org/10.1103/PhysRevLett.67.661) (cited on page 60).
- [60] David Deutsch et al. “Quantum Privacy Amplification and the Security of Quantum Cryptography over Noisy Channels.” In: *Physical Review Letters* 77.13 (Sept. 23, 1996), pp. 2818–2821. doi: [10.1103/PhysRevLett.77.2818](https://doi.org/10.1103/PhysRevLett.77.2818) (cited on page 60).

- [61] Nicolas Gisin et al. “Quantum Cryptography.” In: *Reviews of Modern Physics* 74.1 (Mar. 8, 2002), pp. 145–195. doi: [10.1103/RevModPhys.74.145](https://doi.org/10.1103/RevModPhys.74.145) (cited on page 60).
- [62] Anqi Huang et al. “Implementation Vulnerabilities in General Quantum Cryptography.” In: *New Journal of Physics* 20.10 (Oct. 2018), p. 103016. doi: [10.1088/1367-2630/aade06](https://doi.org/10.1088/1367-2630/aade06) (cited on page 60).
- [63] Xiao-Ling Pang et al. “Hacking Quantum Key Distribution via Injection Locking.” In: *Physical Review Applied* 13.3 (Mar. 3, 2020), p. 034008. doi: [10.1103/PhysRevApplied.13.034008](https://doi.org/10.1103/PhysRevApplied.13.034008) (cited on page 60).
- [64] J. I. Cirac et al. “Distributed Quantum Computation over Noisy Channels.” In: *Physical Review A* 59.6 (June 1, 1999), pp. 4249–4254. doi: [10.1103/PhysRevA.59.4249](https://doi.org/10.1103/PhysRevA.59.4249) (cited on page 60).
- [65] Hugo Jacinto, Élie Gouzien, and Nicolas Sangouard. *Network Requirements for Distributed Quantum Computation*. Apr. 11, 2025. doi: [10.48550/arXiv.2504.08891](https://doi.org/10.48550/arXiv.2504.08891). Pre-published (cited on page 60).
- [66] D. Main et al. “Distributed Quantum Computing across an Optical Network Link.” In: *Nature* 638.8050 (Feb. 2025), pp. 383–388. doi: [10.1038/s41586-024-08404-x](https://doi.org/10.1038/s41586-024-08404-x) (cited on page 60).
- [67] A.M. Childs. “Secure Assisted Quantum Computation.” In: *Quantum Information and Computation* 5.6 (Sept. 2005), pp. 456–466. doi: [10.26421/QIC5.6-4](https://doi.org/10.26421/QIC5.6-4) (cited on page 60).
- [68] Vittorio Giovannetti et al. “Efficient Universal Blind Quantum Computation.” In: *Physical Review Letters* 111.23 (Dec. 3, 2013), p. 230501. doi: [10.1103/PhysRevLett.111.230501](https://doi.org/10.1103/PhysRevLett.111.230501) (cited on page 60).
- [69] Y.-C. Wei et al. “Universal Distributed Blind Quantum Computing with Solid-State Qubits.” In: *Science* 388.6746 (May 2025), pp. 509–513. doi: [10.1126/science.adu6894](https://doi.org/10.1126/science.adu6894) (cited on page 60).
- [70] Zachary Eldredge et al. “Optimal and Secure Measurement Protocols for Quantum Sensor Networks.” In: *Physical Review A* 97.4 (Apr. 23, 2018), p. 042337. doi: [10.1103/PhysRevA.97.042337](https://doi.org/10.1103/PhysRevA.97.042337) (cited on page 60).
- [71] Vittorio Giovannetti, Seth Lloyd, and Lorenzo Maccone. “Quantum-Enhanced Measurements: Beating the Standard Quantum Limit.” In: *Science* 306.5700 (Nov. 19, 2004), pp. 1330–1336. doi: [10.1126/science.1104149](https://doi.org/10.1126/science.1104149) (cited on page 60).
- [72] Daniel Gottesman, Thomas Jennewein, and Sarah Croke. “Longer-Baseline Telescopes Using Quantum Repeaters.” In: *Physical Review Letters* 109.7 (Aug. 16, 2012), p. 070503. doi: [10.1103/PhysRevLett.109.070503](https://doi.org/10.1103/PhysRevLett.109.070503) (cited on page 60).
- [73] E. T. Khabiboulline et al. “Optical Interferometry with Quantum Networks.” In: *Physical Review Letters* 123.7 (Aug. 15, 2019), p. 070504. doi: [10.1103/PhysRevLett.123.070504](https://doi.org/10.1103/PhysRevLett.123.070504) (cited on page 60).
- [74] The Event Horizon Telescope Collaboration et al. “First M87 Event Horizon Telescope Results. IV. Imaging the Central Supermassive Black Hole.” In: *The Astrophysical Journal Letters* 875.1 (Apr. 2019), p. L4. doi: [10.3847/2041-8213/ab0e85](https://doi.org/10.3847/2041-8213/ab0e85) (cited on page 60).
- [75] P. Kómár et al. “A Quantum Network of Clocks.” In: *Nature Physics* 10.8 (Aug. 2014), pp. 582–587. doi: [10.1038/nphys3000](https://doi.org/10.1038/nphys3000) (cited on page 60).
- [76] Steven Weinberg. “Testing Quantum Mechanics.” In: *Annals of Physics* 194.2 (Sept. 1, 1989), pp. 336–386. doi: [10.1016/0003-4916\(89\)90276-5](https://doi.org/10.1016/0003-4916(89)90276-5) (cited on page 60).
- [77] A. Einstein, B. Podolsky, and N. Rosen. “Can Quantum-Mechanical Description of Physical Reality Be Considered Complete?” In: *Physical Review* 47.10 (May 15, 1935), pp. 777–780. doi: [10.1103/PhysRev.47.777](https://doi.org/10.1103/PhysRev.47.777) (cited on page 60).
- [78] J. S. Bell. “On the Einstein Podolsky Rosen Paradox.” In: *Physics Physique Fizika* 1.3 (Nov. 1, 1964), pp. 195–200. doi: [10.1103/PhysicsPhysiqueFizika.1.195](https://doi.org/10.1103/PhysicsPhysiqueFizika.1.195) (cited on page 60).
- [79] John F. Clauser et al. “Proposed Experiment to Test Local Hidden-Variable Theories.” In: *Physical Review Letters* 23.15 (Oct. 13, 1969), pp. 880–884. doi: [10.1103/PhysRevLett.23.880](https://doi.org/10.1103/PhysRevLett.23.880) (cited on page 60).
- [80] B. Hensen et al. “Loophole-Free Bell Inequality Violation Using Electron Spins Separated by 1.3 Kilometres.” In: *Nature* 526.7575 (Oct. 2015), pp. 682–686. doi: [10.1038/nature15759](https://doi.org/10.1038/nature15759) (cited on page 60).
- [81] Simon Storz et al. “Loophole-Free Bell Inequality Violation with Superconducting Circuits.” In: *Nature* 617.7960 (May 2023), pp. 265–270. doi: [10.1038/s41586-023-05885-0](https://doi.org/10.1038/s41586-023-05885-0) (cited on page 60).
- [82] Zheng-Da Li et al. “Testing Real Quantum Theory in an Optical Quantum Network.” In: *Physical Review Letters* 128.4 (Jan. 24, 2022), p. 040402. doi: [10.1103/PhysRevLett.128.040402](https://doi.org/10.1103/PhysRevLett.128.040402) (cited on page 61).

- [83] Peter Shadbolt et al. “Testing Foundations of Quantum Mechanics with Photons.” In: *Nature Physics* 10.4 (Apr. 2014), pp. 278–286. DOI: [10.1038/nphys2931](https://doi.org/10.1038/nphys2931) (cited on page 61).
- [84] C. M. Knaut et al. “Entanglement of Nanophotonic Quantum Memory Nodes in a Telecom Network.” In: *Nature* 629.8012 (May 2024), pp. 573–578. DOI: [10.1038/s41586-024-07252-z](https://doi.org/10.1038/s41586-024-07252-z) (cited on page 61).
- [85] Jian-Long Liu et al. “Creation of Memory–Memory Entanglement in a Metropolitan Quantum Network.” In: *Nature* 629.8012 (May 2024), pp. 579–585. DOI: [10.1038/s41586-024-07308-0](https://doi.org/10.1038/s41586-024-07308-0) (cited on page 61).
- [86] Stephan Kucera et al. “Demonstration of Quantum Network Protocols over a 14-Km Urban Fiber Link.” In: *npj Quantum Information* 10.1 (Sept. 14, 2024), p. 88. DOI: [10.1038/s41534-024-00886-x](https://doi.org/10.1038/s41534-024-00886-x) (cited on page 61).
- [87] Arian J. Stolk et al. “Metropolitan-Scale Heralded Entanglement of Solid-State Qubits.” In: *Science Advances* 10.44 (Oct. 30, 2024), eadp6442. DOI: [10.1126/sciadv.adp6442](https://doi.org/10.1126/sciadv.adp6442) (cited on page 61).
- [88] Johannes Nokkala, Jyrki Piilo, and Ginestra Bianconi. “Complex Quantum Networks: A Topical Review.” In: *Journal of Physics A: Mathematical and Theoretical* 57.23 (June 7, 2024), p. 233001. DOI: [10.1088/1751-8121/ad41a6](https://doi.org/10.1088/1751-8121/ad41a6) (cited on page 61).
- [89] Lucien Hardy. “Quantum Gravity Computers: On the Theory of Computation with Indefinite Causal Structure.” In: *Quantum Reality, Relativistic Causality, and Closing the Epistemic Circle: Essays in Honour of Abner Shimony*. Ed. by Wayne C. Myrvold and Joy Christian. Dordrecht: Springer Netherlands, 2009, pp. 379–401. DOI: [10.1007/978-1-4020-9107-0_21](https://doi.org/10.1007/978-1-4020-9107-0_21) (cited on page 61).
- [90] K. Goswami et al. “Increasing Communication Capacity via Superposition of Order.” In: *Physical Review Research* 2.3 (Aug. 24, 2020), p. 033292. DOI: [10.1103/PhysRevResearch.2.033292](https://doi.org/10.1103/PhysRevResearch.2.033292) (cited on page 61).
- [91] Lee A. Rozema et al. “Experimental Aspects of Indefinite Causal Order in Quantum Mechanics.” In: *Nature Reviews Physics* 6.8 (Aug. 2024), pp. 483–499. DOI: [10.1038/s42254-024-00739-8](https://doi.org/10.1038/s42254-024-00739-8) (cited on page 61).
- [92] W. K. Wootters and W. H. Zurek. “A Single Quantum Cannot Be Cloned.” In: *Nature* 299.5886 (5886 Oct. 1982), pp. 802–803. DOI: [10.1038/299802a0](https://doi.org/10.1038/299802a0) (cited on page 61).
- [93] D. Dieks. “Communication by EPR Devices.” In: *Physics Letters A* 92.6 (Nov. 22, 1982), pp. 271–272. DOI: [10.1016/0375-9601\(82\)90084-6](https://doi.org/10.1016/0375-9601(82)90084-6) (cited on page 61).
- [94] M. Żukowski et al. “Event-ready-detectors” Bell Experiment via Entanglement Swapping.” In: *Physical Review Letters* 71.26 (Dec. 27, 1993), pp. 4287–4290. DOI: [10.1103/PhysRevLett.71.4287](https://doi.org/10.1103/PhysRevLett.71.4287) (cited on page 61).
- [95] Jian-Wei Pan et al. “Experimental Entanglement Swapping: Entangling Photons That Never Interacted.” In: *Physical Review Letters* 80.18 (May 4, 1998), pp. 3891–3894. DOI: [10.1103/PhysRevLett.80.3891](https://doi.org/10.1103/PhysRevLett.80.3891) (cited on page 61).
- [96] H.-J. Briegel et al. “Quantum Repeaters: The Role of Imperfect Local Operations in Quantum Communication.” In: *Physical Review Letters* 81.26 (Dec. 28, 1998), pp. 5932–5935. DOI: [10.1103/PhysRevLett.81.5932](https://doi.org/10.1103/PhysRevLett.81.5932) (cited on page 61).
- [97] W. Dür et al. “Quantum Repeaters Based on Entanglement Purification.” In: *Physical Review A* 59.1 (Jan. 1, 1999), pp. 169–181. DOI: [10.1103/PhysRevA.59.169](https://doi.org/10.1103/PhysRevA.59.169) (cited on page 61).
- [98] W. Dür and H. J. Briegel. “Entanglement Purification and Quantum Error Correction.” In: *Reports on Progress in Physics* 70.8 (July 2007), p. 1381. DOI: [10.1088/0034-4885/70/8/R03](https://doi.org/10.1088/0034-4885/70/8/R03) (cited on page 61).
- [99] Veysel Bayrakci and Fatih Ozaydin. “Quantum Zeno Repeaters.” In: *Scientific Reports* 12.1 (1 Sept. 12, 2022), p. 15302. DOI: [10.1038/s41598-022-19170-z](https://doi.org/10.1038/s41598-022-19170-z) (cited on page 61).
- [100] V. Krutyanskiy et al. “Telecom-Wavelength Quantum Repeater Node Based on a Trapped-Ion Processor.” In: *Physical Review Letters* 130.21 (May 22, 2023), p. 213601. DOI: [10.1103/PhysRevLett.130.213601](https://doi.org/10.1103/PhysRevLett.130.213601) (cited on page 61).
- [101] Zheng-Da Li et al. “Experimental Quantum Repeater without Quantum Memory.” In: *Nature Photonics* 13.9 (9 Sept. 2019), pp. 644–648. DOI: [10.1038/s41566-019-0468-5](https://doi.org/10.1038/s41566-019-0468-5) (cited on page 61).
- [102] Hans K.C. Beukers et al. “Remote-Entanglement Protocols for Stationary Qubits with Photonic Interfaces.” In: *PRX Quantum* 5.1 (Mar. 29, 2024), p. 010202. DOI: [10.1103/PRXQuantum.5.010202](https://doi.org/10.1103/PRXQuantum.5.010202) (cited on page 61).

- [103] Nicolas Sangouard et al. “Quantum Repeaters Based on Atomic Ensembles and Linear Optics.” In: *Reviews of Modern Physics* 83.1 (Mar. 21, 2011), pp. 33–80. DOI: [10.1103/RevModPhys.83.33](https://doi.org/10.1103/RevModPhys.83.33) (cited on page 61).
- [104] Jacob P. Covey, Harald Weinfurter, and Hannes Bernien. “Quantum Networks with Neutral Atom Processing Nodes.” In: *npj Quantum Information* 9.1 (Sept. 16, 2023), p. 90. DOI: [10.1038/s41534-023-00759-9](https://doi.org/10.1038/s41534-023-00759-9) (cited on page 61).
- [105] E. Togan et al. “Quantum Entanglement between an Optical Photon and a Solid-State Spin Qubit.” In: *Nature* 466.7307 (7307 Aug. 2010), pp. 730–734. DOI: [10.1038/nature09256](https://doi.org/10.1038/nature09256) (cited on page 61).
- [106] C. T. Nguyen et al. “Quantum Network Nodes Based on Diamond Qubits with an Efficient Nanophotonic Interface.” In: *Physical Review Letters* 123.18 (Oct. 30, 2019), p. 183602. DOI: [10.1103/PhysRevLett.123.183602](https://doi.org/10.1103/PhysRevLett.123.183602). arXiv: [1907.13199](https://arxiv.org/abs/1907.13199) (cited on page 61).
- [107] L. Bergeron et al. “Silicon-Integrated Telecommunications Photon-Spin Interface.” In: *PRX Quantum* 1.2 (Oct. 2, 2020), p. 020301. DOI: [10.1103/PRXQuantum.1.020301](https://doi.org/10.1103/PRXQuantum.1.020301) (cited on page 61).
- [108] Mohammad Mirhosseini et al. “Superconducting Qubit to Optical Photon Transduction.” In: *Nature* 588.7839 (Dec. 2020), pp. 599–603. DOI: [10.1038/s41586-020-3038-6](https://doi.org/10.1038/s41586-020-3038-6) (cited on page 61).
- [109] Changqing Wang et al. “High-Efficiency Microwave-Optical Quantum Transduction Based on a Cavity Electro-Optic Superconducting System with Long Coherence Time.” In: *npj Quantum Information* 8.1 (Dec. 21, 2022), p. 149. DOI: [10.1038/s41534-022-00664-7](https://doi.org/10.1038/s41534-022-00664-7) (cited on page 61).
- [110] I. N. Stranski and L. Krastanow. “Zur Theorie der orientierten Ausscheidung von Ionenkristallen aufeinander.” In: *Monatshefte für Chemie und verwandte Teile anderer Wissenschaften* 71.1 (Dec. 1, 1937), pp. 351–364. DOI: [10.1007/BF01798103](https://doi.org/10.1007/BF01798103) (cited on page 62).
- [111] Nobuyuki Koguchi, Satoshi Takahashi, and Toyohiro Chikyow. “New MBE Growth Method for InSb Quantum Well Boxes.” In: *Journal of Crystal Growth* 111.1 (May 2, 1991), pp. 688–692. DOI: [10.1016/0022-0248\(91\)91064-H](https://doi.org/10.1016/0022-0248(91)91064-H) (cited on page 62).
- [112] Nobuyuki Koguchi, Keiko Ishige, and Satoshi Takahashi. “New Selective Molecular-beam Epitaxial Growth Method for Direct Formation of GaAs Quantum Dots.” In: *Journal of Vacuum Science & Technology B: Microelectronics and Nanometer Structures Processing, Measurement, and Phenomena* 11.3 (May 1, 1993), pp. 787–790. DOI: [10.1116/1.586789](https://doi.org/10.1116/1.586789) (cited on page 62).
- [113] Nobuyuki Koguchi Nobuyuki Koguchi and Keiko Ishige Keiko Ishige. “Growth of GaAs Epitaxial Microcrystals on an S-Terminated GaAs Substrate by Successive Irradiation of Ga and As Molecular Beams.” In: *Japanese Journal of Applied Physics* 32 (5R May 1, 1993), p. 2052. DOI: [10.1143/JJAP.32.2052](https://doi.org/10.1143/JJAP.32.2052) (cited on page 62).
- [114] Richard J. Warburton. “Single Spins in Self-Assembled Quantum Dots.” In: *Nature Materials* 12.6 (June 2013), pp. 483–493. DOI: [10.1038/nmat3585](https://doi.org/10.1038/nmat3585) (cited on page 62).
- [115] Guido Burkard et al. “Semiconductor Spin Qubits.” In: *Reviews of Modern Physics* 95.2 (June 14, 2023), p. 025003. DOI: [10.1103/RevModPhys.95.025003](https://doi.org/10.1103/RevModPhys.95.025003) (cited on page 62).
- [116] Peter Stano and Daniel Loss. *Review of Performance Metrics of Spin Qubits in Gated Semiconducting Nanostructures*. Mar. 24, 2025. DOI: [10.48550/arXiv.2107.06485](https://doi.org/10.48550/arXiv.2107.06485). Pre-published (cited on page 62).
- [117] Benjamin Jöcker et al. “Transfer of a Quantum State from a Photonic Qubit to a Gate-Defined Quantum Dot.” In: *Physical Review B* 99.20 (May 13, 2019), p. 205415. DOI: [10.1103/PhysRevB.99.205415](https://doi.org/10.1103/PhysRevB.99.205415) (cited on page 62).
- [118] Thomas Descamps et al. “Semiconductor Membranes for Electrostatic Exciton Trapping in Optically Addressable Quantum Transport Devices.” In: *Physical Review Applied* 19.4 (Apr. 28, 2023), p. 044095. DOI: [10.1103/PhysRevApplied.19.044095](https://doi.org/10.1103/PhysRevApplied.19.044095) (cited on page 62).
- [119] G. D. Mahan. “Excitons in Degenerate Semiconductors.” In: *Physical Review* 153.3 (Jan. 15, 1967), pp. 882–889. DOI: [10.1103/PhysRev.153.882](https://doi.org/10.1103/PhysRev.153.882) (cited on page 98).
- [120] Maarten Baeten and Michiel Wouters. “Many-Body Effects of a Two-Dimensional Electron Gas on Trion-Polaritons.” In: *Physical Review B* 91.11 (Mar. 23, 2015), p. 115313. DOI: [10.1103/PhysRevB.91.115313](https://doi.org/10.1103/PhysRevB.91.115313) (cited on page 100).
- [121] M. M. Glazov. “Optical Properties of Charged Excitons in Two-Dimensional Semiconductors.” In: *The Journal of Chemical Physics* 153.3 (July 21, 2020), p. 034703. DOI: [10.1063/5.0012475](https://doi.org/10.1063/5.0012475) (cited on page 100).

- [122] Di Huang et al. “Quantum Dynamics of Attractive and Repulsive Polarons in a Doped MoSe₂ Monolayer.” In: *Physical Review X* 13.1 (Mar. 2, 2023), p. 011029. doi: [10.1103/PhysRevX.13.011029](https://doi.org/10.1103/PhysRevX.13.011029) (cited on page 100).
- [123] Tobias Hangleiter, Pascal Cerfontaine, and Hendrik Bluhm. “Filter-Function Formalism and Software Package to Compute Quantum Processes of Gate Sequences for Classical Non-Markovian Noise.” In: *Physical Review Research* 3.4 (Oct. 18, 2021), p. 043047. doi: [10.1103/PhysRevResearch.3.043047](https://doi.org/10.1103/PhysRevResearch.3.043047) (cited on pages 103, 173).
- [124] Pascal Cerfontaine, Tobias Hangleiter, and Hendrik Bluhm. “Filter Functions for Quantum Processes under Correlated Noise.” In: *Physical Review Letters* 127.17 (Oct. 18, 2021), p. 170403. doi: [10.1103/PhysRevLett.127.170403](https://doi.org/10.1103/PhysRevLett.127.170403) (cited on pages 103–105, 108, 111, 113–116, 147, 148, 150).
- [125] Pascal Cerfontaine. “High-Fidelity Single- and Two-Qubit Gates for Two-Electron Spin Qubits.” RWTH Aachen University, 2019 (cited on page 103).
- [126] Ryogo Kubo. “Generalized Cumulant Expansion Method.” In: *Journal of the Physical Society of Japan* 17.7 (July 1962), pp. 1100–1120. doi: [10.1143/JPSJ.17.1100](https://doi.org/10.1143/JPSJ.17.1100) (cited on pages 103, 104, 108, 110, 128).
- [127] Ronald Forrest Fox. “Critique of the Generalized Cumulant Expansion Method.” In: *Journal of Mathematical Physics* 17.7 (July 1, 1976), pp. 1148–1153. doi: [10.1063/1.523041](https://doi.org/10.1063/1.523041) (cited on pages 103, 104, 128, 131).
- [128] Tobias Hangleiter, Pascal Cerfontaine, and Hendrik Bluhm. “Erratum: Filter-function Formalism and Software Package to Compute Quantum Processes of Gate Sequences for Classical Non-Markovian Noise [Phys. Rev. Research 3, 043047 (2021)].” In: *Physical Review Research* 6.4 (Oct. 16, 2024), p. 049001. doi: [10.1103/PhysRevResearch.6.049001](https://doi.org/10.1103/PhysRevResearch.6.049001) (cited on page 103).
- [129] Leigh M. Norris, Gerardo A. Paz-Silva, and Lorenza Viola. “Qubit Noise Spectroscopy for Non-Gaussian Dephasing Environments.” In: *Physical Review Letters* 116.15 (Apr. 14, 2016), p. 150503. doi: [10.1103/PhysRevLett.116.150503](https://doi.org/10.1103/PhysRevLett.116.150503) (cited on pages 103, 114).
- [130] David P. DiVincenzo. “Two-Bit Gates Are Universal for Quantum Computation.” In: *Physical Review A* 51.2 (Feb. 1, 1995), pp. 1015–1022. doi: [10.1103/PhysRevA.51.1015](https://doi.org/10.1103/PhysRevA.51.1015) (cited on page 103).
- [131] Vittorio Gorini, Andrzej Kossakowski, and E. C. G. Sudarshan. “Completely Positive Dynamical Semigroups of N-level Systems.” In: *Journal of Mathematical Physics* 17.5 (1976), p. 821. doi: [10.1063/1.522979](https://doi.org/10.1063/1.522979) (cited on pages 103, 173).
- [132] G. Lindblad. “On the Generators of Quantum Dynamical Semigroups.” In: *Communications in Mathematical Physics* 48.2 (June 1976), pp. 119–130. doi: [10.1007/BF01608499](https://doi.org/10.1007/BF01608499) (cited on pages 103, 173).
- [133] M. Brownnutt et al. “Ion-Trap Measurements of Electric-Field Noise near Surfaces.” In: *Reviews of Modern Physics* 87.4 (Dec. 2015), pp. 1419–1482. doi: [10.1103/RevModPhys.87.1419](https://doi.org/10.1103/RevModPhys.87.1419) (cited on page 103).
- [134] Santosh Kumar et al. “Resonant Laser Spectroscopy of Localized Excitons in Monolayer WSe₂.” In: *Optica* 3.8 (Aug. 20, 2016), p. 882. doi: [10.1364/OPTICA.3.000882](https://doi.org/10.1364/OPTICA.3.000882) (cited on page 103).
- [135] Jun Yoneda et al. “A Quantum-Dot Spin Qubit with Coherence Limited by Charge Noise and Fidelity Higher than 99.9%.” In: *Nature Nanotechnology* 13.2 (Feb. 2018), pp. 102–106. doi: [10.1038/s41565-017-0014-x](https://doi.org/10.1038/s41565-017-0014-x) (cited on pages 103, 104, 119).
- [136] E. Paladino et al. “1/f Noise: Implications for Solid-State Quantum Information.” In: *Reviews of Modern Physics* 86.2 (Apr. 3, 2014), pp. 361–418. doi: [10.1103/RevModPhys.86.361](https://doi.org/10.1103/RevModPhys.86.361) (cited on page 103).
- [137] Elliot J. Connors et al. “Charge-Noise Spectroscopy of Si/SiGe Quantum Dots via Dynamically-Decoupled Exchange Oscillations.” In: *Nature Communications* 13.1 (Dec. 2022), p. 940. doi: [10.1038/s41467-022-28519-x](https://doi.org/10.1038/s41467-022-28519-x) (cited on page 103).
- [138] Hui Khoon Ng and John Preskill. “Fault-Tolerant Quantum Computation versus Gaussian Noise.” In: *Physical Review A* 79.3 (Mar. 16, 2009), p. 032318. doi: [10.1103/PhysRevA.79.032318](https://doi.org/10.1103/PhysRevA.79.032318). arXiv: [0810.4953](https://arxiv.org/abs/0810.4953) (cited on page 103).
- [139] M. Veldhorst et al. “An Addressable Quantum Dot Qubit with Fault-Tolerant Control-Fidelity.” In: *Nature Nanotechnology* 9.12 (Dec. 2014), pp. 981–985. doi: [10.1038/nnano.2014.216](https://doi.org/10.1038/nnano.2014.216) (cited on pages 104, 119, 140).
- [140] S. Debnath et al. “Demonstration of a Small Programmable Quantum Computer with Atomic Qubits.” In: *Nature* 536.7614 (Aug. 4, 2016), pp. 63–66. doi: [10.1038/nature18648](https://doi.org/10.1038/nature18648) (cited on page 104).

- [141] O. E. Dial et al. “Charge Noise Spectroscopy Using Coherent Exchange Oscillations in a Singlet-Triplet Qubit.” In: *Physical Review Letters* 110.14 (Apr. 5, 2013), p. 146804. doi: [10.1103/PhysRevLett.110.146804](https://doi.org/10.1103/PhysRevLett.110.146804) (cited on pages 104, 140).
- [142] C. M. Quintana et al. “Observation of Classical-Quantum Crossover of $1/f$ Flux Noise and Its Paramagnetic Temperature Dependence.” In: *Physical Review Letters* 118.5 (Jan. 31, 2017), p. 057702. doi: [10.1103/PhysRevLett.118.057702](https://doi.org/10.1103/PhysRevLett.118.057702) (cited on page 104).
- [143] Filip K. Malinowski et al. “Spectrum of the Nuclear Environment for GaAs Spin Qubits.” In: *Physical Review Letters* 118.17 (Apr. 28, 2017), p. 177702. doi: [10.1103/PhysRevLett.118.177702](https://doi.org/10.1103/PhysRevLett.118.177702) (cited on page 104).
- [144] R. Barends et al. “Superconducting Quantum Circuits at the Surface Code Threshold for Fault Tolerance.” In: *Nature* 508.7497 (Apr. 2014), pp. 500–503. doi: [10.1038/nature13171](https://doi.org/10.1038/nature13171) (cited on pages 104, 140).
- [145] Robin Blume-Kohout et al. “Demonstration of Qubit Operations below a Rigorous Fault Tolerance Threshold with Gate Set Tomography.” In: *Nature Communications* 8.1 (Apr. 28, 2017), p. 14485. doi: [10.1038/ncomms14485](https://doi.org/10.1038/ncomms14485) (cited on page 104).
- [146] Kaveh Khodjasteh and Lorenza Viola. “Dynamically Error-Corrected Gates for Universal Quantum Computation.” In: *Physical Review Letters* 102.8 (Feb. 26, 2009), p. 080501. doi: [10.1103/PhysRevLett.102.080501](https://doi.org/10.1103/PhysRevLett.102.080501). arXiv: [0810.0698](https://arxiv.org/abs/0810.0698) (cited on pages 104, 108).
- [147] A. G. Kofman and G. Kurizki. “Universal Dynamical Control of Quantum Mechanical Decay: Modulation of the Coupling to the Continuum.” In: *Physical Review Letters* 87.27 (Dec. 12, 2001), p. 270405. doi: [10.1103/PhysRevLett.87.270405](https://doi.org/10.1103/PhysRevLett.87.270405) (cited on pages 104, 149).
- [148] John M. Martinis et al. “Decoherence of a Superconducting Qubit Due to Bias Noise.” In: *Physical Review B* 67.9 (Mar. 25, 2003), p. 094510. doi: [10.1103/PhysRevB.67.094510](https://doi.org/10.1103/PhysRevB.67.094510) (cited on pages 104, 149).
- [149] Götz S. Uhrig. “Keeping a Quantum Bit Alive by Optimized π -Pulse Sequences.” In: *Physical Review Letters* 98.10 (Mar. 9, 2007), p. 100504. doi: [10.1103/PhysRevLett.98.100504](https://doi.org/10.1103/PhysRevLett.98.100504) (cited on pages 104, 149).
- [150] Łukasz Cywiński et al. “How to Enhance Dephasing Time in Superconducting Qubits.” In: *Physical Review B* 77.17 (May 13, 2008), p. 174509. doi: [10.1103/PhysRevB.77.174509](https://doi.org/10.1103/PhysRevB.77.174509) (cited on pages 104, 108, 116, 163).
- [151] Gonzalo A. Álvarez and Dieter Suter. “Measuring the Spectrum of Colored Noise by Dynamical Decoupling.” In: *Physical Review Letters* 107.23 (Nov. 30, 2011), p. 230501. doi: [10.1103/PhysRevLett.107.230501](https://doi.org/10.1103/PhysRevLett.107.230501) (cited on page 104).
- [152] Jonas Bylander et al. “Noise Spectroscopy through Dynamical Decoupling with a Superconducting Flux Qubit.” In: *Nature Physics* 7.7 (July 2011), pp. 565–570. doi: [10.1038/nphys1994](https://doi.org/10.1038/nphys1994) (cited on page 104).
- [153] Gerardo A. Paz-Silva, Leigh M. Norris, and Lorenza Viola. “Multiqubit Spectroscopy of Gaussian Quantum Noise.” In: *Physical Review A* 95.2 (Feb. 23, 2017), p. 022121. doi: [10.1103/PhysRevA.95.022121](https://doi.org/10.1103/PhysRevA.95.022121) (cited on pages 104, 149).
- [154] Michael J. Biercuk et al. “Optimized Dynamical Decoupling in a Model Quantum Memory.” In: *Nature* 458.7241 (Apr. 23, 2009), pp. 996–1000. doi: [10.1038/nature07951](https://doi.org/10.1038/nature07951) (cited on page 104).
- [155] Hermann Uys, Michael Biercuk, and John Bollinger. “Optimized Noise Filtration through Dynamical Decoupling.” In: *Physical Review Letters* 103.4 (July 20, 2009), p. 040501. doi: [10.1103/PhysRevLett.103.040501](https://doi.org/10.1103/PhysRevLett.103.040501) (cited on page 104).
- [156] A. Soare et al. “Experimental Noise Filtering by Quantum Control.” In: *Nature Physics* 10.11 (Nov. 19, 2014), pp. 825–829. doi: [10.1038/nphys3115](https://doi.org/10.1038/nphys3115) (cited on pages 104, 140, 141).
- [157] Todd Green, Hermann Uys, and Michael J. Biercuk. “High-Order Noise Filtering in Nontrivial Quantum Logic Gates.” In: *Physical Review Letters* 109.2 (July 9, 2012), p. 020501. doi: [10.1103/PhysRevLett.109.020501](https://doi.org/10.1103/PhysRevLett.109.020501) (cited on pages 104, 114, 116, 120).
- [158] Todd J. Green et al. “Arbitrary Quantum Control of Qubits in the Presence of Universal Noise.” In: *New Journal of Physics* 15.9 (Sept. 12, 2013), p. 095004. doi: [10.1088/1367-2630/15/9/095004](https://doi.org/10.1088/1367-2630/15/9/095004). arXiv: [1211.1163](https://arxiv.org/abs/1211.1163) (cited on pages 104, 105, 110–114, 116, 165, 167).

- [159] Utkan Güngördü and J. P. Kestner. “Pulse Sequence Designed for Robust C-phase Gates in SiMOS and Si/SiGe Double Quantum Dots.” In: *Physical Review B* 98.16 (Oct. 1, 2018), p. 165301. doi: [10.1103/PhysRevB.98.165301](#) (cited on pages 104, 109, 116).
- [160] Harrison Ball et al. *Software Tools for Quantum Control: Improving Quantum Computer Performance through Noise and Error Suppression*. July 9, 2020. doi: [10.48550/arXiv.2001.04060](#). Pre-published (cited on page 104).
- [161] Wilhelm Magnus. “On the Exponential Solution of Differential Equations for a Linear Operator.” In: *Communications on Pure and Applied Mathematics* 7.4 (Nov. 1954), pp. 649–673. doi: [10.1002/cpa.3160070404](#) (cited on pages 104, 110).
- [162] S. Blanes et al. “The Magnus Expansion and Some of Its Applications.” In: *Physics Reports* 470.5–6 (Jan. 2009), pp. 151–238. doi: [10.1016/j.physrep.2008.11.001](#) (cited on pages 104, 110).
- [163] Gerardo A Paz-Silva and Lorenza Viola. “General Transfer-Function Approach to Noise Filtering in Open-Loop Quantum Control.” In: *Physical Review Letters* 113.25 (Dec. 19, 2014), p. 250501. doi: [10.1103/PhysRevLett.113.250501](#) (cited on pages 104, 108).
- [164] Jens Clausen, Guy Bensky, and Gershon Kurizki. “Bath-Optimized Minimal-Energy Protection of Quantum Operations from Decoherence.” In: *Physical Review Letters* 104.4 (Jan. 25, 2010), p. 040401. doi: [10.1103/PhysRevLett.104.040401](#) (cited on pages 104, 112).
- [165] Chingiz Kabytayev et al. “Robustness of Composite Pulses to Time-Dependent Control Noise.” In: *Physical Review A - Atomic, Molecular, and Optical Physics* 90.1 (July 14, 2014), p. 012316. doi: [10.1103/PhysRevA.90.012316](#) (cited on page 104).
- [166] Harrison Ball et al. “Effect of Noise Correlations on Randomized Benchmarking.” In: *Physical Review A* 93.2 (Feb. 1, 2016), p. 022303. doi: [10.1103/PhysRevA.93.022303](#) (cited on pages 104, 144).
- [167] Jeroen P. G. van Dijk et al. “The Impact of Classical Control Electronics on Qubit Fidelity.” In: *Physical Review Applied* 12.4 (Oct. 24, 2019), p. 044054. doi: [10.1103/PhysRevApplied.12.044054](#). arXiv: [1803.06176](#) (cited on page 104).
- [168] Ryogo Kubo. “Stochastic Liouville Equations.” In: *Journal of Mathematical Physics* 4.2 (Feb. 1963), pp. 174–183. doi: [10.1063/1.1703941](#) (cited on pages 104, 108, 111, 128).
- [169] Marco Bianucci and Mauro Bologna. “About the Foundation of the Kubo Generalized Cumulants Theory. A Revisited and Corrected Approach.” In: *Journal of Statistical Mechanics: Theory and Experiment* 2020.4 (Apr. 1, 2020), p. 043405. doi: [10.1088/1742-5468/ab7755](#). arXiv: [1911.09620 \[math-ph, stat\]](#) (cited on pages 104, 128).
- [170] Tobias Hangleiter, Isabel Nha Minh Le, and Julian D. Teske, *Filter_functions* version v1.1.3, May 14, 2024. Zenodo. doi: [10.5281/ZENODO.4575000](#), (cited on pages 105, 134, 150).
- [171] J. R. Johansson, P. D. Nation, and Franco Nori. “QuTiP: An Open-Source Python Framework for the Dynamics of Open Quantum Systems.” In: *Computer Physics Communications* 183.8 (Aug. 1, 2012), pp. 1760–1772. doi: [10.1016/j.cpc.2012.02.021](#) (cited on pages 105, 134, 146, 165).
- [172] Julian David Teske, Pascal Cerfontaine, and Hendrik Bluhm. “Qopt: An Experiment-Oriented Software Package for Qubit Simulation and Quantum Optimal Control.” In: *Physical Review Applied* 17.3 (Mar. 14, 2022), p. 034036. doi: [10.1103/PhysRevApplied.17.034036](#) (cited on pages 105, 134, 136, 150).
- [173] Karl Kraus et al., eds. *States, Effects, and Operations Fundamental Notions of Quantum Theory*. Vol. 190. Berlin, Heidelberg: Springer Berlin Heidelberg, 1983 (cited on page 107).
- [174] Isaac L. Chuang and M. A. Nielsen. “Prescription for Experimental Determination of the Dynamics of a Quantum Black Box.” In: *Journal of Modern Optics* 44.11–12 (Nov. 1997), pp. 2455–2467. doi: [10.1080/095008349708231894](#) (cited on page 107).
- [175] J. F. Poyatos, J. I. Cirac, and P. Zoller. “Complete Characterization of a Quantum Process: The Two-Bit Quantum Gate.” In: *Physical Review Letters* 78.2 (Jan. 13, 1997), pp. 390–393. doi: [10.1103/PhysRevLett.78.390](#) (cited on page 107).
- [176] Robin Blume-Kohout et al. *Robust, Self-Consistent, Closed-Form Tomography of Quantum Logic Gates on a Trapped Ion Qubit*. Oct. 16, 2013. doi: [10.48550/arXiv.1310.4492](#). Pre-published (cited on page 107).

- [177] Daniel Greenbaum. *Introduction to Quantum Gate Set Tomography*. Sept. 9, 2015. DOI: [10.48550/arXiv.1509.02921](https://doi.org/10.48550/arXiv.1509.02921). Pre-published (cited on pages 107, 112, 120).
- [178] Easwar Magesan, J. M. Gambetta, and Joseph Emerson. “Scalable and Robust Randomized Benchmarking of Quantum Processes.” In: *Physical Review Letters* 106.18 (May 6, 2011), p. 180504. DOI: [10.1103/PhysRevLett.106.180504](https://doi.org/10.1103/PhysRevLett.106.180504) (cited on pages 107, 143).
- [179] Shelby Kimmel et al. “Robust Extraction of Tomographic Information via Randomized Benchmarking.” In: *Physical Review X* 4.1 (Mar. 25, 2014), p. 011050. DOI: [10.1103/PhysRevX.4.011050](https://doi.org/10.1103/PhysRevX.4.011050) (cited on page 107).
- [180] Yoshihiro Nambu and Kazuo Nakamura. *On the Matrix Representation of Quantum Operations*. Apr. 12, 2005. DOI: [10.48550/arXiv.quant-ph/0504091](https://doi.org/10.48550/arXiv.quant-ph/0504091). Pre-published (cited on page 107).
- [181] U. Fano. “Description of States in Quantum Mechanics by Density Matrix and Operator Techniques.” In: *Reviews of Modern Physics* 29.1 (Jan. 1, 1957), pp. 74–93. DOI: [10.1103/RevModPhys.29.74](https://doi.org/10.1103/RevModPhys.29.74) (cited on page 107).
- [182] Yuan-Chi Yang, S. N. Coppersmith, and Mark Friesen. “Achieving High-Fidelity Single-Qubit Gates in a Strongly Driven Charge Qubit with 1/f Charge Noise.” In: *npj Quantum Information* 5.1 (Dec. 2019), p. 12. DOI: [10.1038/s41534-019-0127-1](https://doi.org/10.1038/s41534-019-0127-1) (cited on page 108).
- [183] P C Moan, J A Oteo, and J Ros. “On the Existence of the Exponential Solution of Linear Differential Systems.” In: *Journal of Physics A: Mathematical and General* 32.27 (1999), pp. 5133–5139. DOI: [10.1088/0305-4470/32/27/311](https://doi.org/10.1088/0305-4470/32/27/311) (cited on pages 110, 166).
- [184] Félix Beaudoin and W. A. Coish. “Microscopic Models for Charge-Noise-Induced Dephasing of Solid-State Qubits.” In: *Physical Review B* 91.16 (Apr. 29, 2015), p. 165432. DOI: [10.1103/PhysRevB.91.165432](https://doi.org/10.1103/PhysRevB.91.165432). arXiv: [1412.5536](https://arxiv.org/abs/1412.5536) (cited on page 110).
- [185] Kyle Willick, Daniel K. Park, and Jonathan Baugh. “Efficient Continuous-Wave Noise Spectroscopy beyond Weak Coupling.” In: *Physical Review A* 98.1 (July 18, 2018), p. 013414. DOI: [10.1103/PhysRevA.98.013414](https://doi.org/10.1103/PhysRevA.98.013414) (cited on page 110).
- [186] P Szańkowski et al. “Environmental Noise Spectroscopy with Qubits Subjected to Dynamical Decoupling.” In: *Journal of Physics: Condensed Matter* 29.33 (Aug. 23, 2017), p. 333001. DOI: [10.1088/1361-648X/aa7648](https://doi.org/10.1088/1361-648X/aa7648) (cited on page 111).
- [187] Pascal Cerfontaine, René Otten, and Hendrik Bluhm. “Self-Consistent Calibration of Quantum Gate Sets.” In: *Physical Review Applied* 13.4 (Apr. 28, 2020), p. 044071. DOI: [10.1103/PhysRevApplied.13.044071](https://doi.org/10.1103/PhysRevApplied.13.044071). arXiv: [1906.00950](https://arxiv.org/abs/1906.00950) (cited on page 111).
- [188] Shelby Kimmel, Guang Hao Low, and Theodore J. Yoder. “Robust Calibration of a Universal Single-Qubit Gate Set via Robust Phase Estimation.” In: *Physical Review A* 92.6 (Dec. 8, 2015), p. 062315. DOI: [10.1103/PhysRevA.92.062315](https://doi.org/10.1103/PhysRevA.92.062315) (cited on page 111).
- [189] Mark Byrd and Daniel Lidar. “Bang–Bang Operations from a Geometric Perspective.” In: *Quantum Information Processing* 1.1/2 (2002), pp. 19–34. DOI: [10.1023/A:1019697017584](https://doi.org/10.1023/A:1019697017584) (cited on page 112).
- [190] Daniel Loss and David P. DiVincenzo. “Quantum Computation with Quantum Dots.” In: *Physical Review A* 57.1 (Jan. 1, 1998), pp. 120–126. DOI: [10.1103/PhysRevA.57.120](https://doi.org/10.1103/PhysRevA.57.120) (cited on page 119).
- [191] T. D. Ladd et al. “Quantum Computers.” In: *Nature* 464.7285 (7285 Mar. 2010), pp. 45–53. DOI: [10.1038/nature08812](https://doi.org/10.1038/nature08812) (cited on page 119).
- [192] Jerry M. Chow et al. “Universal Quantum Gate Set Approaching Fault-Tolerant Thresholds with Superconducting Qubits.” In: *Physical Review Letters* 109.6 (Aug. 9, 2012), p. 060501. DOI: [10.1103/PhysRevLett.109.060501](https://doi.org/10.1103/PhysRevLett.109.060501) (cited on page 119).
- [193] Michał Horodecki, Paweł Horodecki, and Ryszard Horodecki. “General Teleportation Channel, Singlet Fraction, and Quasidistillation.” In: *Physical Review A* 60.3 (Sept. 1, 1999), pp. 1888–1898. DOI: [10.1103/PhysRevA.60.1888](https://doi.org/10.1103/PhysRevA.60.1888) (cited on pages 119, 140).
- [194] Michael A. Nielsen. “A Simple Formula for the Average Gate Fidelity of a Quantum Dynamical Operation.” In: *Physics Letters A* 303.4 (Oct. 7, 2002), pp. 249–252. DOI: [10.1016/S0375-9601\(02\)01272-0](https://doi.org/10.1016/S0375-9601(02)01272-0) (cited on pages 119, 140).
- [195] Joel J. Wallman and Steven T. Flammia. “Randomized Benchmarking with Confidence.” In: *New Journal of Physics* 16.10 (Oct. 20, 2014), p. 103032. DOI: [10.1088/1367-2630/16/10/103032](https://doi.org/10.1088/1367-2630/16/10/103032) (cited on page 120).

- [196] Jens Koch et al. “Charge-Insensitive Qubit Design Derived from the Cooper Pair Box.” In: *Physical Review A* 76.4 (Oct. 12, 2007), p. 042319. doi: [10.1103/PhysRevA.76.042319](https://doi.org/10.1103/PhysRevA.76.042319) (cited on page 121).
- [197] J. R. Petta et al. “Coherent Manipulation of Coupled Electron Spins in Semiconductor Quantum Dots.” In: *Science* 309.5744 (Sept. 30, 2005), pp. 2180–2184. doi: [10.1126/science.1116955](https://doi.org/10.1126/science.1116955) (cited on page 121).
- [198] Christopher J. Wood and Jay M. Gambetta. “Quantification and Characterization of Leakage Errors.” In: *Physical Review A* 97.3 (Mar. 8, 2018), p. 032306. doi: [10.1103/PhysRevA.97.032306](https://doi.org/10.1103/PhysRevA.97.032306) (cited on pages 121, 163).
- [199] Gen Kimura. “The Bloch Vector for N-level Systems.” In: *Physics Letters A* 314.5–6 (Aug. 21, 2003), pp. 339–349. doi: [10.1016/S0375-9601\(03\)00941-1](https://doi.org/10.1016/S0375-9601(03)00941-1) (cited on page 123).
- [200] Reinhold A Bertlmann and Philipp Krammer. “Bloch Vectors for Qudits.” In: *Journal of Physics A: Mathematical and Theoretical* 41.23 (June 13, 2008), p. 235303. doi: [10.1088/1751-8113/41/23/235303](https://doi.org/10.1088/1751-8113/41/23/235303) (cited on page 123).
- [201] F. T. Hioe and J. H. Eberly. “N-Level Coherence Vector and Higher Conservation Laws in Quantum Optics and Quantum Mechanics.” In: *Physical Review Letters* 47.12 (Sept. 21, 1981), pp. 838–841. doi: [10.1103/PhysRevLett.47.838](https://doi.org/10.1103/PhysRevLett.47.838) (cited on page 123).
- [202] Don Coppersmith and Shmuel Winograd. “Matrix Multiplication via Arithmetic Progressions.” In: *Journal of Symbolic Computation* 9.3 (Mar. 1990), pp. 251–280. doi: [10.1016/S0747-7171\(08\)80013-2](https://doi.org/10.1016/S0747-7171(08)80013-2) (cited on page 125).
- [203] N. G. Van Kampen. “A Cumulant Expansion for Stochastic Linear Differential Equations. I.” In: *Physica* 74.2 (June 1, 1974), pp. 215–238. doi: [10.1016/0031-8914\(74\)90121-9](https://doi.org/10.1016/0031-8914(74)90121-9) (cited on page 128).
- [204] N. G. Van Kampen. “A Cumulant Expansion for Stochastic Linear Differential Equations. II.” In: *Physica* 74.2 (June 1, 1974), pp. 239–247. doi: [10.1016/0031-8914\(74\)90122-0](https://doi.org/10.1016/0031-8914(74)90122-0) (cited on page 128).
- [205] Lotte Geck. “Scalable Control Electronics for a Spin Based Quantum Computer.” PhD thesis. Jülich: Forschungszentrum Jülich GmbH, 2021 (cited on page 129).
- [206] Wikipedia contributors. *Rayleigh Distribution*. Wikipedia, The Free Encyclopedia. July 20, 2024. URL: https://en.wikipedia.org/w/index.php?title=Rayleigh_distribution&oldid=1235639507 (visited on 01/10/2025) (cited on page 130).
- [207] Awad H. Al-Mohy, Nicholas J. Higham, and Samuel D. Relton. “Computing the Fréchet Derivative of the Matrix Logarithm and Estimating the Condition Number.” In: *SIAM Journal on Scientific Computing* 35.4 (Jan. 2013), pp. C394–C410. doi: [10.1137/120885991](https://doi.org/10.1137/120885991) (cited on page 130).
- [208] Charles R. Harris et al. “Array Programming with NumPy.” In: *Nature* 585.7825 (Sept. 17, 2020), pp. 357–362. doi: [10.1038/s41586-020-2649-2](https://doi.org/10.1038/s41586-020-2649-2) (cited on page 134).
- [209] Pauli Virtanen et al. “SciPy 1.0: Fundamental Algorithms for Scientific Computing in Python.” In: *Nature Methods* 17.3 (Mar. 2, 2020), pp. 261–272. doi: [10.1038/s41592-019-0686-2](https://doi.org/10.1038/s41592-019-0686-2) (cited on page 134).
- [210] John D. Hunter. “Matplotlib: A 2D Graphics Environment.” In: *Computing in Science & Engineering* 9.3 (2007), pp. 90–95. doi: [10.1109/MCSE.2007.55](https://doi.org/10.1109/MCSE.2007.55) (cited on page 134).
- [211] Daniel G. A. Smith and Johnnie Gray. “Opt_einsum - A Python Package for Optimizing Contraction Order for Einsum-like Expressions.” In: *Journal of Open Source Software* 3.26 (June 29, 2018), p. 753. doi: [10.21105/joss.00753](https://doi.org/10.21105/joss.00753) (cited on page 134).
- [212] Pydata, *Sparse* 2019. URL: <https://github.com/pydata/sparse/> (cited on page 134).
- [213] E. L. Hahn. “Spin Echoes.” In: *Physical Review* 80.4 (Nov. 15, 1950), pp. 580–594. doi: [10.1103/PhysRev.80.580](https://doi.org/10.1103/PhysRev.80.580) (cited on page 135).
- [214] Julian David Teske. “A Software Framework for the Realistic Simulation and Optimal Control of Solid-State Qubits.” PhD thesis. Aachen: RWTH Aachen University, Oct. 25, 2022 (cited on page 136).
- [215] Isabel Nha Minh Le et al. “Analytic Filter-Function Derivatives for Quantum Optimal Control.” In: *Physical Review Applied* 17.2 (Feb. 2, 2022), p. 024006. doi: [10.1103/PhysRevApplied.17.024006](https://doi.org/10.1103/PhysRevApplied.17.024006) (cited on pages 136, 150).
- [216] Simon Humpohl. PhD thesis. Aachen: RWTH Aachen University, 2025 (cited on page 136).
- [217] S. Humpohl et al., *Qutech/Qupulse* version 0.6, July 2021. Zenodo. doi: [10.5281/zenodo.2650139](https://doi.org/10.5281/zenodo.2650139), (cited on page 136).

- [218] Thomas Kluyver et al. “Jupyter Notebooks—a Publishing Format for Reproducible Computational Workflows.” In: *Positioning and Power in Academic Publishing: Players, Agents and Agendas*. 2016, pp. 87–90. DOI: [10.3233/978-1-61499-649-1-87](#) (cited on page 138).
- [219] Pascal Cerfontaine et al. “High-Fidelity Gate Set for Exchange-Coupled Singlet-Triplet Qubits.” In: *Physical Review B* 101.15 (Apr. 28, 2020), p. 155311. DOI: [10.1103/PhysRevB.101.155311](#). arXiv: [1901.00851](#) (cited on pages 138–140, 144).
- [220] A. Wallraff et al. “Strong Coupling of a Single Photon to a Superconducting Qubit Using Circuit Quantum Electrodynamics.” In: *Nature* 431.7005 (Sept. 2004), pp. 162–167. DOI: [10.1038/nature02851](#) (cited on page 140).
- [221] E.T. Jaynes and F.W. Cummings. “Comparison of Quantum and Semiclassical Radiation Theories with Application to the Beam Maser.” In: *Proceedings of the IEEE* 51.1 (1963), pp. 89–109. DOI: [10.1109/PROC.1963.1664](#) (cited on page 141).
- [222] Christopher C. Gerry and Peter Knight. *Introductory Quantum Optics*. 3. print. Cambridge: Cambridge Univ. Press, 2008. 317 pp. (cited on page 141).
- [223] Fei Yan et al. “Rotating-Frame Relaxation as a Noise Spectrum Analyser of a Superconducting Qubit Undergoing Driven Evolution.” In: *Nature Communications* 4.1 (Dec. 15, 2013), p. 2337. DOI: [10.1038/ncomms3337](#). PMID: [23945930](#) (cited on pages 141, 142).
- [224] D. M. Zajac et al. “Resonantly Driven CNOT Gate for Electron Spins.” In: *Science* 359.6374 (Jan. 26, 2018), pp. 439–442. DOI: [10.1126/science.aao5965](#). PMID: [29217586](#) (cited on page 141).
- [225] Jarryd J. Pla et al. “A Single-Atom Electron Spin Qubit in Silicon.” In: *Nature* 489.7417 (Sept. 19, 2012), pp. 541–545. DOI: [10.1038/nature11449](#) (cited on page 141).
- [226] Chunqing Deng et al. “Observation of Floquet States in a Strongly Driven Artificial Atom.” In: *Physical Review Letters* 115.13 (Sept. 24, 2015), p. 133601. DOI: [10.1103/PhysRevLett.115.133601](#) (cited on page 141).
- [227] E. Knill et al. “Randomized Benchmarking of Quantum Gates.” In: *Physical Review A* 77.1 (Jan. 8, 2008), p. 012307. DOI: [10.1103/PhysRevA.77.012307](#) (cited on page 143).
- [228] Easwar Magesan et al. “Efficient Measurement of Quantum Gate Error by Interleaved Randomized Benchmarking.” In: *Physical Review Letters* 109.8 (Aug. 24, 2012), p. 080505. DOI: [10.1103/PhysRevLett.109.080505](#) (cited on page 143).
- [229] Māris Ozols. “Clifford Group.” July 31, 2008 (cited on page 143).
- [230] Jeffrey M. Epstein et al. “Investigating the Limits of Randomized Benchmarking Protocols.” In: *Physical Review A* 89.6 (June 18, 2014), p. 062321. DOI: [10.1103/PhysRevA.89.062321](#) (cited on pages 143, 144).
- [231] M. A. Fogarty et al. “Nonexponential Fidelity Decay in Randomized Benchmarking with Low-Frequency Noise.” In: *Physical Review A* 92.2 (Aug. 11, 2015), p. 022326. DOI: [10.1103/PhysRevA.92.022326](#). arXiv: [1502.05119](#) (cited on page 143).
- [232] Guanru Feng et al. “Estimating the Coherence of Noise in Quantum Control of a Solid-State Qubit.” In: *Physical Review Letters* 117.26 (Dec. 20, 2016), p. 260501. DOI: [10.1103/PhysRevLett.117.260501](#) (cited on page 143).
- [233] S. Mavadia et al. “Experimental Quantum Verification in the Presence of Temporally Correlated Noise.” In: *npj Quantum Information* 4.1 (Dec. 2018), p. 7. DOI: [10.1038/s41534-017-0052-0](#) (cited on page 143).
- [234] C. L. Edmunds et al. “Dynamically Corrected Gates Suppressing Spatiotemporal Error Correlations as Measured by Randomized Benchmarking.” In: *Physical Review Research* 2.1 (Feb. 13, 2020), p. 013156. DOI: [10.1103/PhysRevResearch.2.013156](#) (cited on page 143).
- [235] Pascal Cerfontaine et al. “Closed-Loop Control of a GaAs-based Singlet-Triplet Spin Qubit with 99.5% Gate Fidelity and Low Leakage.” In: *Nature Communications* 11.1 (Dec. 2020), p. 4144. DOI: [10.1038/s41467-020-17865-3](#) (cited on pages 144, 163, 164).
- [236] Navin Khaneja et al. “Optimal Control of Coupled Spin Dynamics: Design of NMR Pulse Sequences by Gradient Ascent Algorithms.” In: *Journal of Magnetic Resonance* 172.2 (Feb. 2005), pp. 296–305. DOI: [10.1016/j.jmr.2004.11.004](#) (cited on pages 145, 146).

- [237] T. Schulte-Herbrüggen et al. “Optimal Control-Based Efficient Synthesis of Building Blocks of Quantum Algorithms: A Perspective from Network Complexity towards Time Complexity.” In: *Physical Review A* 72.4 (Oct. 27, 2005), p. 042331. DOI: [10.1103/PhysRevA.72.042331](https://doi.org/10.1103/PhysRevA.72.042331) (cited on pages 145, 146).
- [238] Tommaso Caneva, Tommaso Calarco, and Simone Montangero. “Chopped Random-Basis Quantum Optimization.” In: *Physical Review A* 84.2 (Aug. 22, 2011), p. 022326. DOI: [10.1103/PhysRevA.84.022326](https://doi.org/10.1103/PhysRevA.84.022326) (cited on page 145).
- [239] D. Coppersmith. *An Approximate Fourier Transform Useful in Quantum Factoring*. Technical report, IBM Research Division, 1994. arXiv: [quant-ph/0201067](https://arxiv.org/abs/quant-ph/0201067) (cited on page 146).
- [240] Peter W. Shor. “Polynomial-Time Algorithms for Prime Factorization and Discrete Logarithms on a Quantum Computer.” In: *SIAM Journal on Computing* 26.5 (Oct. 1997), pp. 1484–1509. DOI: [10.1137/S0097539795293172](https://doi.org/10.1137/S0097539795293172) (cited on page 146).
- [241] Tatsuro Yuge, Susumu Sasaki, and Yoshiro Hirayama. “Measurement of the Noise Spectrum Using a Multiple-Pulse Sequence.” In: *Physical Review Letters* 107.17 (Oct. 18, 2011), p. 170504. DOI: [10.1103/PhysRevLett.107.170504](https://doi.org/10.1103/PhysRevLett.107.170504) (cited on page 149).
- [242] Heinz-Peter Breuer and Francesco Petruccione. *The Theory of Open Quantum Systems*. Oxford: Oxford University Press, 2007. 656 pp. (cited on page 149).
- [243] Simon J Devitt, William J Munro, and Kae Nemoto. “Quantum Error Correction for Beginners.” In: *Reports on Progress in Physics* 76.7 (July 1, 2013), p. 076001. DOI: [10.1088/0034-4885/76/7/076001](https://doi.org/10.1088/0034-4885/76/7/076001) (cited on page 149).
- [244] Hui Khoon Ng, Daniel A. Lidar, and John Preskill. “Combining Dynamical Decoupling with Fault-Tolerant Quantum Computation.” In: *Physical Review A* 84.1 (July 5, 2011), p. 012305. DOI: [10.1103/PhysRevA.84.012305](https://doi.org/10.1103/PhysRevA.84.012305) (cited on page 149).
- [245] A. G. Kofman and G. Kurizki. “Acceleration of Quantum Decay Processes by Frequent Observations.” In: *Nature* 405.6786 (June 2000), pp. 546–550. DOI: [10.1038/35014537](https://doi.org/10.1038/35014537) (cited on page 149).
- [246] Adam Zaman Chaudhry. “A General Framework for the Quantum Zeno and Anti-Zeno Effects.” In: *Scientific Reports* 6.1 (Sept. 13, 2016), p. 29497. DOI: [10.1038/srep29497](https://doi.org/10.1038/srep29497) (cited on page 149).

Special Terms

Numbers

2DEG two-dimensional electron gas. v, 56, 98–100

A

APD avalanche photodiode. 25, 98

API Application Programming Interface. 25, 105, 125, 134

AR anti-reflection. 56

B

BEC Bose-Einstein condensate. 24

BLG bilayer graphene. 58

BS beam splitter. 25, 56, 57

C

CCD charge-coupled device. 25, 56, 98

CRAB chopped random-basis. 145

CSD cross power spectral density. 21, 22

cw continuous-wave. 25, 98

D

DAQ data acquisition. 2, 3, 20

DCG dynamically corrected gate. 104, 108, 116, 140, 142, 164

DD dynamical decoupling. 104, 108, 116, 147

DR dilution refrigerator. 24, 25, 56

E

EPR Einstein-Podolsky-Rosen. 60, 61

F

FES Fermi-edge singularity. 98

FF filter function. 104, 112, 116, 124–126, 128–132, 174, 175

G

GDQD gate-defined quantum dot. 57, 62, 63

GGM generalized Gell-Mann. 123, 124, 135, 164

GKSL Gorini-Kossakowski-Sudarshan-Lindblad. vi, 103, 148, 173–175

GRAPE gradient ascent pulse engineering. v, 145, 146, 160, 164, 165

GST gate set tomography. 107

H

HBT Hanbury Brown-Twiss. 25

I

i.i.d. independent and identically distributed. 109

IQ in-phase/quadrature. 146, 165

IRB interleaved randomized benchmarking. 143

L

LD Loss-DiVincenzo. 62

M

MC Monte Carlo. 105, 121, 124–126, 128–132, 148, 173–175

ME Magnus expansion. 104, 108, 110, 111, 117, 165–167

MFD mode field diameter. 26

MMF multi-mode fiber. 25
MOS metal-oxide-semiconductor. 141
MXC mixing chamber. 25

N

NA numerical aperture. 25
ND neutral-density. 25

O

OAQD optically active quantum dot. 62

P

PL photoluminescence. v, 63, 98–101
PLE photoluminescence excitation. v, 63, 99, 100
POVM positive operator-valued measure. 120
PSD power spectral density. iii, 3, 20–22, 57, 114, 128, 131, 173, 174
PTM Pauli transfer matrix. 107, 131, 173
PTR pulse tube refrigerator. 26, 57, 58

Q

QCSE quantum-confined Stark effect. 62, 63, 98, 99
QD quantum dot. 56, 61–63
QEC quantum error correction. 61, 149
QFT quantum Fourier transform. v, vi, 105, 123, 146–148, 160, 164, 165, 173–175
QPT quantum process tomography. 107
QW quantum well. 62, 98–100

R

RB randomized benchmarking. 105, 107, 120, 143, 145
RF resonance-fluorescence. 100
RMS root mean square. 57, 128
RWA rotating-wave approximation. 141

S

SAQD self-assembled quantum dot. 26, 62
SE spin echo. 132, 135, 136
SMF single-mode fiber. 25, 26, 56, 57
SNR signal-to-noise ratio. 57
SOI spin-orbit interaction. 58
SPAM state preparation and measurement. 143, 144
SPCM single-photon counting module. 25
SRB standard randomized benchmarking. 143–145
ST singlet-triplet. 62

T

TEM transverse electromagnetic. 57
TMD transition-metal dichalcogenide. 58
TMM transfer-matrix method. v, 100

V

VC vibration criterion. 57

Declaration of Authorship

I, Tobias Hangleiter, declare that this thesis and the work presented in it are my own and has been generated by me as the result of my own original research.

I do solemnly swear that:

1. This work was done wholly or mainly while in candidature for the doctoral degree at this faculty and university;
2. Where any part of this thesis has previously been submitted for a degree or any other qualification at this university or any other institution, this has been clearly stated;
3. Where I have consulted the published work of others or myself, this is always clearly attributed;
4. Where I have quoted from the work of others or myself, the source is always given. This thesis is entirely my own work, with the exception of such quotations;
5. I have acknowledged all major sources of assistance;
6. Where the thesis is based on work done by myself jointly with others, I have made clear exactly what was done by others and what I have contributed myself;
7. Parts of this work have been published before as:

Aachen, September 5, 2025.